UNIVERSITY OF CALIFORNIA SAN DIEGO

Surrogacy of Beryllium Welds and Heat Transfer in Metals

A dissertation submitted in partial satisfaction of the
requirements for the degree Doctor of Philosophy

in

Engineering Sciences
(Mechanical Engineering)

by

Everett M. Criss

Committee in charge:

Professor Marc. A. Meyers, Chair
Professor Gilbert A. Hegemier
Professor Bimal K. Kad
Professor Vlado A. Lubarda
Professor Joanna M. McKittrick
Professor Frank E. Talke

2015

This Dissertation of Everett M. Criss is approved, and it is acceptable in quality and form for publication on microfilm and electronically

---

Chair

University of California, San Diego

2015

DEDICATION

To my beautiful Kaitlin,
whose patience and hard work
enabled the completion of this thesis.

TABLE OF CONTENTS

Signature Page..... iii

Dedication..... iv

Table of Contents..... v

List of Figures..... ix

List of Tables..... xi

Acknowledgments..... xii

Vita..... xiv

Abstract of the Dissertation..... xv

Chapter 1. Introduction and Goals..... 1

1.1 Introduction to Surrogacy..... 1

1.2 Rationale for Beryllium Surrogacy..... 5

1.3 Introduction to the Surrogate Cobalt Silver-Copper System..... 6

1.4 Determination of the Surrogate System..... 8

1.4.1 Base Surrogacy..... 10

1.4.2 Filler Surrogacy..... 11

1.5 Goals for the Cobalt Silver-Copper System..... 13

1.6 Organization of Welding Experiments..... 13

Chapter 2. Welding Background..... 16

2.1 Welding Fundamentals..... 16

2.2 Metallurgy of Fusion Welds..... 19

2.2.1 Regions Inside Fusion Welds..... 20

2.2.2 Metallurgical Effects in the True Heat Affected Zone..... 21

2.2.3 Metallurgical Effects in the Partially Melted Zone..... 22

2.2.4 Metallurgical Effects in the Fusion Zone..... 23

2.3 Theoretical Analysis of Heat Flow..... 26

2.3.1 Rosenthal's Equations..... 27

2.3.2 Analysis of Peak Temperatures..... 31

2.3.3 Numerical Analysis of Rosenthal's Three Dimensional Equation..... 33

2.3.4 Further Analysis of the Rosenthal Equations..... 34

2.4 Numerical Analysis of Welding..... 34

Chapter 3. Materials, Experiments and Techniques..... 37

3.1 Welding Materials..... 37

3.2 XRD Characterization..... 37

3.3 Welding Equipment, Materials and Parameters..... 38

3.4 Fracture in Tension and Four-Point Bending..... 41

3.4.1 Root Bending Tests of Different Weld Stages..... 42

3.4.2 Tension Test..... 44

3.4.3 Root and Face Bending Tests of Completed Welds..... 46

3.5 Optical Microscopy & Etching..... 46

3.6 Optical Microscopy with Polishing Slurry..... 48

3.7 Scanning Electron Microscopy and Energy Dispersive X-ray Spectroscopy..... 48

3.8 Spatially Resolved Acoustic Spectroscopy (SRAS)..... 49

3.9 Electron Microprobe and Wavelength Dispersive Analysis (WDS)..... 50

3.10 Finite Element Analysis (FEA) of Fracture..... 50

3.10.1 FEA Material Parameters..... 51

3.10.2 FEA of Sections Fractured at Various Welding Stages..... 53

3.10.3 FEA of Sections Fractured from Completed Welds..... 55

3.10.3.1 Tension FEA..... 56

3.10.3.2 Face and Root 4-Point Bending FEA..... 57

3.10.3.3 Root 4-Point Bending (residual stress study) FEA..... 58

3.11 Crack Compliance Method..... 58

3.11.1 Strain Measurements..... 59

3.11.2 Data Reduction..... 60

3.12 Welding Voltage and Current Measurement..... 61

Chapter 4. Welding Results and Discussion..... 62

4.1 Welding Methodology and Parameters..... 62

4.1.1 Welding Parameter Determination..... 62

4.1.2 Final Welding Parameters..... 64

4.2 Welding Results at Differing Welds Stages..... 68

4.2.1 Microscopy at Differing Weld Stages..... 69

4.2.2 Fracture Testing and FEA at Differing Weld Stages..... 72

4.3 Welding Results For Completed Welds..... 81

4.3.1 Spatially Resolved Acoustic Spectroscopy, Optical Microscopy, and Electron Microprobe on Unfractured, Completed Weldments..... 81

4.3.2 SEM, FEA and Fracture of Tensile Specimens from Completed Weldments.... 86

4.3.3 Fracture of an Unground, Completed Weld in Root Bending..... 91

4.3.4 Fracture, SEM and FEA of Completed Welds in Face and Root Bending..... 92

4.3.5 Residual Stress, Heat Treatment, and Root Bending.....98

Chapter 5. Surrogacy Discussion.....101

5.1 Advantages and Drawbacks of Surrogacy..... 101

5.2 Implications for the Be-AlSi System..... 103

5.2.1 Effects of Geometry..... 103

5.2.2 Effects of Cracking and Porosity..... 104

5.2.3 Effects of Residual Stress..... 106

5.3 Suggested Experiments for the Be-AlSi Welding System.....108

5.4 Improving the Be-AlSi Welding System.....109

Chapter 6. Conclusions.....111

6.1 Conclusions Regarding the Co-AgCu Welding System.....111

6.2 Conclusions Regarding Welding Surrogacy..... 114

6.3 Suggestions for Further Research.....116

References.....117

Appendix I. Welding Parameter Studies.....125

LIST OF FIGURES

Figure 1: Five basic weld joint types..... 19

Figure 2: Co-AgCu weld schematics..... 39

Figure 3: Traverse root and face bending orientations..... 41

Figure 4: Weld schematics..... 42

Figure 5: 5-pass weld showing section locations and welding directions..... 43

Figure 6: Fracture Setup, and its corresponding FEA..... 44

Figure 7: Tension test pieces, tension test, and FEA model..... 45

Figure 8: Sectioning for four-point bending, heat treatment, and residual stress measurement..... 45

Figure 9: Welds sectioned at increasing number of passes..... 47

Figure 10: Calculated Stress vs. Strain..... 54

Figure 11: FEA filler shape..... 55

Figure 12: Comparison of weld geometries..... 66

Figure 13: Welding voltages and currents..... 67

Figure 14: Weld regions..... 69

Figure 15: Optical micrographs..... 71

Figure 16: SEM backscatter and EDX images of the weld-filler interface..... 72

Figure 17: von Mises stresses at failure..... 73

Figure 18: Applied load vs. displacement curves for fracture specimens and FEA models..... 74

Figure 19: Section stiffness..... 75

Figure 20: Applied loads and deflections at failure..... 77

Figure 21: Failure loads and deflections by sample position..... 78

Figure 22: Failure loads vs. displacements arranged by weld..... 78

Figure 23: Average failure loads and deflections..... 80

Figure 24: Weld macrostructure, microstructure, and WDS sample locations.....82

Figure 25: Weld composition vs. distance from AgCu filler.....83

Figure 26: SRAS velocity vector map and optical weld images.....84

Figure 27: Weld macrostructure.....85

Figure 28: Tension test and FEA.....87

Figure 29: Predicted von Mises Stress at tensile failure.....88

Figure 30: SEM fractography of tensile failure surface.....89

Figure 31: Failure strength and displacement of unground welds.....91

Figure 32: Failure strength of ground welds in face and root bending.....93

Figure 33: FEA of root and face bending.....94

Figure 34: FEA predicted and observed failures in face and root bending.....95

Figure 35: SEM of failures in root and face bending.....96

Figure 36: Measured residual stress.....99

Figure 37: Optical micrograph of a Be-AlSi weld.....104

LIST OF TABLES

Table 1: Core criteria for the surrogate welding system..... 9

Table 2: Relevant properties of potential base elements..... 11

Table 3: Characteristics of Be-AlSi and Co-AgCu alloy systems..... 11

Table 4: Relevant properties of fillers, and their constitutive elements..... 12

Table 5: FEA material parameters..... 53

Table 6: FEA geometry..... 56

Table 7: Finite element parameters..... 57

Table 8: Welding parameter comparison..... 66

Table 9: Material Composition by Region..... 90

Table 10: Residual Stress..... 99

ACKNOWLEDGEMENTS

I would like to acknowledge my adviser, Professor Marc Meyers, for all of his support and guidance. I would like to thank Dr. Bimal Kad, for suggesting this research topic, and supporting early research. I also thank my thesis committee, composed of my adviser, Professor Marc Meyers, as well as Professor Gilbert Hegemier, Dr. Bimal Kad, Professor Vlado Lubarda, Professor Joanna McKittrick and Professor Frank Talke.

I would like to extend special thanks to Professor Joanna McKittrick and Professor Frank Talke, for the extraordinary effort and time both of them spent revising this document. Thank you both for your time, and the essential direction you have provided. These two professors went above and beyond the normal expected role of committee member, by recommending significant modifications and improvements to my thesis document.

I must extend thanks to all those who reviewed and edited the manuscript, either in full or in part. This includes Tane Remington, Shiteng Zhao, Vincent Sherman, Professor Robert Criss, Kaitlin Gange, Cindie Power and Bill Power.

I thank Bob Musson, Don Johnson, Steven Rodriguez and Dr. Bimal Kad for assisting in my experiments, as well as Bin Wang for producing most of the excellent SEM images.

I would like to acknowledge Professor Anne Hofmeister, Professor Marc Meyers and Dr. Richard Smith for coauthoring three of my papers.

Portions of Chapters 1, 2, 3 and 4 may be found in E.M. Criss, M.A. Meyers. *Braze welding of cobalt with a silver-copper filler*. Journal of Materials Research and Technology, **4**(1): 44-59 (2015), see [1].

Different portions of these same chapters may be found in E.M. Criss, R.J. Smith, M.A. Meyers. *Failure mechanisms in cobalt welded with a silver-copper filler*. Materials Science and Engineering, A. (2015): *in press,* see [2].

Lastly, I extend special thanks to Craig Hobson. Not only was he responsible for producing the welds, he also contributed substantially in the development of the welding system.

VITA

2006	Bachelor of Science, Case Western Reserve University
2006-2010	Los Alamos Fellow, University of California, San Diego
2008	Master of Science, University of California, San Diego
2015	Doctor of Philosophy, University of California, San Diego

PUBLICATIONS

E.M. Criss, R.J. Smith, M.A. Meyers. *Failure mechanisms in cobalt welded with a silver-copper filler*. Materials Science and Engineering, A. (2015) *In press*

E.M. Criss, M.A. Meyers. *Braze welding of cobalt with a silver-copper filler*. Journal of Materials Research and Technology, **4**(1): 44-59 (2015)

R.E. Criss, E.M. Criss. *Prediction of well levels in the alluvial aquifer along the lower Missouri River*. Ground Water, **50**(4): 571-577 (2011)

E.M. Criss, R.E. Criss, G.R. Osburn. *Effects of stress on cave passage shape in karst terranes*. Rock Mechanics and Rock Engineering, **41**(3): 499-505 (2008)

ABSTRACT OF THE DISSERTATION

Surrogacy of Beryllium Welds and Heat Transfer in Metals

by

Everett M. Criss

Doctor of Philosophy in Engineering Sciences (Mechanical Engineering)

University of California, San Diego, 2015

Professor Marc A. Meyers, Chair

A new method of joining Co by braze-welding it with an AgCu filler was developed in order to better understand the residual stresses in Be-AlSi weldments. The constituents of this new welding system were selected to replicate the physical properties, crystal structures, and chemical behaviors of the Be-AlSi welds; "welding surrogacy" is used to describe this process. Final welds are five pass manual tungsten inert gas (TIG), with He top-gas and Ar back-gas. Final welds exhibit full penetration melting of the cobalt base, while microscopy indicates that cracking is minimal and not through

thickness. Welds are composed of five seperate regions consisting of the unaffected Co base, the heat affected zone, the melted Co base, the AgCu filler, and the CoCu peritectic.

Failure tests of the surrogate welds show that residual stresses have little or no effect on strength, whereas weld quality and geometry are extremely important. Crack compliance measurements show that the largest residual stresses are located along the Co-AgCu interface, as is expected. Residual stresses in the weld root are too small to observably effect failure, whereas stresses in the CoCu region cannot influence failure due to their location and direction. The strength of Co-AgCu welds depends strongly on geometry, penetration, and defects, but little on residual stresses, and this conclusion is tentatively extended to Be-AlSi welds.

Chapter 1. Introduction and Goals

This dissertation analyzes the process of welding surrogacy, and includes supporting metallurgical and mechanical research. Chapter 1 describes the process of surrogacy, the rationale behind welding surrogacy, and the process of surrogate selection. Chapter 2 provides background information on welding processes, metallurgy and heat transfer. Chapter 3 describes the experimental techniques used in the joining of the surrogate materials, and in their characterization and failure analysis. Chapter 4 provides the results of the welding-based experiments, discusses the quality of the surrogate, and discusses the effects of weld geometry, quality, and residual stress upon failure. Chapter 5 discusses the results of surrogacy. Chapter 6concludes these welding investigations.

1.1 Introduction to Surrogacy

Experimental surrogacy is a technique involving substitution of similar parts, materials, or reactions during experimentation. The original system is referred to here as the parent system, while the substitute system is referred to as the surrogate system. Surrogates are selected based on the phenomena being studied; careful selection allows indirect experimentation in situations where direct experimentation is difficult or impossible. Similar concepts exist in mathematics which involve surrogacy of data (e.g., [1]) or functions (e.g., [2]). Such concepts have also been used in modeling. Surrogacy based methods, such as surrogate assisted evolutionary computation [3] or surrogate-based analysis and optimization [4] emulate the behavior of complex systems by substituting high fidelity models with high efficiency surrogate models [3,4]. These

methods have been successfully applied to problems in aeronautics, such rotor blade and airfoil design [4], but have numerous other potential applications for complex, practical problems [3]. Surrogacy, as a concept, is fundamental to the sciences. Both mathematical and numerical models function as surrogates of physical reality, thereby enabling investigation of phenomena too complex to otherwise analyze [5].

Several variants of experimental surrogacy exist. Cramer and Britt [6,7] pioneered the development of reaction surrogacy, in which the product of the parent and surrogate reactions is the same. This technique has been used in the study of nuclear reactions, since it is possible to produce the desired compound nucleus a variety of ways (e.g., [8]).

Industrially, surrogacy involving the substitution of similar parts is used for training purposes, or as pre-production placeholders (e.g., [9]). As such, prototyping can be considered a surrogate process, since it involves substitution of a final product with a similar, pre-production version. Somewhat similarly, surfaces may be surrogated. This technique has proven useful in the study of surface deposition [10].

Surrogacy has also been used in the study of biology, as it allows control of sample properties and reduction of health hazards. Moghtaderi et al. [11] considered a ceramic substitute for wood, which allowed control of material porosity during re-ignition experiments. Lewis et al. [12] discussed the use of latex as a surrogate for blood during the calibration of haematology analyzers. Lytle et al. [13] evaluated several bacteriophages as surrogates for human viruses, and suggests a surrogate for the human immunodeficiency virus, enabling safe and inexpensive verification of barrier materials. Lyons et al. [14] suggested that reconstituted powdered potatoes be used a an intestinal surrogate to asses post-laparoscopic wound closure methods.

Materials surrogacy involves the substitution of similar materials. Occasionally, surrogacy is used when the exact material properties and composition are unknown, or when quantities of the desired material is unavailable. Development of such surrogates usually revolves around accurate emulation of the parent material's chemistry. Wykes et al. [15] used hydrocarbon flakes as well as tungsten and tungsten carbide particles to emulate dust produced in tokamak reactors. Biemeller [16] conducted a metallurgical study evaluating the plate and welds used in a radiation vessel. Weld chemistry was estimated based on historical records, and surrogate welds were produced using duplicate methods [16]. Reynolds et al. [17] used a surrogate to evaluate the health effects of coal dust, since the quantity of dust he required was unavailable.

Materials surrogacy is also performed to avoid direct experimentation involving dangerous or otherwise unobtainable materials. This subtype of surrogacy differs from the methods described above, since accurate chemical reproduction is not desirable. Instead, surrogates are selected to emulate the particular phenomena being studied. Commonly, this method is used to study radioactive materials. In their combustion study, Yang et al. [18] used neodymium, samarium, cerium, gadolinium, cesium and cobalt to surrogate uranium, plutonium, americium, curium, radioactive cesium and radioactive cobalt, respectively. Delegard et al. [19] evaluated the properties of uranium and uranium dioxide contaminated sludge. They conclude that a tungsten alloy, Densalloy SD170, can be used as a uranium surrogate, and that a combination of cerium dioxide and steel grit be used as uranium dioxide surrogates [19].

More complex radioactive materials may also be surrogated. Kercher and Hunn [20] compiled several characterization studies, and conclude that coated yttria stabilized zirconia is a reasonable microstructural surrogate for certain types of reactor fuel.

Materials surrogacy is also used in the study of toxic materials, ranging from flammable organic waste [21], to beryllium dust [15]. The toxic nature of beryllium makes it a viable candidate for surrogacy [22,23]. Direct experimentation during welding is especially dangerous due to the potential of beryllium aerosolization. Furthermore, the resources required to safely weld beryllium are specialized and expensive (see Section 2.1). These reasons prompted development of a surrogate welding system to emulate beryllium welding.

However, welding surrogacy is significantly more complicated than other material surrogacy methods, since welding commonly involves interactions between multiple materials at highly varying temperatures. As such, material properties of all weld constituents must be considered, as well as the potential interactions between them. This dissertation advances the study of welding surrogacy, through consideration of the beryllium aluminum-silicon (Be-AlSi) system, and development of the cobalt silver-copper surrogate system (Co-AgCu). Through careful material selection and welding process control, this new cobalt based surrogate system has provides into the behavior of the original, beryllium based welds [22,23].

1.2 Rationale for Surrogacy of the Beryllium Aluminum-Silicon System

This research was motivated by a need to indirectly investigate the behavior of beryllium (Be), specifically the behavior of Be rings Pressurized Inert Gas Metal Arc (PIGMA) welded with 88-12 at.% aluminum-silicon (compositions provided are based on atomic percentages unless noted otherwise) [22,23]. Beryllium is a unique and useful material with many desirable mechanical, thermal, and nuclear properties [24,25]. Its superlative physical properties include high strength, high stiffness, low density, high specific heat, high melting point, and hexagonal crystal structure [22-27]. Commercially, it is used in beryllium-copper and beryllium oxide ceramics [27]. Due to drawbacks, such as its low fracture strength, high cost, and toxicity, its use in pure form is limited to specialty applications in the defense, aerospace, and energy industries [28]. The high sensitivity of Be to cracking has made welding, autogenously or otherwise, particularly difficult [28]. A wide variety of welding techniques have been investigated over the decades; however, joint quality is still highly process dependent [29]. Brazing has emerged as the most reliable and preferred process for the joining of beryllium [29]. Braze-welding, a variation of brazing involving some melting of the base metal, is often used [30]. In this process, the beryllium base partially melts [30] and is joined by silver or aluminum-based filler wire [25]. Although braze-welded beryllium structures are less susceptible to cracking, the different thermal expansion coefficients of the base and filler metals often introduces residual stresses into the part [31]. Investigation of weldments, produced by braze-welding a Be ring with 88-12 at.% AlSi filler prompted the present study. Neutron beam diffraction of these welds reveals residual stress distributions, which are inconsistent with coefficient of thermal expansion (CTE) mismatch [31].

However, CTE mismactch was the expected cause of these stress distributions. Differential heating is a possible explanation for these stress distributions. Additional study is needed to fully understand them; however, directly investigating Be-AlSi welds is limited due to the high toxicity of beryllium [32].

To circumnavigate these issues, we advance the concept of 'surrogacy', the idea that an analogous welding system can be developed and used to provide insights into the behavior of another. Development of a surrogate welding system, based on the physical properties and chemistry of the original, permits evaluation and experimentation not otherwise possible [22,23]. This leads to a better understanding of the behavior of welds, as currently manufactured and studied at the Los Alamos National Laboratory. Although this study was primarily intended to investigate the residual stresses in these Be-AlSi welds, the work done here has broader implications for other exotic weldments.

1.3 Introduction to the Surrogate Cobalt Silver-Copper System

A number of different surrogates were evaluated before cobalt welded with a silver-copper filler (Co-AgCu) was selected as the best possible surrogate system [22]. In this application Co-AgCu must mimic, as accurately as possible, the behavior of Be-AlSi, including the interactions between the Be base and the AlSi filler. Cobalt was found to be an ideal surrogate for beryllium-based weldments, due to the mechanical, thermal, and crystallographic similarities of the two elements [22,23].

Cobalt, like beryllium, has a hexagonal close packed (HCP) crystal structure, a relatively high stiffness, and a similar melting point [22,23,26,33,34]. Selection of this material as a base imposed a number of difficulties, predominantly caused by a lack of

welding information due to the infrequent use of cobalt in pure form. Study of Co, especially its behavior during welding, is important for other reasons. Cobalt is used as an alloying element in a variety of steels, carbides, and wear and corrosion resistant alloys [33]. It is also a primary constituent of batteries, magnets, and superalloys [35,36,37]. Worldwide, cobalt is mainly used as a constituent in batteries [35], while in the United States it is primarily used in superalloys [36].

A few alloys utilize cobalt as their base element, and are routinely welded [22,23]. Cobalt-chromium-molybdenum alloys (e.g., Vitallium, Megallium) are used in dentistry and biomedical implants [38]. Vitallium is usually joined via soldering or brazing [38] but may be joined via torch [39] or Tungsten Inert Gas (TIG) [40]. Cobalt-chromium based alloys (Stellite) are generally used as hard-facings, which are applied using a variety of welding, cladding and brazing techniques [41,42]. TIG may be used to apply Stellite using either helium [41] or argon shielding gas [42]. Heat resistant alloys, often consisting of Co-Cr-Ni-W, are also welded or brazed [33]. Welding is accomplished using a variety of techniques, including TIG, commonly with cobalt or nickel-based fillers [33]. Brazing is accomplished in a vacuum or in a hydrogen atmosphere, preferably with nickel, cobalt, or gold-palladium based filler metals [33].

Behavior of the Ag-Cu filler during welding with Co is also of interest because such filler metals best emulate the chemistry of the Be-AlSi system. Both systems are characterized by a lack of miscibility between filler and base metals [22,23]. The eutectic AgCu filler metal is commonly used as a filler for vacuum brazing [43]. Silver-copper alloys are used in jewelry, tableware (e.g., sterling silver, 92.5 wt.% Ag, [46]), and as electrical contact alloys [47].

Despite the diverse usage of the components of our Co-AgCu system, information is lacking on the brazing of cobalt-copper, due to possible liquid metal embrittlement [46], and welding with HCP cobalt base alloys. A majority of cobalt's structural alloys (Stellite, Vitallium, etc.) utilize the high temperature face-centered cubic (FCC) phase [46], and differ structurally from pure cobalt's HCP structure. Cobalt usage in batteries usually involves cobalt oxide, cobalt hydroxide or lithiated cobalt oxide (Li_xCoO_2) [33,47], which all differ from pure cobalt structurally and chemically. Some samarium-cobalt ($SmCo_5$) magnets do possess a hexagonal crystal structure [48] but are not welded. Because development of Co based superalloys is ongoing [49,50], understanding the behavior of the pure metal is important.

1.4 Determination of the Surrogate System

As detailed below, cobalt braze-welded with 60-40 at.% AgCu was selected as an optimal surrogate for beryllium weldments. To mimic the residual stresses, failure mechanisms, and overall weld behavior, the entire weld system must be surrogated. Selection of a reasonable surrogate insures that the techniques used to join these Co-AgCu welds will be applicable to the original system [22,23]. The quality of this surrogate is not entirely dependent on the material properties of either the base or the filler, but also upon their interactions. The Co-AgCu combination was selected to mimic the key traits of the Be-AlSi system, including base and filler properties, as well as their chemical interactions. This approach allowed the determination of a list of core requirements for our surrogate welding system (Table 1).

Approximating the filler properties was necessary in order to form the core criteria for the surrogate filler. This was done using the Voigt-Reuss-Hill average of the filler's constituent polycrystalline elastic modulus (E) (e.g., [55]):

$$E \approx \frac{1}{2}\left(\frac{1}{\sum \frac{f_i}{E_i}} + \sum E_i f_i \right) \tag{1}$$

where E_i is the elastic modulus of an individual component and f_i is the volume fraction of that component.

This equation was modified *mutatis mutandis* for the coefficient of thermal expansion (α), resulting in:

$$\alpha \approx \frac{1}{2}\left(\frac{\sum f_i E_i \alpha_i}{\sum f_i E_i} + \sum f_i \alpha_i \right) \tag{2}$$

where α_i is the thermal expansion coefficient of the component materials.

Table 1: Core criteria for the surrogate welding system

Core Criteria (base)	**Priority**	**Be-AlSi**	**Co-AgCu**
Safe to weld	1	No	Yes
Hexagonal Base[a]	2	Yes ($P6_3/mmc$)	Yes ($P6_3/mmc$)
Obtainable, less than \$200/kg[b]	3	No(\$235.89/kg)	Yes(\$45.97/kg)
895°C<Base MP<1680°C (within 25%)[a]	4	Yes (1287°C)	Yes (1495°C)
Core Criteria (system)			
Safe to weld	1	No	Yes
Immiscible Base/Filler	2	Yes	Yes
1.25<Filler CTE/Base CTE<2.75[c]	3	Yes(1.95)	Yes(1.38)
2<Base E/Filler E[c]	4	Yes(4.24)	Yes(2.22)
30%<Filler M.p./Base M.p.<80%[d]	5	Yes (54%)	Yes (60%)

[a]Data from [26], [b]Data from [51], [c]Calculated from data in [26] using a Voigt-Reuss-Hill average, [d]Data from [52,53]

Although better approximations are possible, the allowable ranges of the core criteria are sufficiently large that the errors in these calculations are not significant. These criteria were used to select possible surrogate base metals, and to select compatible fillers.

1.4.1 Base Surrogacy

The behavior and material properties of beryllium are highly influenced by its HCP structure and anisotropic lattice, which provides it with the lowest $\underline{c/a}$ ratio of any HCP element [28]. The requirement for our surrogate system to have an HCP base imposes strong limitations on potential surrogates, as very few room temperature HCP elements are both obtainable and safe to weld. Of these materials, zinc was excluded due to its low melting point, and zirconium was excluded due to its excessive melting point.

The core criteria (Table 1) suggest that only cobalt and titanium are viable options. Magnesium was also included for reference due to its chemical similarity to beryllium in spite of its comparatively low melting point (650ºC) and combustible nature.

Table 2 compares the properties of Be, Co, Ti and Mg that are most likely to influence residual stresses inside a weld. This comparison shows that cobalt has the mechanical properties most similar to beryllium, although magnesium is the best thermal match. No viable fillers were found for Mg (see below), and magnesium's high ductility and low stiffness make it a difficult beryllium surrogate, whereas the mismatched thermal properties of cobalt can be mitigated by varying welding techniques. Based on material properties alone, cobalt appears the most reasonable surrogate for beryllium.

Table 2: Relevant properties of potential base elements[a]

Relevant Material Properties	Beryllium	Cobalt	Magnesium	Titanium
Young's Modulus, GPa	318	**211**	44.7	120.2
Poisson's Ratio	0.02	0.32	**0.291**	0.361
CTE, 25ºC, µm/m-ºC	11.3	**13.0**	24.8	8.6
Melting Pt., ºC	1287	**1495**	650	1668
HCP-FCC transition	1270	422	N/A	**882**
Conductivity, W/m-K, 25ºC	210	69.04	**155**	11.4
Specific Heat, J/g-ºK, 0-100ºC	1825	421	**1023**	523
Lattice c/a Ratio	1.5681	1.6228	1.6236	**1.5873**
Density, g/cm^3 20ºC	1.85	8.86	**1.74**	4.51
Immiscible Fillers[b]	Al,Ag,Si	Ag,Au,Cu		Si,V

[a]Data is from [26], unless marked otherwise

[b]Fillers shown are immiscible, commercially obtainable as a primary or secondary constituent in filler wire, and between 50% and 125% the base material's melting point [56].

1.4.2 Filler Surrogacy

The Be-AlSi system is characterized by the immiscibility of its primary constituents (Table 3). In order to replicate the behavior of the Be-AlSi system, it is necessary that the surrogate system also be characterized by base-filler immiscibility. No suitable filler metals were found for either Ti or Mg. The melting point of magnesium is too low for any feasible filler, while no potential titanium fillers conform to all of these criteria.

Table 3: Characteristics of Be-AlSi and Co-AgCu alloy systems[a]

	Al-Si	Al-Be	Be-Si	Ag-Cu	Ag-Co	Co-Cu
Type	Filler	Base-Filler 1	Base-Filler 2	Filler	Base-Filler 1	Base-Filler 2
System	Eutectic	Eutectic	Eutectic	Eutectic	Immiscible	Peritectic
Eutectic Point	12.2 at.%. Si	2.4 at.% Be	36 at.% Si	39.9 at.% Cu	N/A	N/A
Eutectic Temp[b]	577 575	644	1085 1090	780 782	N/A	N/A

[a]Data is from [57-68]

[b]Top value is experimental, bottom is a calculated equilibrium value. Both sources are in agreement for Al-Be.

Cobalt is immiscible with a handful of elements, including copper, silver, gold and lead. Gold was discounted due to high cost, and lead lacks a melting point high enough to function effectively as a filler metal. Silver and copper are relatively inexpensive and

easily obtainable as filler wire due to the prevalence of silver soldering. This availability influenced the choice of cobalt as an ideal material for beryllium surrogacy.

Silver was selected as a filler over copper because it has a CTE ratio further from cobalt, potentially producing higher stresses [26]. However, preliminary welding studies indicate that pure silver is not capable of forming strong welds with cobalt. To correct this deficiency, Ag was alloyed with 40 at.% copper [53]. Material properties of this Co-AgCu surrogate alongside the original Be-AlSi system are provided in Table 4. This surrogate system exceeds all of the original requirements (Table 1). Furthermore, the chemistry of the surrogate system resembles the phase stability of the original Be-AlSi system (Table 3).

Table 4: Relevant properties of fillers, and their constituative elements

	Al[a]	**Si**[a]	**Al-12Si**[b]	**Ag**[a]	**Cu**[a]	**Ag-28Cu**[c]
Young's Modulus, GPa	70.6	113		82.7	129.8	
E, Voigt-Reuss-Hill avg			75			95
Poisson's Ratio	.345	.42		.367	.343	
CTE, 25°C	23.1	7.6		18.9	16.5	
CTE, Voigt-Reuss-Hill avg.			22			18
Melting Pt.	660.323	1412	577-582[d]	961.78	1084.62	780
Conductivity, W/m-K, 25°C	247	156		428	398	
Specific Heat J/kgK, 25°C	897	705		235	385	
Specific Heat, average			874			277
Density, g/cm^3	2.7	2.34		10.5	8.96	

[a]Data from [26]
[b]Data from [52]
[c]Data from [53]
[d]Solidus and liquidus temperatures

The chemistries of the base and surrogate systems differ in one important regard: the limited miscibility between liquid cobalt and liquid silver (monotectic response) leads to Co-Ag phase separation. This difference is unavoidable, and results in microstructural differences near the filler-base interface due to the lack of a eutectic point between silver and cobalt.

1.5 Goals for the Cobalt Silver-Copper System

Development of the Co-AgCu surrogate system allows indirect investigation of the Be-AlSi welding system, without risk of beryllium toxicity [22,23]. Careful selection of our base and filler metals mimics, as closely as possible, the physical properties and chemical interactions of the parent system. Special attention was paid to the mechanical, crystallographic, and chemical properties influencing residual stresses (Section 1.4). As such, residual stress distributions in the surrogate welds should emulate residual stresses in the parent system. Furthermore, similarities in melting points, miscibility, crystallography, and mechanical properties between parent and surrogate systems result in microstructural similarities (cf. [54, 23]). Of especial note are the presence of backfilled cracks and immiscible ternary solutions in both systems (cf. [54, 23]).

Due to these structural, chemical, and mechanical similarities, optimization of welding methods for the Co-AgCu surrogate should improve welding techniques for the Be-AlSi parent system. Furthermore, investigations into failure and stresses in the Co-AgCu surrogate should determine the relative importance of such mechanisms in the parent, Be-AlSi system.

1.6 Organization of Welding Experiments

Due to the reasons outlined above (Section 1.3), there is limited information regarding fabrication and welding of pure cobalt. Furthermore, crystallographic differences between pure cobalt and commonly used cobalt alloys prevent direct use of already established welding parameters [22]. As such, all of the welding parameters had to be independently determined, including filler composition and weld type.

Determination of these parameters was accomplished through an extensive, multi-parameter study. Weld quality was evaluated primarily by investigation [22], however higher quality welds were also evaluated by four-point bending, scanning electron microscopy (SEM), and optical microscopy. In order to satisfactorily join the surrogate materials, novel methods of welding by hand were developed. These include alternating welding direction, adopting unusual weld bead placements, and welding on top of a refractory material. Five welds, including one complete weld, were produced utilizing the final, optimized welding parameters; each weld corresponds to differing stages of weld completion. These welds were failed in 4-point bending, and were further investigated by finite element analysis (FEA). Although the welding parameters developed here differ substantially from the original beryllium welds, the techniques developed should be applicable to Be-AlSi welds and braze-welds in general due to the careful selection of our surrogate materials.

Once these welding parameters were established, the Co-AgCu system was used to investigate the effects that residual stress, weld geometry, weld quality, and post welding heat treatment have on weld failure, allowing extrapolation of these results to welded Be-AlSi [23]. The specialized welding techniques discussed in Section 3.3 were used to create 11 new welds, which were analyzed alongside the single complete weld from the welding parameter study.

These welds were tested utilizing tension and 4-point bending. These failures were combined with the crack compliance (slitting) method to determine the effect of residual stresses. The weldments were further characterized by using scanning electron microscopy (SEM) and wavelength dispersive analysis (WDS), by developing a novel

use of optical microscopy, and by applying spatially resolved acoustic spectroscopy (SRAS). SRAS is a laser ultrasonic technique that produces maps of the surface acoustic wave (SAW) velocity [69,70]. The SAW velocity for a particular propagation direction depends strongly on the crystallographic orientation of the material and can be used to map the microstructure of a material. Combining a number of velocity maps with different acoustic wave propagation directions can generate information about the c-axis orientation for hexagonal materials, or the complete grain orientation for some specific crystallographic symmetries [70].

Effects of low temperature heat treatment on weld strength are examined, in order to determine whether residual stress amelioration is possible. Finite element models were constructed to understand the residual stress measurements and fracture results. This combination of measurements, images and quantitative models shows that residual stresses do not substantially impact failure in Co-AgCu weldments, but that weld geometry, material quality, defects, and imperfections govern weld strength and failure [23]. The insight provided here into the behavior of welded cobalt pertains to the development and joining of new cobalt alloys, as well as the behavior of the original Be-AlSi system.

Chapter 2. Welding Background

2.1 Welding Fundamentals

Welding is a process in which materials, usually metals, are joined by heat and pressure [71-73]. Although various methods of joining materials exist, welding is unique because only this process fuses separate surfaces together, uniting them with a continuous series of similar, interatomic bonds [72,74]. Welding is advantageous, since interfaces are minimized and stress concentrators, such as bolts or rivets, are not involved. Often, welded joints have similar strength to the materials being joined [72].

Welding may be divided into two main categories (e.g., [26]). Non-fusion welding methods, such as explosive welding, utilize pressure to form joints without observable melting. Non-fusion welding methods include forge welding, a process dating to antiquity in which materials are joined via hammering [72,73].

Fusion methods, such as the electric-arc based methods discussed here in detail, form joints via melting due to high temperatures. Melting is a key attribute of fusion welding processes which differentiates them from both brazing and soldering, which do not involve melting of all joint constituents (e.g., [26,71]).

Fusion welding may be accomplished utilizing a variety of methods (e.g., [71,75]). Oxyfuel gas welding utilizes a flame, usually generated from the burning of oxy-acetylene, to produce the weld [76]. Similar methods are also used for cutting and for applying hardfacings. Many resistance welding methods, such as spot welding, are fusion processes (e.g., [71]). These processes fuse metals using pressure and electric current passed through two or more metal surfaces [76]. The interface usually

experiences the highest temperatures due to its high electrical resistance [71,72,76]. Energy beam methods weld via high energy electron or laser beams [71,72]. Although the equipment and particles used are dissimilar, both methods are capable of deep penetration with minimal cross-sectional area (e.g., [71,74,76]). Finally, arc based methods achieve fusion using the heat from an electric arc.

The electrode used to generate this arc may have negative (Direct Current Electron Negative, or DCEN), positive (Direct Current Electron Positive, or DCEP), or alternating (AC) polarity (e.g., [71]). DCEN is associated with higher weld temperatures and is the standard polarity used for most arc welds (e.g., [71]). However, AC and DCEP are occasionally beneficial, due to ionic cleaning of the weld surface resulting from positive polarity [71].

Arc welding methods are further categorized based on the type of electrode and the type of shielding (e.g., [75]). (The following process designations correspond to the AWS standards. Multiple methods use a consumable electrode (e.g., [71,76]). Shielded Metal Arc Welding (SMAW, or stick) involves welding utilizing a consumable electrode containing flux [76]. As the electrode is consumed, this flux disintegrates, protecting the weld from oxidation by forming slag and protective gasses. Furthermore, the electrode functions as a filler metal, allowing the welder to add material to the joint.

Like SMAW, Metal Inert Gas (MIG) welding, officially referred to as Gas Metal Arc Welding (GMAW), involves a consumable electrode which doubles as a filler [76]. Unlike SMAW, MIG utilizes a welding gun, which both feeds the electrode into the weld and shields the weld with a shielding gas, generally argon, helium or carbon dioxide. A variant of this process, Pressurized Inert Gas Metal Arc (PIGMA) welding was used to

join the beryllium rings described in Sections 1.2 and 4.1.2. PIGMA differs from standard MIG since it is performed in an inert gas chamber operating above atmospheric pressure [29].

Flux-Cored Arc Welding (FCAW) is similar to MIG welding, but the consumable electrodes used in FCAW contain flux [76]. As such, additional shielding gas is not always used. Like FCAW, Submerged Arc Welding (SAW) involves both the usage of welding flux, and a consumable electrode [76]. However, this method differs from the other arc welding methods, since the arc occurs underneath a layer of granulated flux and not in atmosphere.

Tungsten Inert Gas (TIG) welding, officially referred to as Gas Tungsten Arc Welding (GTAW), differs from the above processes since a non-consumable (tungsten) electrode is used [76]. Use of a tungsten electrode requires that the filler metal, if needed, must be added separately (e.g., [71]). Like MIG, TIG occurs in an inert gas atmosphere which is supplied by the torch (e.g., [71,76]). This gas is referred to here as the top-gas, in order to differentiate it from the additional back-gas used to shield the weld root. TIG is usually a manual process, because coordinating both the arc and the addition of filler is difficult. However, automation is possible, although it generally requires additional equipment [71].

The decoupled nature of TIG results in more flexibility and control compared to other welding methods. It is possible to weld almost all metals, including dissimilar ones, with TIG [71]. As such, all of the welds for this study were produced using manual TIG; welding parameters are provided in Section 4.1.2.

Welding geometries vary considerably, in part due to the variety of joints which may be welded. A collection of parts welded together is referred to as a weldment. Five basic joint geometries exist (Fig. 1), but every joint type has several variations (e.g., [71,75]). The Co-AgCu welds for this study are all butt welds (Fig. 1A). Exact geometry of these weldments is provided in Section 3.3.

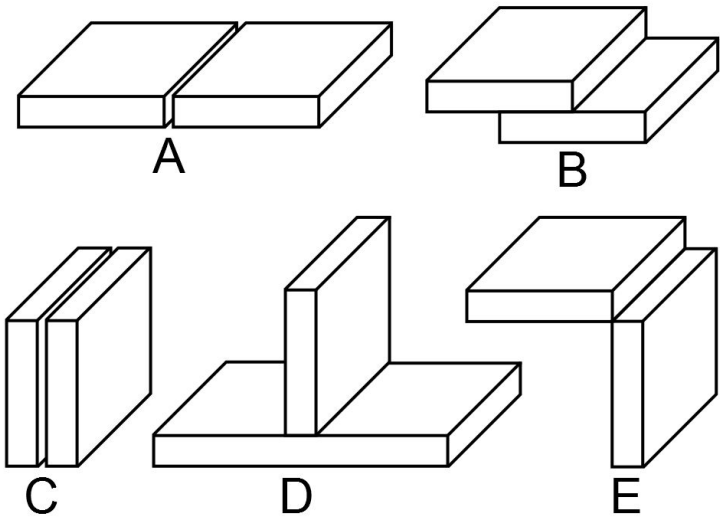

Figure 1: Five basic weld joint types
A. Butt joint. **B.** Lap joint. **C.** Edge joint **D.** Tee joint **E.** Corner joint

2.2 Metallurgy of Fusion Welds

The science of welding may be subdivided into thermal, metallurgical, or mechanical components. The thermal component governs the flow of heat, from the source, through the weld, and into the surroundings. The metallurgical component involves the variations in composition and structure during the welding process. Finally, the mechanical component involves both the internal stresses, displacements, and strains in the weld, as well as the mechanical behavior of the weldment when subjected to external forces. (see Section 2.4 for numerical techniques to address this coupling). As such, the thermal fields inside the weld greatly affect weld microstructure, thereby

altering the mechanical characteristics of the weldment. Notably, the thermal behavior of the weld directly affects grain size, dissolution and precipitation, while the latent heat of fusion and the more minor effects of other phase transformations influence the temperature field (e.g., [79]). This section considers such effects inside fusion welds.

Fusion welds are often classified according to the relationship between the base and filler metals (e.g., [71,77]). Autogenous welds are formed without a filler (e.g., [71,77]). Homogeneous welds are formed using a filler which is similar to the base metal (e.g., [71,77]). Heterogeneous welds, such as the welds in this study, use filler metals which are significantly different from the base.

2.2.1 Regions Inside Fusion Welds

Fusion welded joints generally consist of three separate regions (e.g., [77]). The fusion zone exists in the center of the weld and is composed of material which has melted. The Heat Affected Zone, or HAZ, exists to the side of the fusion zone. The material in the HAZ has not melted, but its temperature has increased enough to cause metallurgical or geometric changes. Often this results in a coarse grained area near the fusion zone (CGHAZ), and a fine grained area further away (FGHAZ) (e.g., [77]). Further still, the material has not been affected by the welding process and is referred to as the base metal.

Savage et al. [78] expanded upon this terminology by subdividing the both the fusion zone and the HAZ into two regions. The fusion zone was divided into the composite region and the unmixed zone (UMZ). The composite region consists of a mixture of base and filler metals, while the UMZ consists entirely of melted base metal [77,78]. The HAZ was divided into the True Heat Affected Zone (T-HAZ), and the

Partially Melted Zone (PMZ). The T-HAZ experiences no melting, whereas the PMZ experiences some melting due to its varied composition [77,78]. The PMZ exists in all welds produced in alloys [77]. Subsequent research has identified another region occurring in heterogenous welds, referred to as the Transition Zone (TZ) [77]. This zone occurs between the unmixed zone and the composite region [77]. Other research further divides the heat affected zone into a third region, the Intercritical Heat Affected Zone (ICHAZ) (e.g., [77]).

Specialized welds, such as the TIG welded Co-AgCu plates discussed here, may have additional regions due to the complex interactions of their constituents. The geometry of the Co-AgCu welds is discussed further in Section 4.2.1.

2.2.2 Metallurgical Effects in the True Heat Affected Zone

Microstructural effects of welding are not limited to the fusion zone, but extend to the edge of the true heat affected zone (T-HAZ) (e.g., [77,78]). This region commonly exhibits both coarse and fine grained microstructures due to its thermal history. However, compositional changes in the true heat affected zone are small, as this region does not melt.

Existence of the fine grained heat affected zone occurs because this region experiences temperatures high enough to alter material properties, but too low to cause grain growth. Metallugically this process is referred to as ‘recovery’, and involves release of residual stresses, but only minor changes in material properties (e.g., [80,81]). However, in welds, this process is often coupled with other factors. Small amounts of recrystallization may also occur, as grains formed slightly above the recovery

temperature are small (e.g., [80,81]). Additionally, allotropic phase transformations may even contribute to grain refinement, should the entire grain not simultaneously convert to the new phase. Such behavior is could occur in our welds, due to the existence of the HCP-FCC transition in cobalt.

Grain growth in the coarse grained heat affected zone occurs because this region experiences temperatures which are in excess of the recrystalization temperature but are still below the material's melting point (e.g., [77,80,81]]). The minimum temperature to form this region is approximately $T_m/2$, where T_m is the melting point [77].

Coarse-grained structures are associated with lower yield strength and higher ductility, while fine-grained structures are associated with higher yield strength and lower ductility (e.g., [80]). As such, the heat affected zone commonly consists of a weaker, ductile region surrounding a stronger, more brittle region. Furthermore, the thermal excursion experienced by the weld can exacerbate this discontinuity in properties by introducing residual stresses into the HAZ.

Additional precipitation effects may also exist inside the heat affected zone (e.g., [77]). Depending on chemistry and temperature the welds may experience precipitation hardening (e.g., [80]). However, the lack of exact temperature control makes welds susceptible to over-aging, a phenomena in which precipitates grow, rather than dissolve [77].

As both the Co-AgCu and Be-AlSi welding systems are produced using a relatively pure base metal, such reactions are expected to be of minor importance.

2.2.3 Metallurgical Effects in the Partially Melted Zone

Although the partially melted zone is generally considered part of the heat affected zone (e.g., [77]), this classification is in error since the presence of fusion is the main defining characteristic of fusion welds. As such, the partially melted zone should be considered a unique region, as it experiences incomplete melting.

The partially melted zone exists when welding alloys, as alloys do not melt at a specific point. (e.g [77]). Since all real metals have impurities, the PMZ is expected to exist in numerous welding systems, although it may be extremely small. The PMZ may form via several mechanisms, although not all are fully understood [77]. However, existence of this region implies segregation, which is generally detrimental to mechanical alloy properties (e.g [80]). However, the welds analyzed in this document were formed using a pure cobalt base, and such a region has not been observed.

2.2.4 Metallurgical Effects in the Fusion Zone

As discussed above, the fusion zone is commonly subdivided into the composite region and the unmixed zone. The unmixed zone occurs at the edge of the fusion region, and consists of melted base metal which has not interacted with the filler (e.g., [77]). Often, formation of this region is due to convective effects in the weld pool, specifically low fluid velocity near the fusion zone boundary [77].

In most welds this region is small, however the base-filler immiscibility of the Co-AgCu and Be-AlSi systems (Section 1.4) results in the existence of a significant unmixed zone. Material properties in this region are generally similar to the base metal, because their compositions are almost identical. However, the unmixed zone may have markedly

different mechanical or corrosive properties than the base metal, especially when the base and filler metals are dissimilar [77].

Unlike the unmixed zone, the composite region experiences both fusion and base-filler mixing. The main effect of mixing is referred to in welding literature as dilution, which is mathematically defined as the ratio of base metal to total metal in the composite region [71]. As such, dilution is most significant in heterogeneous welds, although it is expected to be of less importance in the Co-AgCu system, due to limited miscibility. The desirability of dilution depends on the welding system. In many heterogeneous systems dilution is undesirable since it degrades the quality of the base or the filler.

A transition zone may exist between the unmixed zone and the composite region, especially if these regions differ significantly (e.g., [77]). The composition of this transition zone varies between that of the base metal, and the composite region. As such, the microstructure of this region may differ from the other regions.

The behavior of the entire fusion zone is characterized by melting and solidification. The exact behavior of any system is complex; a function of both its chemistry and thermal history. Solidification may occur homogeneously or heterogeneously (e.g., [77]). Homogeneous nucleation occurs when solids form inside a liquid of equivalent composition, while heterogeneous nucleation requires the existence of foreign particles. Heterogeneous nucleation, especially epitaxial nucleation, is common in welds, due to the potential variations in composition. Epitaxial growth occurs when growth occurs away from a solid surface, along preexisting crystallographic planes (e.g., [77). As such, epitaxial nucleation is often competitive, since grains tend to run into each other.

A number of different solidification modes are possible for any different composition. Like most solidification processes, modes are a function of both composition, solidification rate and thermal history. Solidification modes can be considered a function of composition, solidification rate, cooling rate, and the temperature gradient at the interface, as described by the constitutional supercooling criteria (e.g., [71]). These parameters will determine the nature of the solidifying grains. The most commonly described modes are planer, cellular, columnar dendritic and equiaxed dendritic; each mode possess a unique morphology (e.g., [71]). Similarly, the grain size is also related to both the thermal gradient, and the solidification rate. Higher thermal gradients, and higher solidification rates both lead to smaller grain sizes. Since different regions inside the fusion zone experience different thermal excursions, welds may exhibit multiple solidification modes at different locations relative to the weld center.

Significant macroscopic effects also occur during weld solidification, often as an effect of weld parameters. Importantly, the shape of the weld pool itself is influenced by heat flow, weld power, and travel speed (e.g., [77]). Welds with high travel speeds, low thermal conductivity, and high heat flux generally form a characteristic teardrop shape, while slower, lower power welds, in conductive materials generally form an elliptical weld pool (e.g., [77]). Plate thickness also has an effect, with thicker plates favoring elliptical weld pools, and thin plates favoring teardrop shaped weld pools. Since weld pool shape affects the orientation of the solid-liquid interface relative to the torch direction, it will affect grain growth. In particular, elliptical weld pools exhibit more competitive grain growth than teardrop shaped pools [77]. As such, grains in teardrop

shaped pools tend to converge at the weld center, causing weakness along the weld centerline.

Critically, solidification of the weld pool tends to decrease material volume in a process referred to as ‘shrinkage’. This is a phenomenon shared with castings, (e.g., [80]). Although shrinkage occurs throughout the weld, the high temperatures and solid-liquid phase transition make its effects the most severe inside the fusion zone. Thermal and compositional gradients cause these volumetric changes to produce residual stresses. These stresses may cause local or systematic failure of the weldment. When failure occurs at high temperature, it is referred to as ‘hot tearing’, while at lower temperatures it is referred to as 'cracking’. As expected, cracking in the weld results in a significant loss of strength.

Many of the above effects influence behavior in the Co-AgCu welding system, as discussed in Sections 4.2.1 and 4.3.1.

2.3 Theoretical Analysis of Heat Flow

Analytical methods are useful for estimating weld temperature, geometry, and cooling rate. These methods involve solving the time dependent, 3-dimensional heat flow equation (e.g., [82]):

$$\frac{\partial^2 T}{\partial x^2}+\frac{\partial^2 T}{\partial y^2}+\frac{\partial^2 T}{\partial z^2}=\frac{1}{\alpha}\frac{\partial T}{\partial t} \qquad (3)$$

where x, y and z are geometric coordinates, T is the temperature, and α is the thermal diffusivity. Solving Eq. 3 generally requires simplifying assumptions. Therefore, analytical methods are difficult to apply to welds with complex geometries, multiple

materials, or variable heat flux. Modeling of manual welds is particularly difficult, since power, speed, material deposition and geometry are all variable.

2.3.1 Rosenthal's Equations

The most well-known, and also one of the earliest welding-specific solutions of Eq. 3 was developed by Rosenthal [82] to describe the temperature field of a semi-infinite plate subjected to a moving arc. Crucial to this solution are the following assumptions [82]:

1. Welding occurs during quasi-steady state
2. The welding torch can be approximated as a point source
3. Energy input is constant
4. Torch velocity is constant (and in the x direction)
5. Material properties (α,k,c,ρ) are constant
6. The heat of fusion is negligible
7. No convection occurs in the weld pool
8. The work-piece does not lose heat to the surroundings

These assumptions do not consider the effects of convection or heat loss to the surroundings. The welding torch is considered as a point source which supplies heat (Q_p) into the plate. This heat is then transferred throughout the plate via conduction.

In order for heat flow to occur in a quasi-steady state, the temperature field around the constant velocity heat source must be constant ($dT/dt = 0$); therefore the general heat flow equation is expressed in a moving reference frame [82]:

$$\frac{\partial^2 T}{\partial \xi^2}+\frac{\partial^2 T}{\partial y^2}+\frac{\partial^2 T}{\partial z^2}=-\frac{v}{\alpha}\frac{\partial T}{\partial \xi}+\frac{1}{\alpha}\frac{\partial T}{\partial t} \tag{4}$$

where

$$\xi = x - vt\,. \tag{5}$$

and v is the heat source velocity. Applying the quasi-steady state assumption simplifies Eq. 4 into [82]:

$$\frac{\partial^2 T}{\partial \xi^2}+\frac{\partial^2 T}{\partial y^2}+\frac{\partial^2 T}{\partial z^2}=-\frac{v}{\alpha}\frac{\partial T}{\partial \xi} \tag{6}$$

Rosenthal [82] solved Eq. 6 for both two and three dimensional heat flow, using a modified coordinate system such that the origin occurs at the torch. Since the torch is considered a point source, and the work-piece does not lose heat to its surroundings, the heat flux through any hemisphere surrounding the torch must approach the value of the total heat (Q) as the radius of the hemisphere (R) approaches zero [82]. This can be expressed mathematically as [82]:

$$-2\pi R^2 k\frac{\partial T}{\partial R}\to Q \text{ as } R=\sqrt{\zeta^2+y^2+z^2}\to 0 \tag{7}$$

where k is thermal conductivity. Solution of Eq. 6 now requires establishment of boundary conditions. Since there is no transference of heat from the work-piece to the surroundings the temperature field at the top of the plate must obey [82]:

$$\frac{\partial T}{\partial z}=0 \text{ for } z=0 \text{ and } R\neq 0 \tag{8}$$

As the plate is semi-infinite, the temperature of the plate far from the torch must remain unchanged, i.e. [82],

$$T=T_0 \text{ for } R=\infty \tag{9}$$

Solving Eq. 6, using the boundary conditions expressed in Eqs. 7-9 yields Rosenthal's 3-dimensional solution (e.g., [71]):

$$T - T_0 = \frac{Q}{2\pi kR} e^{\left(\frac{-v(R+x)}{2\alpha}\right)} \tag{10}$$

where Q is heat transferred by the torch (Watts), x is the distance from the torch along the weld centerline in the weld direction, R is the total distance from the torch, and α is the thermal diffusivity. The 3-dimensional solution is valid for welds performed on thick plates. However, Rosenthal's assumptions are not valid for temperatures inside the fusion zone, as a temperature singularity is predicted at the torch.

The above procedure can also be applied to thin plates (e.g., [82]). In the case of a thin plate, no heat may be transferred at the bottom of the plate, i.e. [82],

$$\frac{\partial T}{\partial z} = 0 \text{ for } z = g \tag{11}$$

where g is the work-piece thickness. Solving Eq. 6, using the boundary conditions given in Eqs. 7,8,9,11 yields Rosenthal's 2-dimensional solution (e.g., [71]):

$$T - T_0 = \frac{Q}{2\pi kg} K_0\left(\frac{vR}{2\alpha}\right) e^{\left(-\frac{vx}{2\alpha}\right)} \tag{12}$$

where symbols are as above, and K_0 is the zero-order, modified Bessel function of the second kind. This solution is valid for heat flow in thin plates. Like Rosenthal's 3-dimensional solution (Eq. 10), Rosenthal's 2-dimensional solution (Eq. 12) is also inaccurate for temperatures inside the fusion zone.

Some disagreement exists in the literature regarding the exact Bessel function used in these equations (cf. [71,72]). This disagreement is likely a result of ambiguity in Rosenthal's original work [82]. However, both the symbol used by Rosenthal (K_0) and

the form of the solution indicate that the intended function is a modified Bessel function of the second kind, zero order.

The highest cooling rates will occur along the *x*-axis when *x* is negative [82]. During these conditions, Eq. 10 reduces to [83]:

$$T - T_0 = \frac{Q}{2\pi kx} \tag{13}$$

Taking the derivative of Eq. 13 with time yields the cooling rate for a weld in a thick plate [82]:

$$\frac{\partial T}{\partial t} = -\frac{2\pi kv}{Q}\left(T - T_0\right)^2 \tag{14}$$

A similar procedure yields the cooling rate for a weld in a thin plate [83]:

$$\frac{\partial T}{\partial t} = -\frac{2\pi k^2}{\alpha}\left(\frac{vg}{Q}\right)^2\left(T - T_0\right)^3 \tag{15}$$

The above analysis requires that thermal properties remain constant, despite significant changes in temperature. This assumption is severely flawed, as thermal properties vary significantly as a function of temperature [72]. Furthermore, this analysis assumes that the heat source functions as a point source. As a result, there is a temperature singularity at the torch center. Due to these assumptions, Rosenthal's equations are not capable of accurately predicting temperatures inside the weld pool.

2.3.2 Analysis of Peak Temperatures

Adams [83] modified Rosenthal's equations (Eqs. 10,12) to calculate the peak temperatures experienced in the weld. First, Rosenthal's 3-dimensional solution (Eq. 10) was expressed as:

$$T' - T_0 = \frac{Qv}{4\pi k\alpha}\frac{e^{\left(m-\sqrt{m^2+n^2}\right)}}{\sqrt{m^2+n^2}}, \qquad m = -\frac{vx}{2\alpha}, \quad n = \frac{vR}{2\alpha} \tag{16}$$

The location of the points at peak temperatures occurs when the isotherm is tangent to the *x*-axis. Expressed mathematically [83]:

$$\left.\frac{\partial n}{\partial m}\right)_{T'} = 0 \tag{17}$$

where T' is the temperature of the isotherm under analysis. The locus of the peak temperature is given by [83]:

$$m^2 + n^2 = m\left(1 + \sqrt{m^2+n^2}\right) \tag{18}$$

Generally, *n* is larger than *m*, so that [83]:

$$\sqrt{m^2+n^2} \cong m\left(1 + \left(n^2/2m^2\right)\right) \tag{19}$$

Eq. 18 then reduces to [83]:

$$n^2 \cong 2m \tag{20}$$

Substituting the above approximation back into Eq. 16 yields Adam's solution for peak temperature (T_p) in a welded, thick plate [83]:

$$T_P - T_0 = \frac{Qv}{2\pi k\alpha e}\frac{1}{2+n^2} \tag{21}$$

Due to its underlying assumptions, the Rosenthal equations (Eqs. 10,12) are unlikely to correctly predict temperature inside the fusion zone. Adams rewrote Eq. 21 to describe the peak temperature as a function of the distance from the fusion zone, resulting in:

$$\frac{1}{T_P - T_0} = \frac{2\pi k \alpha e}{Qv}\left[2 + \left(\frac{vR'}{2\alpha}\right)^2\right] + \frac{1}{T_m - T_0} \tag{22}$$

where R' is the distance from the edge of the fusion zone and T_m is the melting point. Repeating the above analysis using Eq. 12 yields the following expression of Rosenthal's 2-dimensional solution [83]:

$$T' - T_0 = \frac{Q}{2\pi kg} K_0\left(\sqrt{m^2 + n^2}\right) e^{(m)} \tag{23}$$

The locus of peak temperature is given by [83]:

$$m^2 + n^2 = m\left(\tfrac{1}{2} + \sqrt{m^2 + n^2}\right) \tag{24}$$

Combining Eqs. 19, 23 and 24 yields Adams solution for peak temperature in a welded thin plate [83]:

$$T_P - T_0 = \frac{Q}{2kgn\sqrt{2\pi e}} \tag{25}$$

The equation for peak temperature as a function of distance from the fusion zone is given by [83]:

$$\frac{1}{T_P - T_0} = \frac{vR'k\sqrt{2\pi e}}{Q\alpha} + \frac{1}{T_m - T_0} \tag{26}$$

2.3.3 Numerical Analysis of Rosenthal's Three-Dimensional Equation

Further analysis of Eq. 10 may be performed by expressing it in dimensionless form, before numerical solution [84]. This may be done using the following substitutions (e.g., [85]):

$$\theta = \frac{T(r) - T_0}{T_C - T_0}, \quad \lambda = \frac{vx}{2\alpha}, \quad \phi = \frac{vy}{2\alpha}, \quad \zeta = \frac{vz}{2\alpha}, \quad \Delta = \frac{vr}{2\alpha} = \sqrt{\left(\lambda^2 + \phi^2 + \zeta^2\right)} \quad (27)$$

where T_C is the chosen reference temperature, and other values are as previously defined. Direct substitution of these terms into Eq. 10 yields (e.g., [85]) :

$$\theta = \left[\frac{Qv}{4\pi k\alpha\left(T_F - T_o\right)}\right]\frac{e^{-(\Delta+\lambda)}}{\Delta}. \quad (28)$$

The bracketed term is generally referred to as the operating parameter, n, for which

$$n = \left[\frac{Qv}{4\pi k\alpha\left(T_F - T_o\right)}\right]. \quad (29)$$

For arc-welding processes, heat is often related to process efficiency (η) such that (e.g., [72, 86]):

$$Q = \eta EI \quad (30)$$

where E is voltage, and I is current. Process transfer efficiency has been determined for multiple welding systems by calorimetry [86]. Substituting Eq. 30 into Eq. 29 relates the operating parameter with the physical welding parameters (E,I,v) such that

$$n = \left[\frac{\eta EIv}{4\pi k\alpha\left(T_F - T_o\right)}\right] \quad (31)$$

Numerical solution of Eq. 28 allows weld geometry, specifically the maximum extent of weld isotherms, to be related to the operating parameter, n [84]. Usage of Eq. 31 allows weld shape to be related to the physical welding parameters (E,I,v) [84].

2.3.4 Further Analysis of the Rosenthal Equations

Several notable attempts have been made to improve upon Rosenthal's solutions. Udin et al. [87] developed an analytical description of temperature in a plate of intermediate thickness. Eager and Tsai considered thermal fields resulting from a torch with a Gaussian heat distribution [88]. Nunes developed an extended model, which includes effects from both the circulation of the weld pool, and the phase change experienced inside the fusion zone [89]. Malmuth et al. [90] addressed heat loss due to a weld backing.

Unfortunately, such analytical attempts have only met with limited success, mainly due to the number of assumptions required [72].

2.4 Numerical Analysis of Welding

Numerical modeling has largely replaced the theoretical solutions described above, due to the complexity of welding, and the number of important secondary effects which analytical models ignore [71,72]. In particular, the assumptions required for theoretical approaches (Section 2.3.1) are not required for numerical solution [86]. As such, numerical solutions are often more accurate and more applicable than theoretical approaches.

Due to the importance of welding to industry, multiple welding specific FEA programs exist. These include simufact.welding and ESI's Virtual Welding and Assembly Suite, powered by the WELDSIM and SYSWELD solvers respectively [91,92]. Specialized finite element solvers, such as these, are capable of modeling most of the above issues utilizing coupled thermal-microstructural-mechanical analysis [79].

The relationships between these aspects are non-trivial. Macroscopically, the weld can be interpreted thermo-mechanically, with temperature influencing displacement, stress, and strain, and plastic work effecting temperature (e.g., [79]). Microscopically, the weld can be analyzed based on the metallurgical relationships between temperature, phase transformations, grain growth, dissolution, and precipitation (e.g., [79]). Finally, microstructure has a significant influence on mechanical behavior, since material properties are affected, whereas mechanical deformation alters transformation rates, thereby affecting microsctructure (e.g., [79]).

The emphasis on changing microstructure separates welding specific FEA software with more generic varieties. Welding specific codes use microstructural models, generally developed for common materials such as aluminum or steel, to relate materials, temperatures, and microstructures. The results of these calculations are stored as scalar fields representing the volume fractions of the different phases, the compositions of these phases, and the grain size at different points in the weld [79]. This allows prediction of material properties based on experimental data, or preexisting models.

Important secondary effects which can be addressed using such numerical methods include [71, 91]:

1. Complex geometries
2. Temperature dependent thermal properties
3. Compositional gradients
4. Material deposition
5. Complex heat sources
6. Variable welding parameters
7. Complex boundary conditions
8. Heat of fusion.

However, thermal-microstructural-mechanical analysis is not suited for fluid dynamics calculations, specifically calculations involving convection in the fusion zone. These calculations are of limited commercial interest, because the effect of convection on the stress field is usually negligible [79]. However, correct modeling of fluid dynamics is necessary to precisely predict geometry near the weld pool [79]. Much research has been done in this area using a variety of methods, including finite difference [93], discrete element analysis [94], and finite volume [95, 96].

Despite the potential applicability thermo-mechanical-microstructural analysis, development of such models is beyond the scope of this dissertation. However, substantial material property data, welding parameter data, and weld temperature data has been recorded to facilitate future numerical analysis.

Chapter 3. Materials, Experiments and Techniques

3.1 Welding Materials

The base material was 99.95% pure cobalt (Sophisticated Alloys). Prior to welding, Co was hot-rolled to 7.6 mm and heat treated at either 325°C or 350°C to homogenize the grain structure of the metal. However, some studies [97] have reported the persistence of the FCC phase after refining the grain structure by rolling. In order to ensure that no FCC material was present, the cobalt was again heat treated at either 350°±10°C, or 325°±10°C for 100 hours, and then allowed to slowly cool. For the second heat treatment, the temperature was measured at various locations to ensure consistency.

A majority of the experiments were performed on cobalt samples after a heat treatment of 325°C, with the exception of a few early incomplete welds. Neither heat treatment produced detectable quantities of FCC cobalt [22].

The filler selected was 60-40at.% AgCu wire (Lucas Milhaupt), which is at the eutectic point. It is available from a number of sources, and often referred to by its AWS specification, BAg-8 [98].

3.2 XRD Characterization

One of the heat-treated blocks and an unheated blank were sectioned to expose three orthogonal faces. X-ray diffraction was performed with a Rigaku Geigerflex D-MAX/A Diffractometer at Washington University in St. Louis using Cu-Kα radiation. The voltage and current used were 35kV and 35mA, respectively. No noticeable FCC

peaks were found on any of these 6 faces, allowing the conclusion that neither treatment nor hot-rolling had induced any persistent FCC structures significant to these experiments.

3.3 Welding Equipment, Materials, and Parameters

Optimization of weld parameters requires consistency. In order to reduce uncertainty, all welds were produced by the same ASME aerospace certified welder on a TIG Welder with high-frequency stabilization (Miller Aerowave) set to direct current electron negative (DCEN).

The standardized weld part used in this study was a 76 mm long, 25.4 mm wide, 6.35 mm thick block of 99.95% cobalt with a 3.2 mm radius J-groove (Fig. 2). These parts were precision machined, so that the thicknesses of the J-groove and part were accurate to 0.08 mm.

The parts were held with a specially built clamp during welding, which rigidly positioned the cobalt plates above a crushed refractory substrate. This permitted argon back-gas to shield the weld, while still reflecting heat back onto the weld base.

All welds involve 5 passes, in alternating directions, with 0.25 liter/s Ar back-gas and He or Ar top-gas (Fig. 2A). Passes 1-4 were done at 225 A, with 0.43 liter/s He top-gas, while pass 5 was 150 A with 0.25 liter/s Ar top-gas. Passes 1 and 2 were centered, whereas passes 3 and 4 were to either side of the original J-groove (Fig. 2B). The final pass was done in an oscillating trajectory. The weldments were allowed to cool to room temperature after passes 2, 3, and 4.

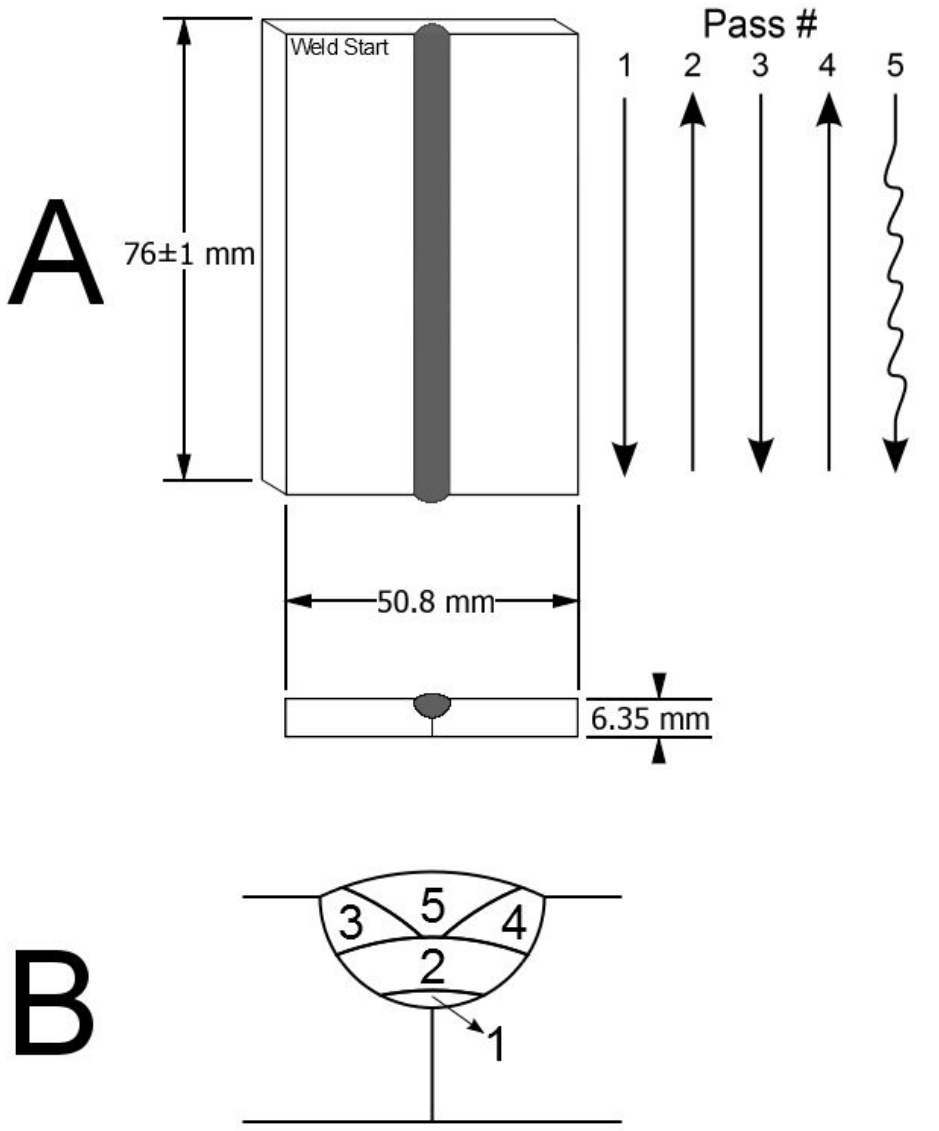

Figure 2: Co-AgCu weld schematics

A. Schematic showing approximate pass locations, directions, and weldment geometry used in surrogate Co-AgCu TIG welds. Two cobalt samples sharing a single U-groove are joined by 5 passes in alternating directions. The final, oscillating pass is indicated by a wavy line.

B. Approximate weld-bead locations are given in the section view. Dimensions are all ±0.08 mm unless noted otherwise.

Weld power was controlled via foot pedal. The first pass was usually conducted at the 225A limit. All other passes were performed at around 100-150A. In an effort to maximize penetration, the torch was held in a vertical position for passes 1 and 2. For passes 3 and 4, the torch was oriented at an approximately 15-30° angle from vertical,

towards the corner of the U-groove, but was still held perpendicular to the travel direction. Torch position varied during the final, oscillatory pass, as deep penetration was no longer desirable. The torch height was approximately 1.6 mm for all passes. Methods used to measure weld power are discussed in section 3.12, while results of these measurements are presented in section 4.1.2.

Filler deposition was highly variable. Pass 1 involved almost no filler deposition, while passes 2-4 almost entirely fill the weld groove. Pass 5 used the minimum amount of filler required to smooth the weld. Filler was added incrementally as series of approximately 20-25 dabs per pass. Structural effects due to these different passes is discussed further in section 4.2.1, while the effect of incremental filler addition is discussed in section 4.3.1.

Power, filler deposition, and traverse speed are linked. Traverse speed for the above parameters is approximately 2.5 mm/s for passes 1-4, and 1 mm/s for pass 5. The slower speed for pass 5 does not account for the greater distance traveled during oscillation.

Substitution of personnel or equipment is expected to require modification of these welding parameters. Therefore, these parameters are presented as guidelines, which should enable experimental reproduction after slight adjustment.

Further explanation of these welding parameters, along with the study that determined them, is provided in section 4.1.

3.4 Fracture in Tension and Four-Point Bending

Welds were fractured both in tension and in a 4-point bending apparatus, using an Instron 3307 tensile tester. These tests were performed in order to evaluate the quality of the weld and of the welding technique, and to produce failures for fractography and statistical analysis.

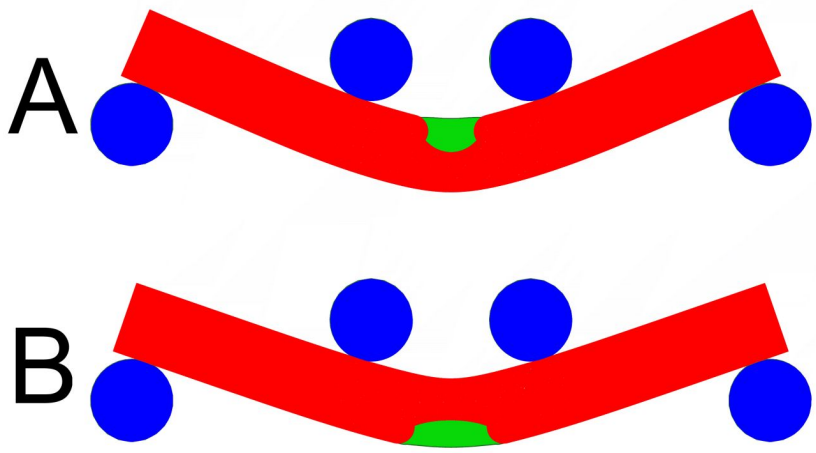

Figure 3: Traverse root and face bending orientations
A: Root bending orientation. Section and filler (red and green) subjected to root bending by AISI 304 steel rollers (blue).
B: Face bending orientation. Section and filler (red and green) subjected to face bending by AISI 304 steel rollers (blue).

Images produced from 2D Abaqus contact models.

Four-point bending was performed on 9 completed welds, 4 incomplete welds, and 4 machined cobalt blanks using both transverse root bending (Fig. 3A) and transverse face bending (Fig. 3B). Two of the completed welds were heat treated, while the remainder were left as is. These bending orientations correspond to the ASTM weld bending standard [99], although the testing jig here differs by having 4 rollers (Fig. 3) rather than a guided bend fixture. For brevity, these tests will be referred to as root bending and face bending, respectively.

3.4.1 Root Bending Tests of Different Weld Stages

Early tests focused on perfecting the methods and techniques used to weld the Co-AgCu surrogate. The quality of these welds was determined by root bending. The orientation of the welds during fracture (Fig. 3) was selected such that fracture would occur at the base of the weld. This orientation corresponds to the expected failure direction due to the residual stresses induced by CTE. The bending apparatus was set to have a 48 mm support span and a 12 mm load span. The load span was chosen to be slightly larger than the expected width of the weld pool, while the support span was as wide as the weld geometry would allow (Fig. 3). No extensometer was employed during the tests, resulting in data that is accurate for loads, but provides displacements that are generally overestimated.

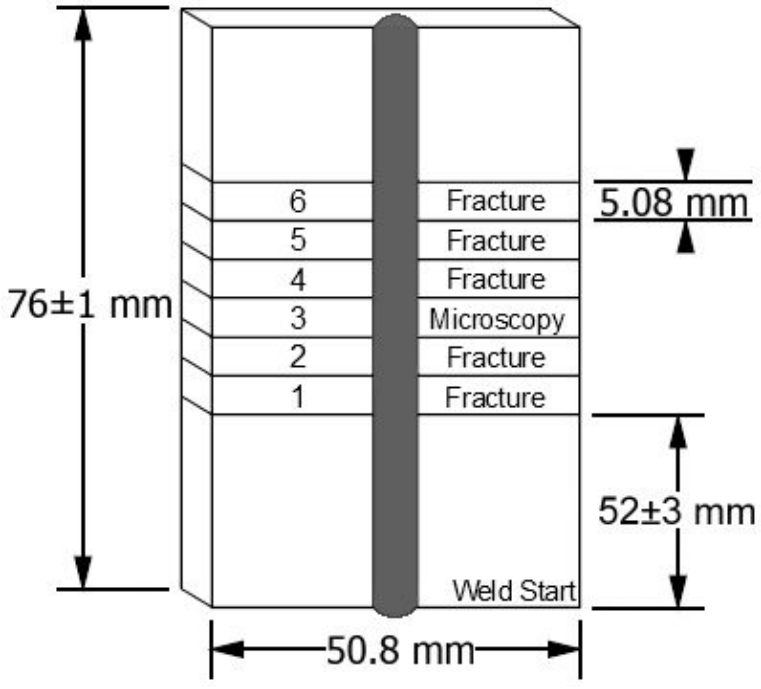

Figure 4: Weld schematics

Schematic shows basic weldment geometry and the locations for fracture and microscopy sections used in the study of differing weld stages. Section numbers are provided on the left. The sections are all undersized by approximately .35 mm due to the width of the EDM wire. Dimensions are all ±.08 mm unless noted otherwise.

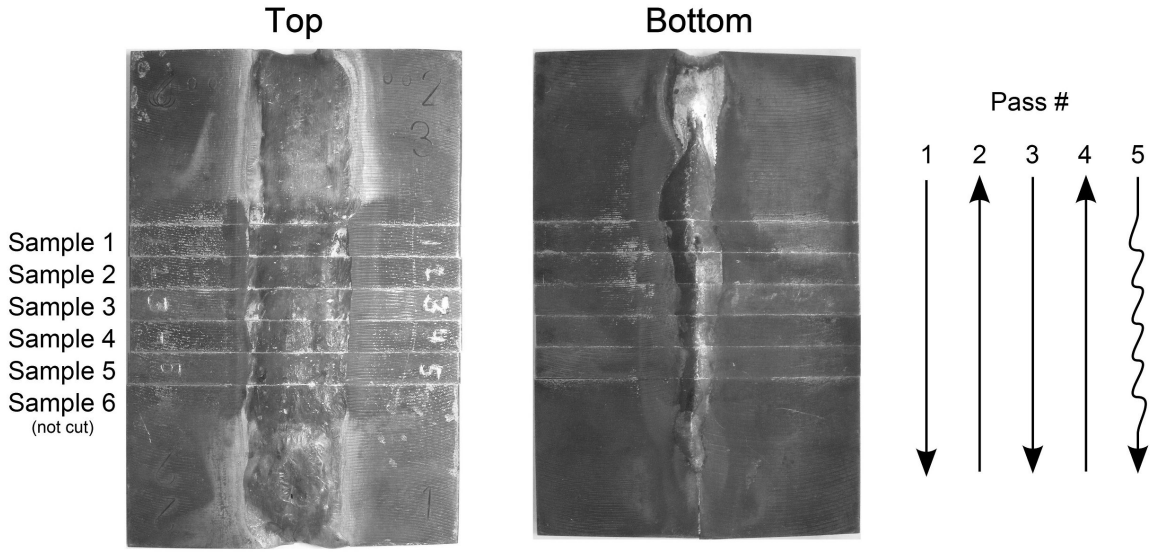

Figure 5: 5-pass weld showing section locations and welding direction
Top and bottom images of a 5 pass weld, after sectioning for the weld stage study. Sample 6 has not yet been cut. Notice the large weld pool at the start of the weld, tapering away toward the base. This shape has been observed in a large percentage of these Co-AgCu welds, and indicates the welding power was too low. The alternating welding direction was selected in order to minimize thermal gradients due to the small length of these welds. The final, oscillating 'filler' pass is designated by a wavy line.

To perform these tests, the welds are cut into 8 parts; 2 end pieces and 6 sections (Figs. 4, 5). These welds were not ground, but were fractured with their entire cross section intact. The end pieces were not used due to the unstable nature of the transient region. The asymmetrical sectioning (Fig. 4) reflects the estimated location of the quasi-steady zone. Section 3 was not usually fractured, but was instead preserved for microscopy. These tests were then compared with 4-point bending tests on four samples, made from the pre-welded, heat-treated cobalt block, to compare the quality of the Co-AgCu welds to the parent material. These samples have the same single-U geometry as our welds, but were cut out of a single piece of cobalt (Fig. 6).

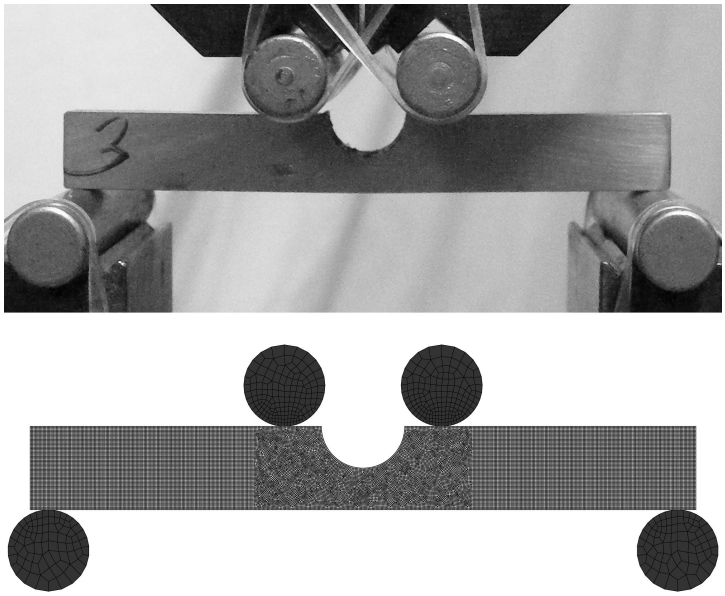

Figure 6: Fracture setup, and its corresponding FEA
Photograph captures the 4pt bending apparatus fracturing a blank specimen, while the computer image shows element size and orientation in the corresponding FEA. Fracture setup is intended to mimic "natural" failure of the welds, due to CTE mismatch and expected grain orientation.

3.4.2 Tension Test

Once the Co-AgCu welding methods were determined, several further fracture tests, involving both tension and four-point bending, were performed in order to understand the behavior of this welding system. To perform the tension test, the weld was first precision ground until it had an orthogonal cross section. It was then sectioned in an electrical discharge machine EDM into 8 test pieces (Fig. 7A), and loaded into a specially made fixture (Fig. 7B). Displacement was measured with a deflectometer (Fig. 7B). Results were compared to finite element models (Fig. 7C).

To perform the four-point bending test, the tester was set up as before, with a 48 mm support span and a 12 mm load span. No extensometer was fitted, resulted in accurate load data, but overestimated displacement data. Unlike the earlier tests, a majority of these tests were ground until their cross section was orthogonal.

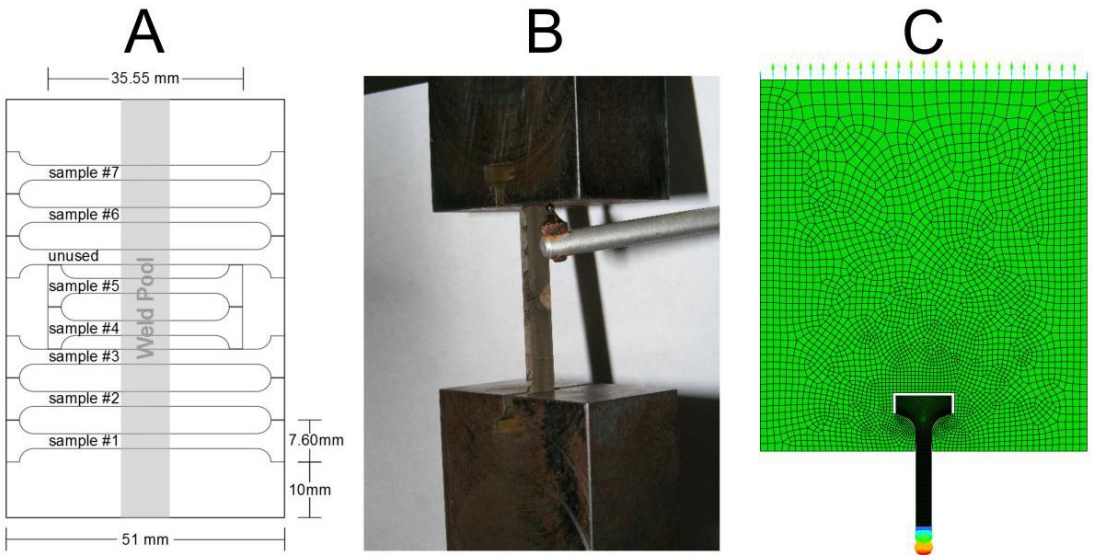

Figure 7: Tension test pieces, tension test, and FEA model

A: Schematic shows locations and size of the test pieces. All test pieces have identical geometry except for their lengths. One test piece was unused due to machining defect.

B: Test piece being fractured in tension grips, showing location of filler pool, and use of deflectometer.

C: FEA model showing half symmetry test piece in tension. The large green area is the fixture; the test piece is dark due to the small size of its mesh. Arrows at the top are forces due to displacement, colored areas at the bottom are force vectors due to symmetric boundary conditions.

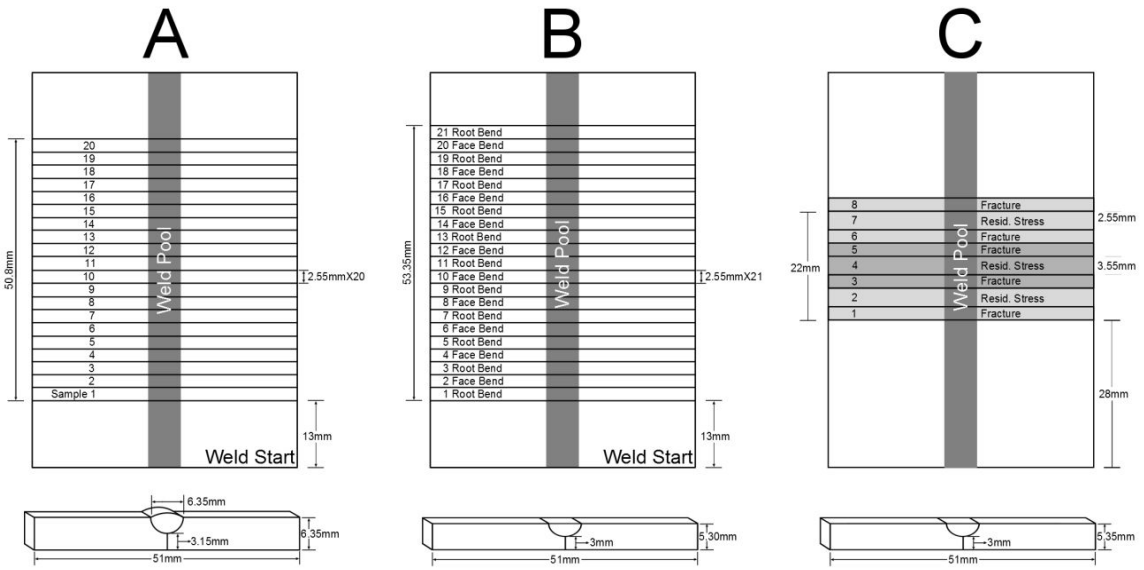

Figure 8: Sectioning for four-point bending, heat treatment, and residual stress measurement

A: Schematic shows section positions and dimensions for the 20 section, unground root bending test. A single unground weld, with an intact filler and base pool was used in this test.

B: Schematic shows section positions and dimensions for the 21 section alternating face and root bending test. Three separate welds were used in these tests.

C: Schematic shows section positions, dimensions and heat treatments for the crack compliance method and root bending tests. Four welds were used in these tests. A heat treatment of 325°C for 100 hours was applied to either sections 3-5, or 1-2, 6-8, as indicated by the different shading. Sections used for residual stress measurement are larger, to accommodate the strain gauge.

3.4.3 Root and Face Bending Tests of Completed Welds

One weld was EDM cut into 20 sections but not ground (Fig. 8A). Fracture was performed in the root bending orientation, and compared to the completed (5 pass) weld used in the earlier root-bending tests (Section 3.4.1).

Three welds were ground until flat, and then cut with an EDM into 21 sections (Fig. 8B). Root and face bending were applied alternately to adjacent sections. Results were compared to finite element models.

Four welds were used in a combined residual stress and heat treatment study. These welds were also ground, before being sectioned into 4 fracture and 4 residual stress specimens (Fig. 8C). Half of the fracture sections and half of the residual stress sections were heat treated at 325±2°C for 100 hours. Fracture was performed in the root bending orientation. Results were compared to finite element models.

3.5 Optical Microscopy & Etching

Optical microscopy was performed on chemically etched sections in order to reveal both the microstructure and macrostructure of the welds. Two etchants were sequentially used. The first etch was composed of a solution of 60 ml hydrochloric acid, 15 ml nitric acid, 10 ml water, and 15 ml acetic acid. The section was then placed in a secondary solution of 60 ml nitric acid and 40 ml methanol which was slowly diluted by a 1-1 water-methanol mixture before being quenched by water (modified from [100]). All images were produced on faces located exactly 40.6 mm from the weld start (Fig. 9).

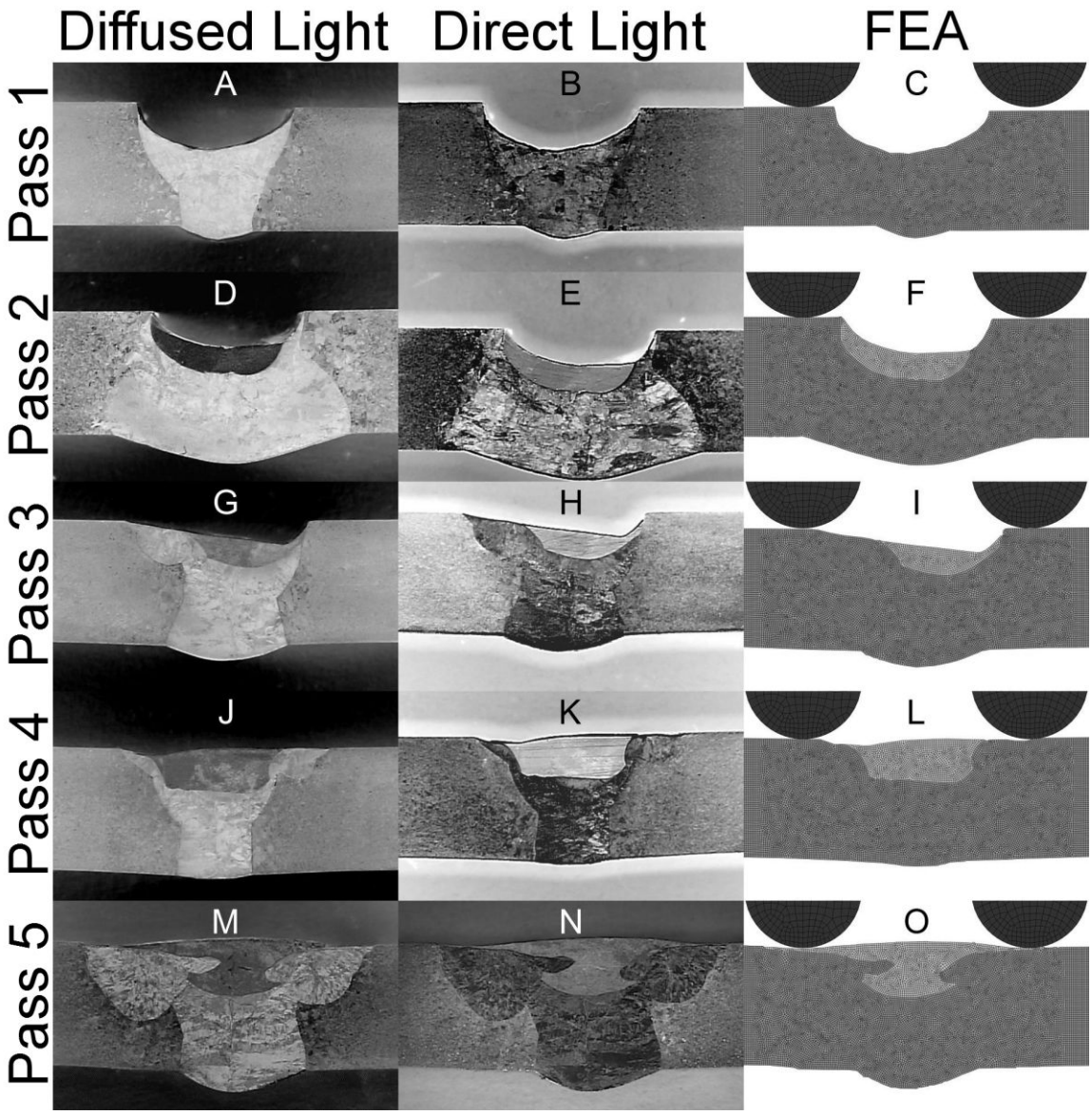

Figure 9: Welds sectioned at increasing number of passes

Microscopic images using diffused light and color inversion are shown to the left; direct light is in the middle, and the corresponding FEA model is to the right. The FEA models contain the base, as well as two of the rollers used in 4-point bending. In all images, the silver filler is located up. The different colored area surrounding the filler in the microscopic images is the cobalt which has been melted. The areas on either side of the melted region is the HAZ, which exhibits grain growth. All welds contain backfilled cracks, but they are most obvious in welds 2 (**DE**) and 5 (**MN**) . All welds show grain growth originating at the center. Close inspection of the images shows an area immediately under the filler pool which forms an arc. This area is most visible in **G** and **H**; it is suspected the different grain structure is due to the formation of a Cu-Co alloy.

Etching using this procedure was performed on all of the intermediate stages of the weld. These images were taken with indirect light using digital color inversion (Fig. 9, left column), and direct light (Fig. 9, middle column).

3.6 Optical Microscopy with Polishing Slurry

To reveal machining inconsistency, as well as sufficiently large grain structures, a new, simple method of sample preparation was developed. First, the sample is ground to a high degree of flatness using a granite block and 1500 grit paper [23]. A slurry is then prepared from a mixture of silicon carbide, alumina, and water. By carefully removing the sample from the polishing surface, surface tension adhered the slurry to the sample, permitting surface deviations to be revealed during optical microscopy. Although this method does not reveal fine detail, it is faster than etching, and can be performed utilizing only sandpaper, polishing compound, a polishing block, and a camera with a macro lens.

3.7 Scanning Electron Microscopy (SEM) and Energy Dispersive X-ray Spectroscopy (EDS)

Imaging and compositional analysis was performed on a Phillips XL30 ESEM with an Oxford EDS attachment. Images were taken after etching as described above, as well as after fracture in tension and 4-point bending. Images of the etched section were formed using both secondary electrons and EDS, on an uncoated section. Images of the 4-point bending sections were also taken using secondary electrons, but these were first polished and iridium coated. Only the strongest and weakest sections were examined. Fractography was also performed after tension, on the uncoated failure surface of the

strongest test piece. Compositional analysis was performed at areas of interest utilizing the EDS attachment. Concentrations of Ag, C, Co, Cu and O were measured, but percentages of C and O were removed during analysis.

3.8 Spatially Resolved Acoustic Spectroscopy (SRAS)

Two welds were sectioned along the direction of welding, in the weld center. Two SRAS scans were performed on each weld, one with the wave propagation direction aligned with the long edge of the sample and the other orthogonal to this. The projected fringe pattern had a spacing of 23.6 microns and so the measured acoustic frequency range was ~100-140MHz. The acoustic generation patch size was 120 microns giving a spatial resolution on the order of 60 microns.

The weldments studied have a predominantly hexagonally close packed cobalt base. Due to the geometry of this crystal structure, SRAS can provide some indication of c-axis orientation by combining two maps with orthogonal propagation directions. Regions where the measured surface acoustic wave velocity is ‘fast’ for both propagation directions are basal, for ‘fast/slow’ or ‘slow/fast’ combinations the c-axis lies orthogonal or in line with the scan direction, respectively.

During the SRAS scan the amount of reflected probe light is also recorded, allowing a high contrast / high resolution optical image to be obtained, showing surface features such as the base-filler boundary and crack locations.

3.9 Electron Microprobe and Wavelength Dispersive Analysis (WDS)

A completed weld section was characterized by wavelength dispersive analysis (WDS) and standard procedures on the JXA-8200 electron microprobe at Washington University, using "Probe for EPMA" for data reduction (see http//www.probesoftware.com/). The measured data was corrected with CITZAF after [101]. Pure Ag and Co were used as standards for their respective elements, while cartridge brass (NIST) was used as a standard for Cu.

Locations of the WDS measurements are overlaid on micrographs of the weld section, created using electron backscatter as well as optical microscopy. Optical micrographs were taken after the weldment was sequentially etched by an aqua regia based mixture and nital. Full description of the methods used to produce these images is given in Section 3.5. Electron backscatter images were created using the microprobe software described above.

3.10 Finite Element Analysis (FEA) of Fracture

Four sets of finite element fracture models were created using Abaqus. The first set of models consists of two-dimensional models of the root bending test of different weld stages (Section 3.4.1). The second set of models are three-dimensional representations of the tension test (Section 3.4.2). The third set are two-dimensional representations of the face and root bending tests (Section 3.4.3). The fourth set are also 2-dimensional representations of the root bending tests used in the residual stress study (Section 3.4.3).

All models are entirely mechanical, and do not involve welding thermodynamics or microstructural changes. The welds were considered to consist of two regions, a filler,

assumed to consist of AgCu, and a base, assumed to consist of pure cobalt. Both of these materials were modeled using experimental data. Section 3.10.1 covers the modifications which were made to convert this data into true stresses and strains, while section 1.4 explains the Voigt-Reuss-Hill average used to approximate some of the properties of AgCu. Microstructural details, such as grain alignment or backfilled cracks, were not considered. Cross-sectional weld geometry was not considered to vary inside parts.

Failure was predicted when stresses in either material exceeded its measured yield strength. Adhesion between the base and filler was considered to be perfect. As such, failure due to delamination was predicted to occur should the interface experience stresses in excess of the predicted AgCu ultimate strength.

3.10.1 FEA Material Parameters

All of these finite element models utilize only three different materials. The filler is assumed to consist of AgCu, the base is assumed to consist of pure Co, and the fixtures are assumed to consist of AISI 304 steel. Both the Co base and the AgCu filler are assumed to undergo plastic deformation,, while the AISI fixtures are assumed to be completely elastic. The AgCu filler and Co base are assumed to follow metal plasticity, as defined by Abaqus, using the von Mises yield surface. Elastic data for both pure cobalt and AISI 304 steel was provided by Smithells [26], whereas elastic data for the AgCu was approximated using the Voigt-Reuss-Hill average (Eq. 1, Table 4).

Plasticity data for both Co and AgCu was extrapolated from published experimental results [102,103]. This extrapolation was done by assuming that the true stress (σ_t) and true strain (ε_t) are related to engineering stress (σ_E) and measured strain (ε_m) by:

$$\sigma_t \cong \sigma_E\left(1+\varepsilon_E\right)=\sigma_E\left(1+\varepsilon_m-\frac{\sigma_E}{b}\right) \tag{32a}$$

$$\varepsilon_t \cong \ln\left(1+\varepsilon_E\right)=\ln\left(1+\varepsilon_m-\frac{\sigma_E}{b}\right) \tag{32b}$$

where b is the spring constant of the testing machine. These equations assume incompressible materials, and a linear deflection of the testing machine with load. In order to calculate these results, the Young's modulus of cobalt was assumed to be 211 GPa [26] while silver-copper was assumed to have a Young's modulus of 95 GPa (Table 4), calculated as an approximate midpoint between the Reuss and Voigt averages for these materials. These assumed values for the moduli allowed calculation of the true stresses and strains from reported data by solving for the spring constant using only data from the elastic region and the equation:

$$b \cong \frac{\sigma_E^2}{\sigma_E\varepsilon_m + EW\left(-\frac{\sigma_E}{b}\right)+\sigma_E} \tag{33}$$

where W is the Lambert function:

$$W\left(z\right)e^{W(z)}=z \tag{34}$$

Using these equations, tensile results for AgCu and annealed cobalt were transferred into true stress and strain (Fig. 10**,** Table 5), and used in the finite element models.

Table 5: FEA material parameters
(4 Significant Figures)

Material	Location	Young's Modulus (GPa)	Poisson's Ratio	Plasticity Law	UTS (MPa)	Max Equivalent Plastic Strain
AISI 316	Rollers/ Tensile fixture	215	0.283	N/A	N/A	N/A
Cobalt	Weld Base	211	0.32	Mises	949.1	0.1727
72/28 AgCu	Weld Filler	95.37	0.3593	Mises	302	0.3136

3.10.2 FEA of Sections Fractured at Various Welding Stages

Models of these fracture tests (Section 3.4.1) were created in Abaqus from microscopic images (Fig. 6, bottom, Fig. 9, right column). These finite element analysis (FEA) models are two-dimensional, assume plane stress, and apply loads via frictionless contact with 4 rollers (Fig. 6). The model is displacement-controlled in order to reduce instabilities. Material parameters are described above (Section 3.10.1, Table 5). The standard, implicit problem solver was used, with a maximum time step corresponding to an approximate deflection of $5x10^{-4}$ mm.

Geometry was extrapolated by manually outlining the images and converting this outline to a DXF file, which was then uploaded into Abaqus, where it was scaled and rotated into position. Mesh sizes in the sample varied slightly, but corresponded to a seed length of 0.1 mm (Fig. 6, bottom, Fig. 9, right column). Mesh sizes in the rollers were coarser, which is of little consequence because the material is assumed to be elastic.

To replicate 4-point bending, the model assumes that the bottom rollers are stationary, and the top rollers are capable of motion only along the Y (vertical) axis. The 4-point bending is modeled as contact between the plastic ('slave') sample surface, and the elastic ('master') roller surface, and assumes a frictionless interface. The sample is

locked in place by assuming that the center node at the base of the weld is stationary. The simulation was displacement-controlled, and was ended when the maximum nodal stress exceeded the von Mises failure stress of cobalt.

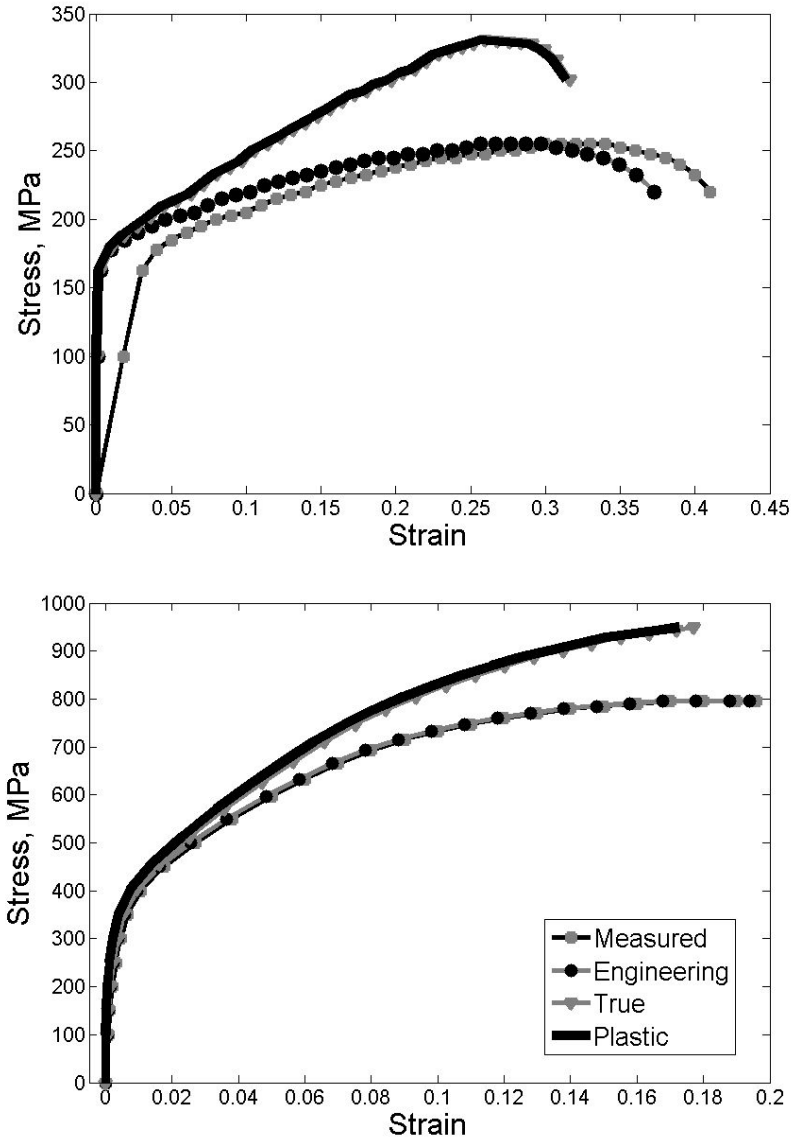

Figure 10: Calculated stress vs. strain

Raw data taken from literature [102,103] and subjected to equations 32,33. Deviations between engineering and measured stress-strain curves due to machine flexure; deviations between engineering and true stresses due to 'necking'. Plastic stress, used in the FEA models, is true stress minus elastic strain.

3.10.3 FEA of Sections Fractured from Completed Welds

Models of these fracture tests (Section 3.4.2-3.4.3) were created assuming a generic filler shape typical of all the Co-AgCu welds (Fig. 11). This allowed a small number of models to represent a much larger number of fracture tests. Shape parameters were determined by a combination of mechanical and optical measurements over the sample set being investigated. Measurements are accurate to 0.025 mm, but the variance across parts significantly exceeds that value. To estimate the predictive uncertainties, multiple models were produced per sample set, based on these measurements (Table 6). For bending tests, these models approximate the average, weakest, and strongest possible geometries. For the weakest FEA geometry, measurements providing maximum filler area and minimum base area were used. For the strongest geometry, measurements forming the smallest filler and largest base were used. The average model was constructed by simply averaging these measurements. For tension, only the average dimensions from the measured test pieces were used in the FEA models.

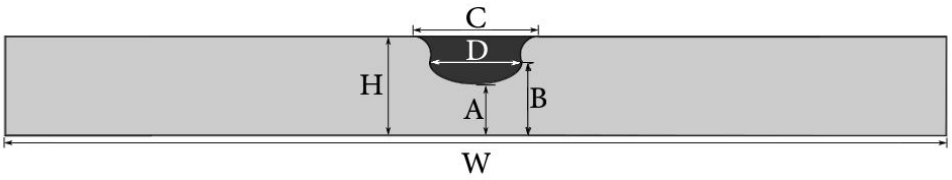

Figure 11: FEA filler shape
Basic shape used in most of the FEA. This corresponds roughly to the observed shapes of the weld sections. Table 6 provides parameter values.

These models share multiple similarities with the previous computations (Section 3.10.2). All of these FEA models utilize material properties for the base, filler and fixtures (Table 5) as previously discussed (Section 3.10.1). The contact formulation used in both model sets is identical; the contact between the sample and fixtures was

assumed to be frictionless, with the cobalt and filler being defined as the slave surfaces, and the steel fixture defined as the master surface. Like before, these models were displacement (not force) controlled, and used the standard, implicit problem solver.

Table 6: FEA geometry, ±0.005 mm

Finite Element Model	Width (W), mm	Height (H), mm	Thickness into page, mm	A, mm	B, mm	C, mm	D, mm
Tension, Average (Long Test Piece)	N/A	5.36	2.075	3.04	4.335	6.47	4.63
Tension, Average (Short Test Piece)	N/A	5.36	2.055	3.04	4.335	6.47	4.63
Root and Face Bending, Weakest	50.08	5.26	2.11	2.61	3.36	8.02	6.43
Root and Face Bending, Average	50.08	5.31	2.125	2.985	3.71	6.91	4.73
Root and Face Bending, Strongest	50.08	5.335	2.135	3.435	3.94	5.69	3.88
Root Bending and Crack Compliance, Weakest	50.08	5.32	2.465	2.465	3.63	8.28	5.58
Root Bending and Crack Compliance, Average	50.08	5.355	2.505	2.76	3.945	6.85	5.04
Root Bending and Crack Compliance, Strongest	50.08	5.385	2.525	3.075	4.36	5.74	3.94

3.10.3.1 Tension FEA

These models correspond to the tension tests done in Section 3.4.2. The two tension models were 3-dimensional, and utilized mirror symmetry across the weld (Fig. 7). Each of these models corresponds to the different types of tension test piece (Fig. 7A). Geometry for the fixture was measured via caliper, as were the width, height and depth of these test pieces (Table 6). Filler geometry was measured optically from approximately 30 mm and 45 mm from the weld start. All elements were hexagonal, corresponding to a seed size of between 0.1 mm and 0.125 mm (Table 7). In order to stabilize the FEA, a minimum of 250 steps were used in both calculations.

Table 7: Finite element parameters

Finite Element Model	Minimum Seed (mm)	Maximum Seed (mm)	Curvature Control	Max Step Deflection (mm)	Max Total Deflection (mm)	Dominant Element Type	Other Element Type
Tension, Average (long test piece)	0.1	0.125	0.2	0.005	1.25	Hex[a]	N/A
Tension, Average (short test piece)	0.1	0.125	0.2	0.005	1	Hex	N/A
Root and Face Bending, Weakest	0.1	0.1	0.1	0.001	7	Quad[b]	Tri[c]
Root and Face Bending, Average	0.1	0.1	0.1	0.001	7	Quad	Tri
Root and Face Bending, Strongest	0.1	0.1	0.1	0.001	8	Quad	Tri
Root Bending (residual stress study), Weakest	0.1	0.1	0.1	0.001	8	Quad	Tri
Root Bending (residual stress study), Average	0.1	0.1	0.1	0.001	8	Quad	Tri
Root Bending (residual stress study), Strongest	0.1	0.1	0.1	0.001	8	Quad	Tri
Crack Compliance, Weakest	0.1	0.1	0.1	N/A	N/A	Quad	Tri
Crack Compliance, Average	0.1	0.1	0.1	N/A	N/A	Quad	Tri
Crack Compliance, Strongest	0.1	0.1	0.1	N/A	N/A	Quad	Tri

[a]Hexahedral, [b]Quadrilateral, [c]Triangular

3.10.3.2 Face and Root 4-Point Bending FEA

These models correspond to some of the 4-point fracture tests done in Section 3.4.3. Models were 2-dimensional, and constructed of 5 parts consisting of a sample and 4 rollers. The face and root 4-point bending tests are identical, with the exception that the sample was flipped. Geometry of the rollers was measured via caliper, as were the height and depth of all of the samples. Width is approximate, and does not influence model behavior. The filler parameters were measured optically, from images occurring approximately 13 mm and 66 mm from the weld start. Final values were created from

the maximum, minimum and average dimensions from the three welds used in the corresponding study (Table 6). Basic finite element parameters are provided (Table 7).

3.10.3.3 Root 4-Point Bending (Residual Stress Study) FEA

These models correspond to the remainder of 4-point fracture tests done in Section 3.4.3. Models used for 4-point bending were 2-dimensional, and constructed of 5 parts consisting of a sample and 4 rollers. Geometry of the rollers was measured via caliper, as were the height and depth of all of the samples. Width is approximate, and does not influence model behavior. The filler parameters B and C were measured optically, while parameters A and D were measured via caliper from images occurring approximately 28 mm and 52 mm from the weld start. Final values were created from the maximum, minimum and average dimensions from the four welds used in the residual stress study (Table 6). Basic finite element parameters are provided (Table 7).

3.11 Crack Compliance Method

Residual stress measurements were successfully performed on sections from three separate welds utilizing the crack compliance, or slitting method. This method combines incremental strain measurements with analytic or finite element analysis assisted data reduction [104]. In this particular case, residual stress measurements were made by creating incremental cuts using a wire EDM, which were analyzed with FEA data reduction using Abaqus.

3.11.1 Strain Measurements

To perform the strain measurements, the welds were first cut into eight sections using an EDM (Fig. 8C). Half of these sections were heat-treated, half were not. Three of these sections were used for residual stress measurements, the others were fractured (Fig. 8C). This resulted in 12 total residual stress measurements. Of these 12 tests, only 5 were successful, mainly due to water impinging on the strain gauge.

For all of these tests, a strain gauge (Micro-Measurements EA-06-062AK-120) was mounted on the section, and protected via watertight acrylic coating. The sections were degreased with methyl-ethyl-ketone, before being cleaned with a mild phosphoric-acid compound (Conditioner A). This compound was then removed with an ammonia-based neutralizer (Neutralizer 5A). The glue used to affix the gauges was high purity cyanoacrylate (CN general purpose adhesive). The sections were then protected by a watertight acrylic coating (M-Coat D). Gauges were mounted on the back face of the section, in the exact center, on the cobalt base. This is similar to the typical setup used at Los Alamos [105], with the omission of a top gauge.

The sections were then loaded into a flushing type EDM. After the machine was automatically zeroed, a crack was extended from the filler to the base, using 20 increments of 0.25 mm each. Utilizing any more increments would jeopardize the strain gauge by potentially cutting the section in half.

The pressure of the jets, combined with the tight tolerances between the gauge size and part width, contributed to the destruction of the first 6 gauges. The next 6 gauges were run under minimal pressure; 1 additional gauge was lost due to poor section-gauge adhesion.

Residual stress measurements were taken after each increment. In order to account for EDM induced thermal expansion, measurements were taken after a time delay, or after observed temperature equilibration. The first 8 tests utilized a time delay; measurements were taken until no change was observed over a 2 minute period. This generally occurred after 6 or 8 minutes. The final four tests were temperature controlled via a mounted thermocouple. Measurements were taken between 23.4°C-23.6°C.

The procedure used during testing is very similar to the method in use at Los Alamos [105]. However, the procedure used here utilizes temperature control, has no top gauge, and omits all post-test optical measurements.

3.11.2 Data Reduction

Due to the complex shape of the Co-AgCu welds, it was necessary to analyze the strain data using FEA. Utilization of FEA for data reduction is typical for the crack compliance method [104]. FEA models for strain data reduction were created using the same shape parameters as earlier (Section 3.10.3, Table 6). Variance in calculated residual stresses due to these shape parameters is not significant, with the peak tensile stresses generally within ±5% of each other. This is a considerable under-representation of experimental uncertainties during strain measurement.

These models are 2-dimensional, and utilize weld symmetry for stress computation. Element size is restricted due to the requirement that crack width (induced by the EDM wire) be effectively filled. This results in a seed size of 0.1 mm (Table 7).

In order to reduce the strain data, the model is started in a stress free state. The crack is simulated through element removal. A sequential, unit traction is then applied to

every set of faces exposed through elemental removal. The change in displacement is then recorded over the elements representing the strain gauge contact area. This allows creation of a compliance matrix, relating relieved residual stresses and measured strains. By solving for residual stresses using this compliance matrix, the residual stress results were created.

3.12 Welding Voltage and Current Measurement

Welding currents and voltages were recorded using a standard digital camera (Fujifilm S700). However, the inconsistent brightness of the welding torch caused the ambient lighting to fluctuate significantly. Due to these variances, the resulting video data was not recoverable using commercial Optical Character Recognition (OCR) software.

In order to recover the data, the individual frames were digitally altered and enhanced using Imagemagick and MATLAB. Every individual frame was converted into six different images by varying thresholding parameters. Optical character recognition was then performed on these images using Tesseract OCR; results for every six image set were compared using MATLAB. This allowed determination of the character most likely responsible for a given image.

Chapter 4. Welding Results and Discussion

4.1 Welding Methodology and Parameters

Development of the Co-AgCu welding system involved not only system chemistry, but also determination of welding methodology and techniques. These techniques were simultaneously part of the methods used to produce the welds examined below and a critical result of this research. As such, a brief description of them is presented in the method section (Section 3.3).

4.1.1 Welding Parameter Determination

The techniques used in welding beryllium provided the basis for initial attempts at joining our surrogate. However, differences in the systems described in Chapter 1 required development of an entirely new welding system with specialized techniques. These techniques should be applicable to the original Beryllium welds, due to the physical similarities between these systems (Section 1.4).

Determination of weld parameters involved an extended multi-parameter study (Appendix I). Effects of welding method, top-gas, back-gas, amperage, pass number and position, and various clamping techniques were investigated. A majority of these welds were discarded after visual inspection due to incomplete melting. Weld quality of the remaining samples was evaluated with a combination of optical microscopy and 4-point bending. Since one of the goals of this study is residual stress analysis, our welds were evaluated based not only on their strength in 4-point bending, but also on the consistency of the individual samples. Thus, welding techniques that ensure full thickness melting

and crack mitigation were preferentially selected. This was not a straightforward procedure, as techniques which increase weld penetration generally result in more cracking.

Final welding parameters were evaluated through fracture, optical microscopy and SEM. Furthermore, FEA was performed to supplement these fracture results. These tests were performed on a complete weld, and on a series of incomplete welds after every pass.

Initial welding studies were performed using robotic or manual MIG. However, sufficient penetration was not possible using this method. Efforts to weld with an AlSi filler were also successful, due to the formation of brittle intermetallics. Switching to TIG with a silver-based filler resulted in increased penetration, as did changing our top gas from argon to helium. These efforts to increase penetration were complicated by the surrogate chemistry changing from CoMo with an AgMn filler, to Co with a AgCu filler (See section 1.4 for the rationale behind this chemistry).

Once the basic welding parameters (TIG, 225A, He top-gas) were determined, full penetration welding was possible. However, these welds were often inconsistent; displaying variable penetration and significant cracking. Further studies focused on increasing consistency more than increasing penetration. A special welding clamp (Section 3.3) was constructed in order to homogenize boundary conditions and the gap between parts. No effect of small gaps (<.65 mm) was observed. Argon back-gas was used to reduce oxidation, thereby reducing cracking. Welds were heated prior to welding to reduce internal stress; temperatures were monitored by thermocouple. A refractory backing was used to reduce thermal stresses. Finally, weld bead placement and pass direction were altered in order to reduce thermal stresses.

4.1.2 Final Welding Parameters

Our final manual tungsten inert gas (TIG) welding parameters used five passes with alternating directions. This unorthodox approach was adopted because welding in alternating directions produced more consistent weld pools, smaller transient areas at the beginning and end of these welds, and larger quasi-steady zones.

The power, location, and direction of these five passes was selected to increase penetration and reduce cracking. In particular, staggering the weld passes (Fig. 2) was designed to cracking by reducing reduce residual stresses. The 5-pass configuration was selected because this was the maximum number of passes which could be consistently produced.

The first four passes were done at 225 A, with 0.43 liter/s He top-gas and 0.25 liter/s Ar back-gas, while the final pass was done at 150 A with 0.25 liter/s Ar top-gas and back-gas. The weldments were allowed to cool to room temperature between passes for all but the first two.

The first pass is done with very little filler, allowing maximum penetration. The second pass was performed immediately afterwards in the opposite direction, in order to further penetrate the base and homogenize the thermal fields. Since both the first and second passes heat the weld root, producing them sequentially allows increased temperatures at lower welding power. The third and fourth passes are designed to penetrate the sides of the weld groove without causing excessive filler addition or melting. Excessive filler melting causes cracking and distortion due to base-filler CTE mismatch. The final, fifth pass is designed to homogenize the weld face, at the lowest possible temperature.

In order to homogenize thermal and mechanical boundary conditions, these welds were all produced utilizing a purpose built clamp (Section 3.3). This clamp featured a porous refractory base, which allowed Ar back-gas, while simultaneously thermally insulating the weld root. Ar back-gas was used in order to reduce root oxidation and potentially cracking. Insulating the weld root reduces cracking by reducing thermal gradients and reducing necessary power.

This clamp was heated prior to welding inside a muffle furnace to above 300°C, then air-cooled to 250°C before the part was loaded. Welding occurred at a substrate temperature of approximately 230°C, which was monitored by a thermocouple. Preheating a weld often improves weld quality, as the internal temperature fields are less severe. Furnace heating, rather than torch heating, the clamp significantly improved weld consistency. However all of the high-quality partially completed welds were produced prior to this discovery. These welds were instead produced on a clamp preheated by torch or previous welds.

These parameters are significantly different than those used to produce Be-AlSi welds at Los Alamos National Laboratory (LANL). Those welds are three-pass metal inert gas (MIG), robotically welded in an Ar-He environment. The base is S200D grade beryllium, formed into two 165.1 mm diameter rings, 6.35 mm thick, 25.4 mm high with a 3.18 mm J groove (Fig. 12) [31]. Our surrogate welding parameters are compared with the LANL Be parameters in Table 8 [31,106]. More significant than these geometrical differences was our substitution of TIG for the MIG welding used on beryllium (Table 8). By replacing MIG with TIG it became possible to form coherent welds, due to the greater amount of energy TIG imparts to the weld base.

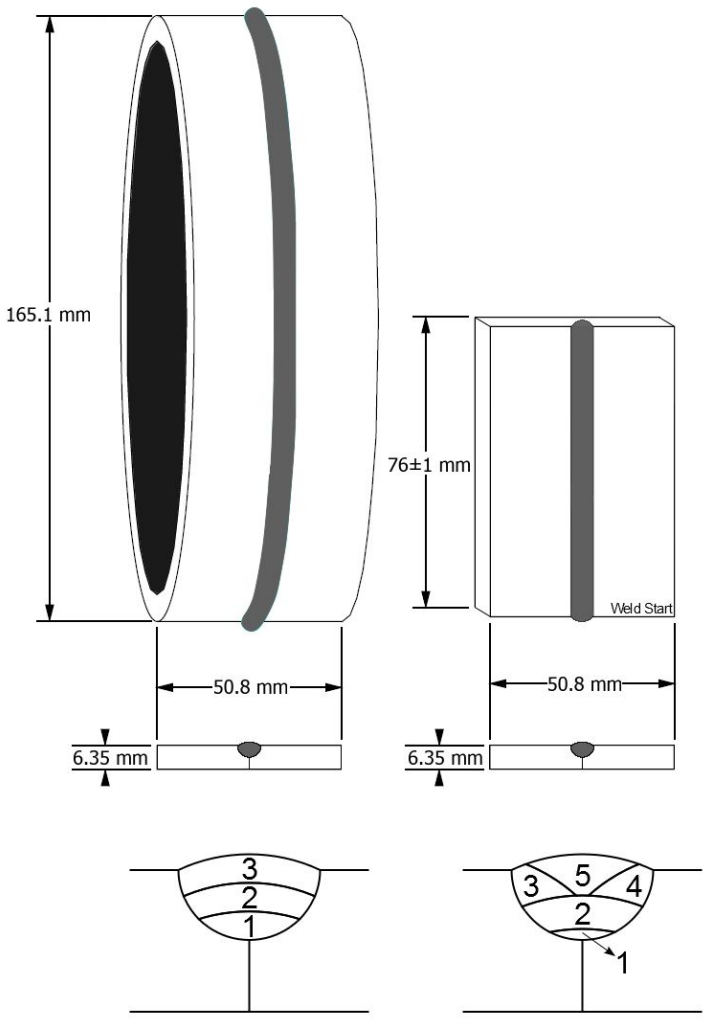

Figure 12: Comparison of weld geometries

Left: PIGMA welded Be-AlSi weldment.
Right: TIG welded Co-AgCu Weldment. Schematic shows weldment geometry and approximate pass locations for both the Be-AlSi and the Co-AgCu weldments. Dimensions are all ±.08 mm unless noted otherwise. Image of Be ring modified from [31].

Table 8: Welding parameter comparison

Welding Parameters	Be-AlSi	Co-AgCu
Base Metal Crystal Structure	HCP	HCP
Filler Metal Crystal Structure	FCC-Diamond	FCC
Immiscible Constituents	Yes	Yes
Welding Method	3 pass MIG	5 pass TIG
Geometry	Cylindrical Double J groove	0.25”X1”X3” plate Double J groove
Shielding Gas	0.39 Helium-.07 Argon	0.43 Helium topgas, 0.25 Argon back-gas
Maximum Amperage (A)	150	225[a]

[a] Foot pedal controlled
[b] Maximum voltage, (Maximum start voltage)

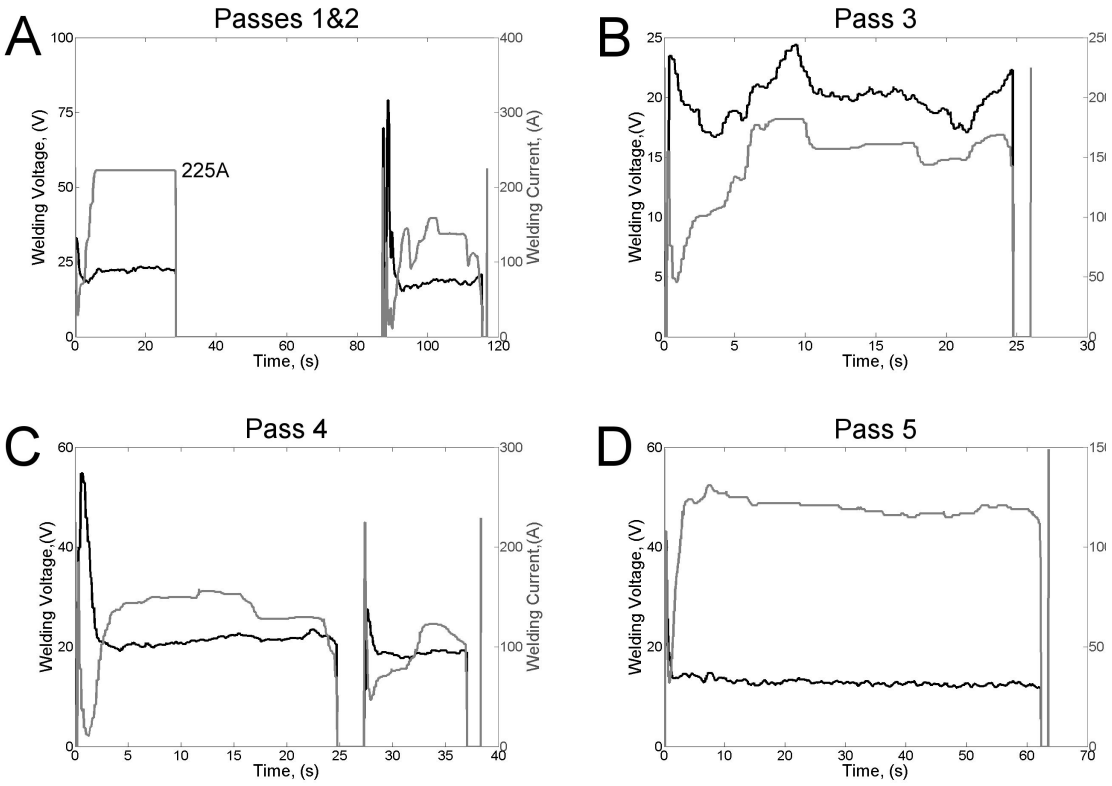

Figure 13: Welding voltages and currents

Figure shows voltages (black) and currents (gray) recorded during welding. Voltage spikes generally indicate poor contact, and often precede or follow establishment of the arc. Passes 1 and 2 were performed together, all other passes were performed after a lengthy delay.

A. Pass 1 (left) was performed at the maximum amperage for all but the first few seconds. Approximately 60 seconds after pass 1 was completed, pass 2 (right) was performed at a lower amperage.

B. Pass 3 was performed after a long delay. Like passes 2 and 3, amperage and voltage are variable for the first several seconds. After about 7 seconds, these values equilibrate.

C. Pass 4 was interrupted after ~25 seconds, and restarted ~3 seconds later. Although not typical, several welds have a similar interruption

D. Pass 5 is performed at a lower maximum amperage (150A) then the others, in order to finalize the weld. Currents and voltages for this pass are usually more consistent than the other passes.

Producing these welds by hand implies that the currents used in these experiments do not provide an accurate measure of the energy imparted to the weld. Since the welder controls the power of the torch, these tabular values correspond to the maximum current available. This is only achieved when the foot-pedal is fully depressed. Repeated trials resulted in our selection of a 225A limit. However, subsequent voltage and current

measurements (Fig. 13) indicate that 225A is not sufficient. This is evidenced by the welder operating at the 225A limit for the duration of Pass 1 (Fig. 13A).

Hand welding introduces additional uncertainties as well, since the torch position, feed rate, and traverse speed are not precisely controlled. This is beneficial in the prototyping phase, allowing a human welder much greater flexibility than a machine. Unfortunately, this complicates analysis since the welds are less consistent. Further study has concentrated on thermal profiles and power usage; information necessary for automation. Our techniques have proven consistent enough for us to generate 14 complete 5-pass welds, and an additional 4 incomplete welds for further study.

4.2 Welding Results at Differing Welds Stages

Weld quality was evaluated using a combination of 4-point bending, microscopy, and FEA. These evaluations were performed on a complete 5 pass weld, and a series of incomplete welds, halted after passes 1, 2, 3 and 4. This allows investigation into the quality of the individual passes. A 4-point bending apparatus was used to evaluate weld quality, since it produces failure which would be most augmented by CTE (coefficient of thermal expansion) mismatch. Optical microscopy allows analysis of grain structure, cracking and overall quality, while SEM shows the fine structure and material composition. Finite element analysis allows interpretation of fracture results.

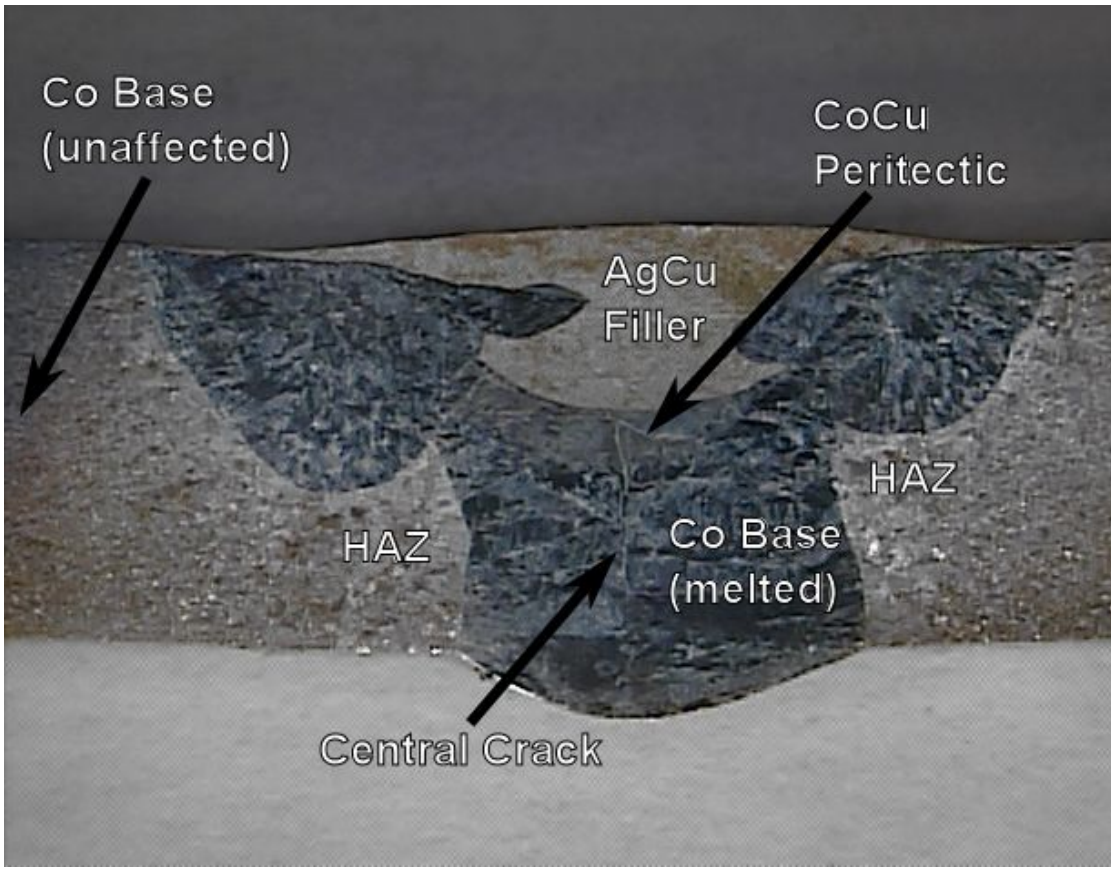

Figure 14: Weld regions

Micrograph of a completed weld shows the 5 basic weld regions, and the central crack. The central crack is caused by grain convergence near the weld centerline. The 5 regions define the shape and chemistry of all the complete Co-AgCu welds. (1) The unaffected Co base, located away from the weld is composed of small equiaxed Co grains (Fig. 15A). (2) The HAZ, located on either side of the fusion zone, is characterized by grain growth. (3) The melted Co base is composed of larger, directional Co grains, and AgCu backfilled cracks. (4) The AgCu filler has a eutectic structure (Fig. 15B). (5) The CoCu peritectic, located between the AgCu filler and Co base, is characterized by cellular and lamellar Cu exsolution structures (Figs. 15C,D,E)

4.2.1 Microscopy at Differing Weld Stages:

Optical images were taken with direct (Fig. 9, middle column) and indirect light (Fig. 9, left column), the latter using digital color inversion. These images show a high variability in the size of the melted cobalt regions, as well as a sizable reduction in the size of the filler region when compared to the machined shape (cf. Figs. 6, 9). This change is due to melted cobalt flowing towards the weld base, and to AgCu going into

solution with the cobalt. The variability in shape of the melted zone illustrates the inherent uncertainty of hand-made welds. Furthermore, this uncertainty is such that the effect of the second pass on final weld geometry is not possible to determine; although its impact must be slight (Figs. 9 D,E,F). The primary effect of the second pass is to increase the amount of AgCu filler (Figs. 9 D,E,F). The third and fourth passes melt only a semicircular area on the side of the weld (Figs. 9 G,H,J,K). Of note are the elongated (columnar) grains with the long axis pointing toward the center, which are most clear in the image of Pass 1 (Fig. 9B) and Pass 5 (Fig. 9M), although it is present in all passes. This is significant because the center line into which grains converge facilitates cracking in the weld center (Figs. 14, 15F), since impurities segregate here. The fifth pass is produced with a lower temperature arc, with the intention of filling any low areas left after the fourth pass. The markedly different shape of the fifth pass is likely due to the weld experiencing very hot third and fourth passes as evidenced by the large melted regions.

The micrographs show that the completed weldments contain 5 distinct regions (Fig. 14). The unaffected cobalt is characterized by the small grain size (≈20μm) produced by rolling (Figs. 14, 15A) and is located away from the weld. The heat-affected zone (HAZ) (Fig. 14) is visible after all passes on both sides of the weld (Fig. 9), although its extent can only be determined by comparing both the images produced with direct (Fig. 9 middle column) and indirect light (Fig. 9 left column). This region exhibits grain growth. The melted Co base is characterized by larger grained cobalt (≈500 μm), coupled with backfilled silver-copper cracks (Figs. 14, 15F). At the top is the AgCu eutectic, which is occasionally invaded by cobalt nodules (Figs. 14, 15B, 16A).

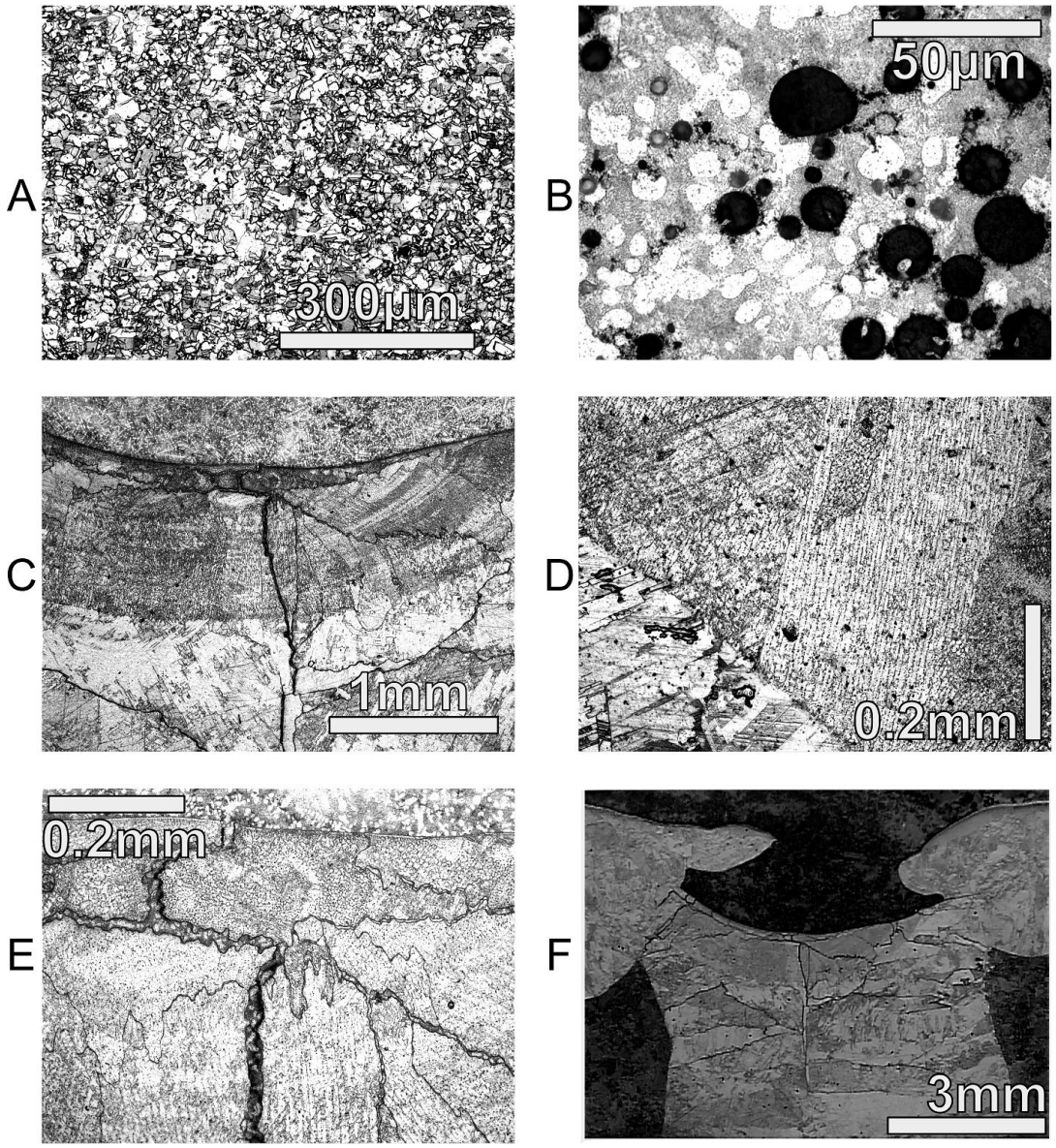

Figure 15: Optical micrographs

Taken from pass 5, unless noted otherwise. **A:** Base grain structure of pure cobalt, far from the weld. Note the small, consistent grain size, produced by the rolling the Co base. **B:** Image inside the filler showing the AgCu eutectic (white and tan). The dark areas are cobalt grains, which has been verified by SEM (Fig. 16). From a prior 5 pass weld. **C:** The AgCu filler (top) is bounded by an arcuate region below it, also visible in Fig. 9, rows 3-5. This region is thought to contain significant amounts of copper. Below this region is the cobalt base consisting of hcp grains meeting at a central crack. **D:** A magnified image showing the probable intersection of the Co base, and a CoCu mixture. Filler is up, and offscreen. The cellular structure is thought to be produced by Cu exsolving from the Cobalt base. **E:** A magnified image showing the intersection of the AgCu filler, and the CoCu mixture. The AgCu dentrites are located at the top. Below this is another, finer, dendritic structure, thought to be caused by copper exsolution. Several backfilled cracks are present in the middle of the image. Some of the small dots in this image seem to be silver, isolated inside the cobalt base. **F:** Cracks enhanced optically. The network of backfilled cracks originates at the filler, and grows outward from a predominant, central crack. This behavior has been observed in all welds, and is one of the primary factors affecting weld strength. Also note the small crack, running directly under the filler. This crack is due to CTE mismatch, and has also been repeatedly observed.

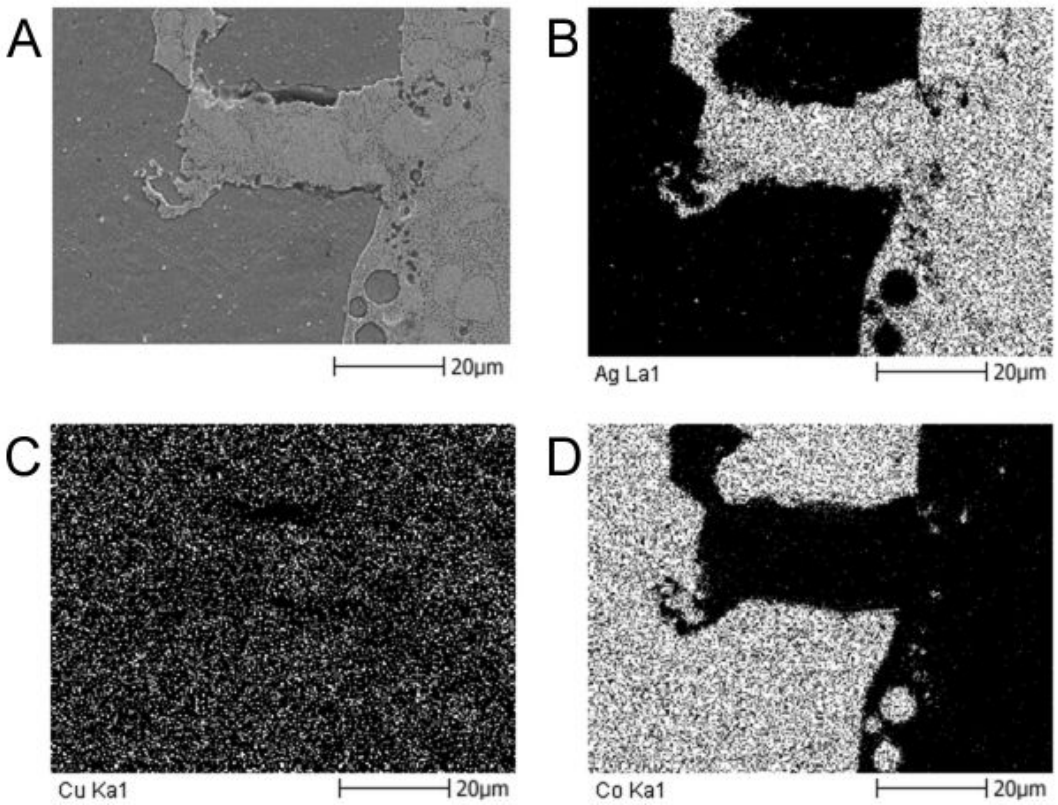

Figure 16: SEM backscatter and EDX images of the weld-filler interface

Images taken on the 5 pass weld after chemical etching. **A:** SEM backscatter shows the intersection between the cobalt (dark gray) and the silver copper (light gray and dendritic). Note the presence of cobalt inside the filler (dark, circular grains), and small concentrations of silver inside the cobalt base (white spots). The extremely dark areas along the interface are voids. These voids were probably caused by hot shortness, and may have been augmented by the chemical etch. **B:** Silver (Ag) EDX scan shows the lack of mixing between the silver in the filler (right) and the cobalt base (left). **C:** EDX scan for copper shows a nearly universal distribution of copper, indicating that cobalt and copper went into solution with the cobalt during welding. There appears to be a slightly higher concentration of copper inside the globular grains in the filler, indicating that the fine, dendritic area is the eutectic, and that the filler in this image is copper rich. **D:** Cobalt EDX scan shows the lack of mixing between the cobalt and silver constituents. Confirms that the inclusions in the filler are cobalt.

4.2.2 Fracture Testing and FEA at Differing Weld Stages

Finite Element Analysis (Section 3.10) was used to evaluate our Co-AgCu welds during fracture (Section 3.4). The experimentally obtained (after stiffness correction) von Mises stress at failure of cobalt was approximately 950 MPa. Finite element modeling shows the influence of stress concentrations (Fig. 17) on fracture location. Higher numbers of passes resulted in predicted fractures on either side of the weld root,

whereas fewer passes produced failure at the top of the weld. The failure initiation regions are marked by arrows (Fig. 17). However, experiments show that failure is generally observed in the center of the weld, due to local cracks produced by the convergence of grain boundaries.

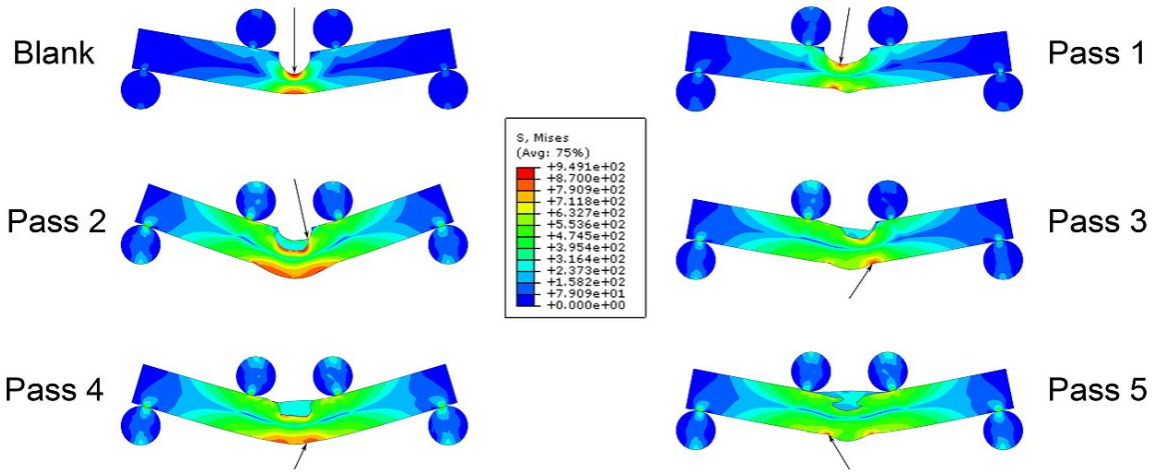

Figure 17: von Mises stresses at failure
Images show predicted stress field at minimum displacement sufficient to cause material failure according to the von Mises yield criterion. (von Mises failure stress is assumed 949.08 MPa). The location of the peak stress is designated by the arrow. Note how the location at failure changes from the top of the sample, for low numbers of passes, to the bottom of the sample, on one side of the weld pool. This observation is crucial, as weld failures have been observed both here, and the center of the weld. This indicates that these welds have been weakened by cracking; but that this is highly mitigated since the cracks are not in the regions of highest stress. Also note the large stressed areas in pass 1 and pass 3, indicating that the stress concentrations for these samples is lower.

Four-point root bending, as described in Section 3.4.1, was performed on the outside 5 pieces for the intermediate and final stages of the weld (Fig. 3A). The resulting plots (Fig. 18) are normalized to the width of the sections, and compared to crosshead displacement of the tensile tester. This was done to eliminate any effects caused by inexact sectioning. The most important trends in these plots are the general increase in strength with the number of passes. The increased strength is expected and is caused by the addition of material to the welds.

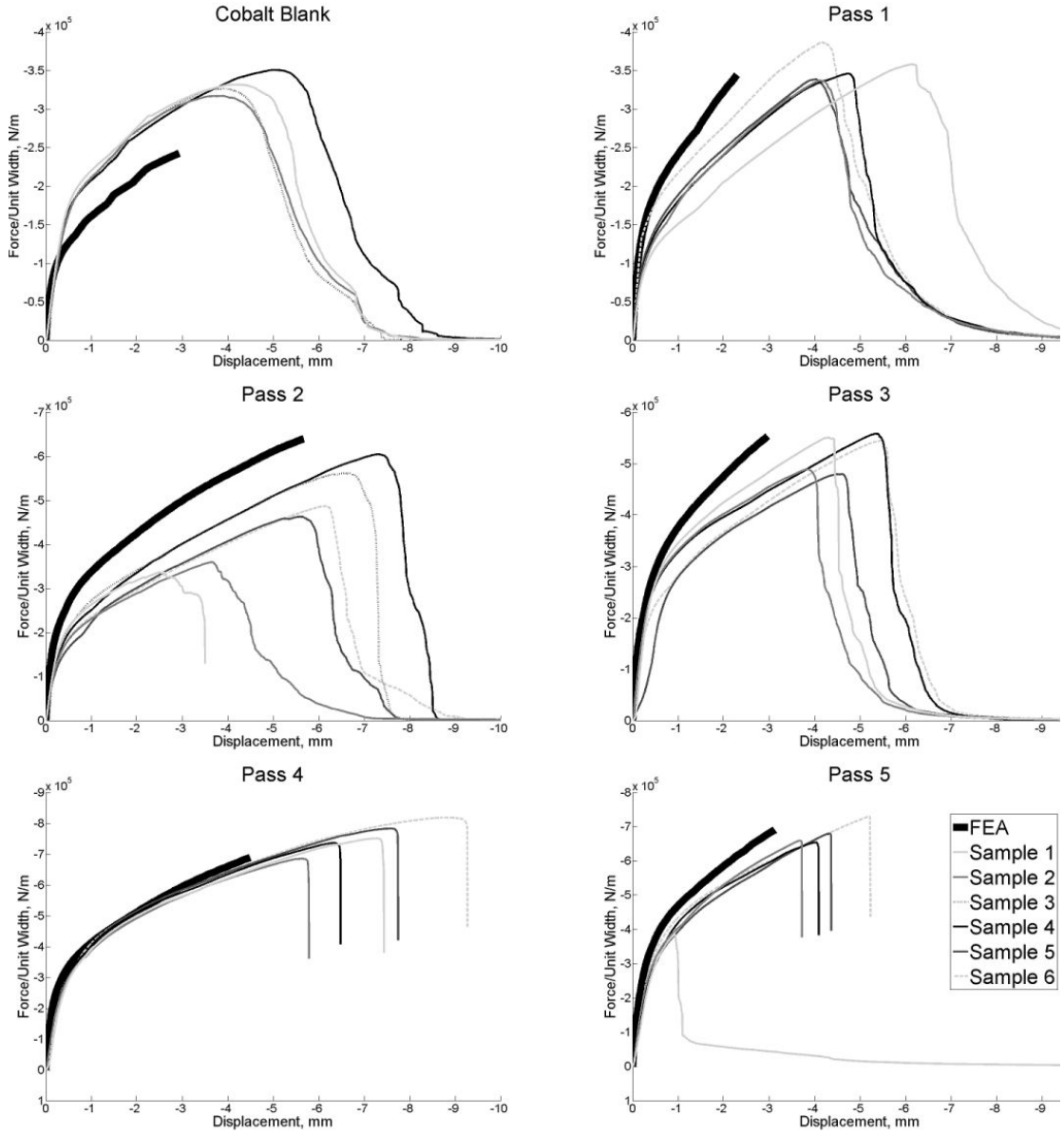

Figure 18: Applied load vs. displacement curves for fracture specimens and FEA models
The load is normalized by the sample width, or for the FEA curves, the section width. The displacement is measured at the tensile tester's screw, and modeled as the displacement of the top rollers. Note the average increase in failure moment at the number of passes increases. Also note the increased severity of failure as the number of passes increases. This is most noticeable in pass 4 and pass 5, where the machine truncated the test due to the abrupt change in load. The overestimation of load by FEA is thought to be mostly caused by dissimilarities between the theoretical and actual materials, although slip and flex of the tensile tester could contribute. The opposite behavior of the cobalt blank is due to the material composing the blanks not being softened by the welding process. The underestimation of displacement at failure may be caused by the truncation of the simulation before total failure and by the slip of the tester.

All sections fail at a higher displacement than predicted by FEA (Fig. 18) and all welds (Fig. 18, Pass 1-5) exhibit lower than predicted Force vs. Displacement curves. These effects may have a number of physical causes, such as presence of Ag cracks in the cobalt base, large grain sizes, or slip and deflection of the tensile tester itself. The simulation, which truncates due to predicted local failure, may also contribute to this effect by ending prematurely. The higher than predicted Force vs. Displacement curves of the cobalt blanks are probably due to their finer grain size.

Further analysis of these welds involved determination of the quasi-steady region of the samples. This was done by comparing the initial stiffness and maximum applied loads and deflections. Determination of the stiffness involved finding highest slope in the Load vs. Deflection graph. This was done in order to avoid the "ramping up" often seen in tensile testers. The stiffness increases with the number of passes, and is roughly constant in all weld stages (Fig. 19).

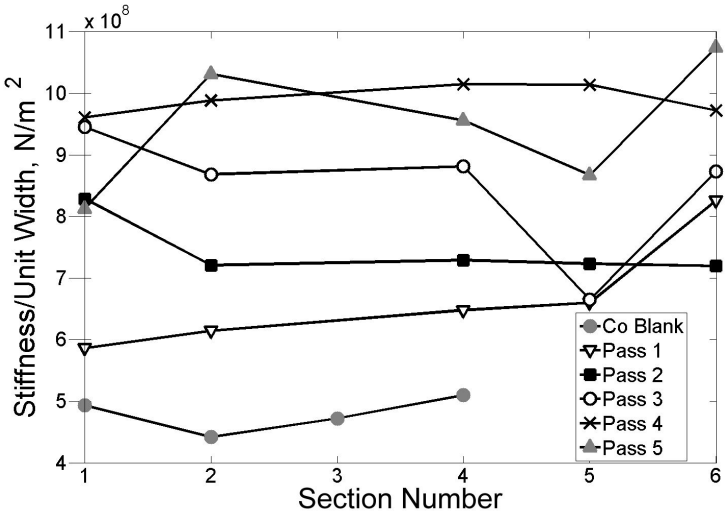

Figure 19: Section stiffness

For the different passes, the section number corresponds to a change in section position of .2 inches. The cobalt blank sample numbers do not share this relationship. The stiffness is mainly a function of specimen shape and material composition. A weld's quasi-steady zone should have relatively constant stiffness. The area of greatest consistency in these welds is from sections 2-4. The higher stiffness at the beginning and end of these welds is due to the larger weld pools there.

Section stiffness is useful for determining the quasi-steady state region of these welds, as it is heavily dependent on macro geometry. Although effects such as residual stresses or cracking may play a prominent role in weld failure, the purely elastic response will largely ignore them. Thus, these stiffness plots indicate whether the geometry is fairly consistent inside the welds; one of the features of the quasi-steady state region.

Interestingly, the weld with 5 passes has a less consistent, and often lower stiffness then the weld with 4 passes. This may be due to the presence of backfilled cracks, or geometric differences due to the tapering weld root (Fig. 5). In either case, the AgCu overfill (Fig. 9, M,N,O) seems to not significantly stiffen the weldment.

Section 1 (Fig. 4) often has a higher stiffness than the other sections. This is probably due to the first section being on the edge of the initial weld pool. What follows is a 20 mm long area of fairly consistent geometry, for all but the 3-pass weld. It is likely the variations seen in the 3-pass weld are augmented by its asymmetric section (Fig. 9 G,H,I). The final section position indicates an increase in stiffness for three of the welds; which may be an effect of the weld pool at the back of the weld.

The conclusion that sections 1 and 6 are outside the quasi-steady state region is supported by both the Load vs. Section Position and Displacement vs. Section Position plots (Fig. 20). These plots show a large degree of inconsistency for section 1. This inconsistency is probably caused by the initial weld pool changing the geometry and potentially initializing cracks. Section 6 is also arguably outside of the quasi-steady state region, as it always fails at a higher moment and higher displacement then the other sections in this series. Further analysis of this data shows a general increase in strength with position (Fig. 21), as well as a linear relationship between moments and

displacements at failure (Figs. 21, 22). The range of measured values, indicated by the error bars (Fig. 21), gives a rough estimate of the variance at each position; the low quality of position one is evidenced by both the high variance in position, and low moment. The high deviations in deflection and load for sections 1 and 6 indicate that these positions are not in the quasi-steady region.

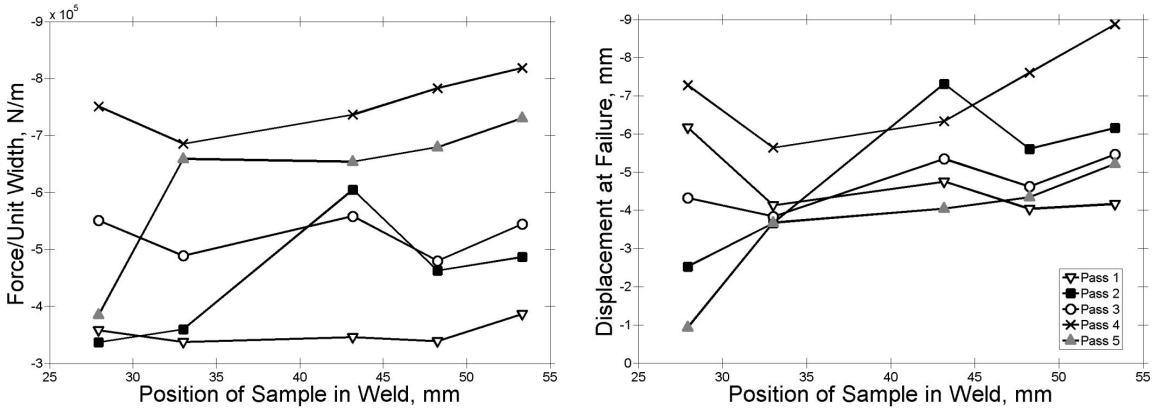

Figure 20: Applied loads and deflections at failure

Left: Applied load at failure vs. sample position**.** Note the wide disparity of behaviors for the first sample position. From this point onward, the load is still somewhat random, but all welds show an increase in load for the final position.

Right: Deflections at failure vs. sample position. Note again the high degree of variation, followed by a more consistent region. Like the above graph of failure loads, all samples show a higher displacement at the final position. This indicates the material here is both stronger and more ductile.

Determination of the quasi-steady region is both subjective and non-trivial. Furthermore, the location of this region varies slightly for different welds. This region is defined as extending from 30-50 mm, because this area shows a higher degree of consistency (Figs. 19, 20) then the surrounding regions, although the different individual welds do exhibit smaller random changes in maximum moment, displacement, and stiffness here. For the purposes of this study, section 6, but not section 1 was included in the region of analysis. Section 1 was too inconsistent to provide useful insight into weld

behavior (Figs. 19-21); while section 6, arguably outside of the quasi-steady state region, still provides consistent data.

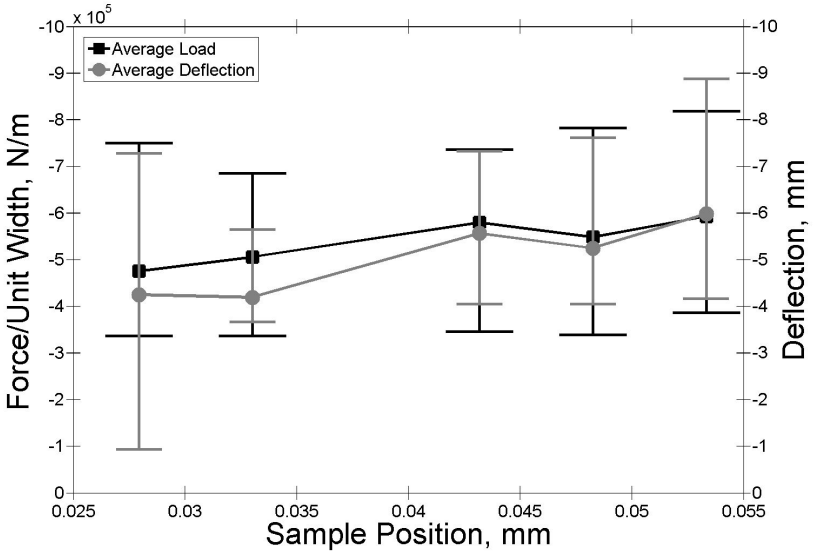

Figure 21: Failure loads and deflections by sample position

The error bars indicate the range of recorded values. Several trends are visible, the most striking being the relationship between failure deflections and applied loads. The large deviations at the first sample position indicate that the quasi-steady region does not extend this far for all welds. The increase of weld strength with position, as well as the increased uncertainties at the final position suggests a small quasi-steady state region, potentially only including the samples located between 30.5 mm and 50.8 mm.

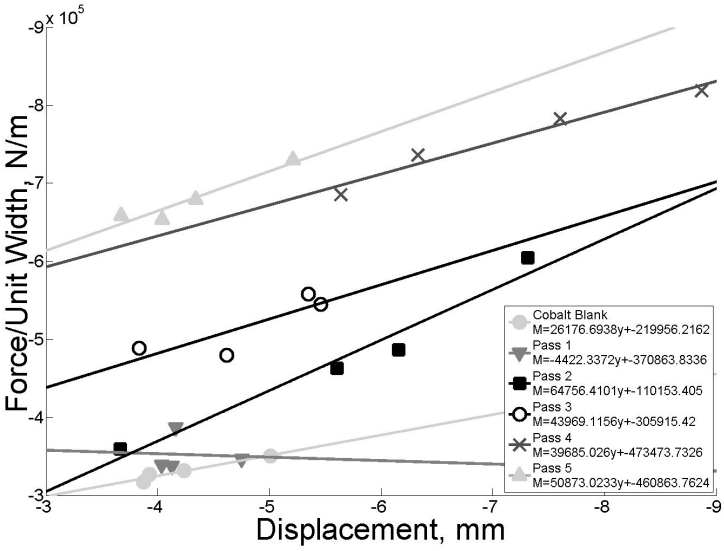

Figure 22: Failure loads vs. displacements arranged by weld

Note the clear linear relationship, showing that the most ductile specimens are also the strongest. This is an indication of the effects of random cracking across different samples for the same weld. The most significant outlier is weld pass 1, position 6, which may be an indication that the geometry here is noticeably different to the other samples; an assertion supported by its high stiffness (Fig. 19).

Removing section 1 from the data pool allows investigation into the average behavior of each weld (Fig. 23), with the error bars indicating the ranges of used values. Superimposed on this is the FEA predicted load to failure. As is expected, the increasing number of passes generally results in a stronger weld (Fig. 23, top), but, surprisingly, has little impact on displacements to failure (Fig. 23, bottom). The performance of the cobalt blank in both graphs deviates considerably from predicted; which is expected due to its much smaller grain size reducing its ductility. The differences in displacements by weld is mostly determined by nuances in weld geometry causing stress concentrations, as FEA predictions mirror data (Fig. 23, bottom). The poor performance of the two-pass weld (Weld 2) may be a random result of a poor weld, as the best section from this weld seems to correlate best with the finite element model.

Investigation into the relationship between moments and displacements inside these welds shows a linear correlation (Figs. 21, 22). Deviations in geometry (Fig. 5) are thought to be significant, and may influence this behavior. Changes in the amount of backfilled or empty cracks will also cause such behavior. Alteration of material properties, however, cannot account for observed behavior, since this would cause increased strength but decreased strain.

The displacement at failure is dependent mainly on the section geometry and on the weld quality. The influence of section geometry is shown by the correlation of FEA and fracture data. The influence of weld quality is more difficult to define, since the models do not correlate with differing geometries across sections. If the averages (Fig. 23) are considered, the average loads at failure for both the two and four pass welds are different than predicted. This deviation is probably caused by the two pass weld being lower than

average quality, and the four pass weld being of excellent quality. The stiffness plot (Fig. 19) supports this by showing approximately constant behavior over each weld; implying that most of the variation for a single weld (Fig. 22) is due to weld quality. This is especially significant for pass 2; it has a very linear stiffness relationship when section 1 is removed, but huge uncertainties (Figs. 22, 23).

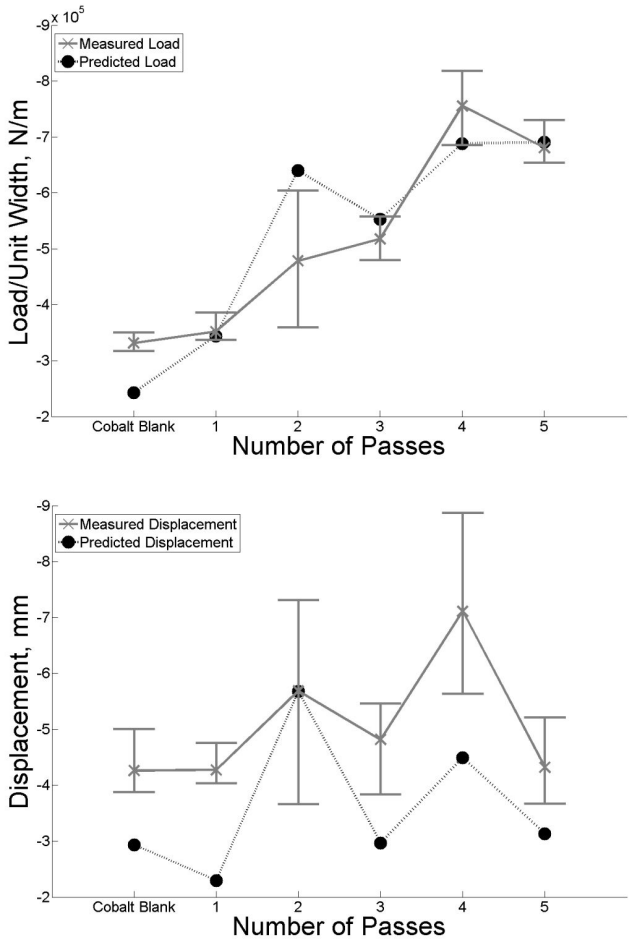

Figure 23: Average failure loads and deflections

Top Average loads at failure, vs. number of passes. The blue line shows measured values, while the dotted red line indicates values predicted by FEA. The error bars indicated the maximum and minimum values measured. The main trend is the increase in strength with the number of passes. This is caused by the addition of material to the weldment. The deviation between measured and predicted values for the cobalt blank was caused by the material not being annealed.

Bottom Average deflections at failure vs. number of passes. The blue line shows measured values, while the dotted red line indicates values predicted by FEA. The difference between predicted and measured values may be due to measurement errors caused by apparatus slip and flex. The high variation at pass 2 is probably caused by influence of cracking.

Although weld quality can have a large impact on strength and deflection, the quality was similar for all welds, which allows for reasonable correlation with FEA results. The effects of cracking are also ameliorated by the maximum stresses occurring away from the central, cracked region.

4.3 Welding Results For Completed Welds

4.3.1 Spatially Resolved Acoustic Spectroscopy, Optical Microscopy, and Electron Microprobe on Unfractured, Completed Weldments

As discussed earler (Section 4.2.1) Co-AgCu welds possess five distinct regions: the eutectic AgCu filler, the peritectic CoCu region, the melted cobalt base, the heat affected zone (HAZ), and the unmelted base (Fig. 24A). SRAS, WDS and microscopy provide a better understanding of the microstructure and origin of these zones.

The peritetic zone was originally distinguished by the presence of small (~10μm) aligned lamellar and cellular structures, believed to be the result of Cu exsolution during cooling. Exsolution is a process by which a solid solution phase unmixes into two separate phases in the solid state. These structures exist inside larger macrozones (~500μm), which are believed to be remnant Co grains, before Cu exsolution.

The presence of Cu has been confirmed by WDS, with significantly higher concentrations of Cu existing in the peritectic region, which encompasses WDS measurements on spots 1-9 (Figs. 24, 25). Optical microscopy shows two different structures inside the CoCu macrozones; close (~ 200μm) to the filler these structures appear cellular, while farther away (~ 200-1000μm) they are lamellar (Figs. 15E, 24). Although significant variations in Cu and Ag content occur inside the peritectic region

(Fig. 25), these chemical variations are not well correlated with observed structural differences; the area of highest Cu and Ag content extends into the lamellar region (Figs. 24, 25). Therefore, these structural variations are probably thermally induced.

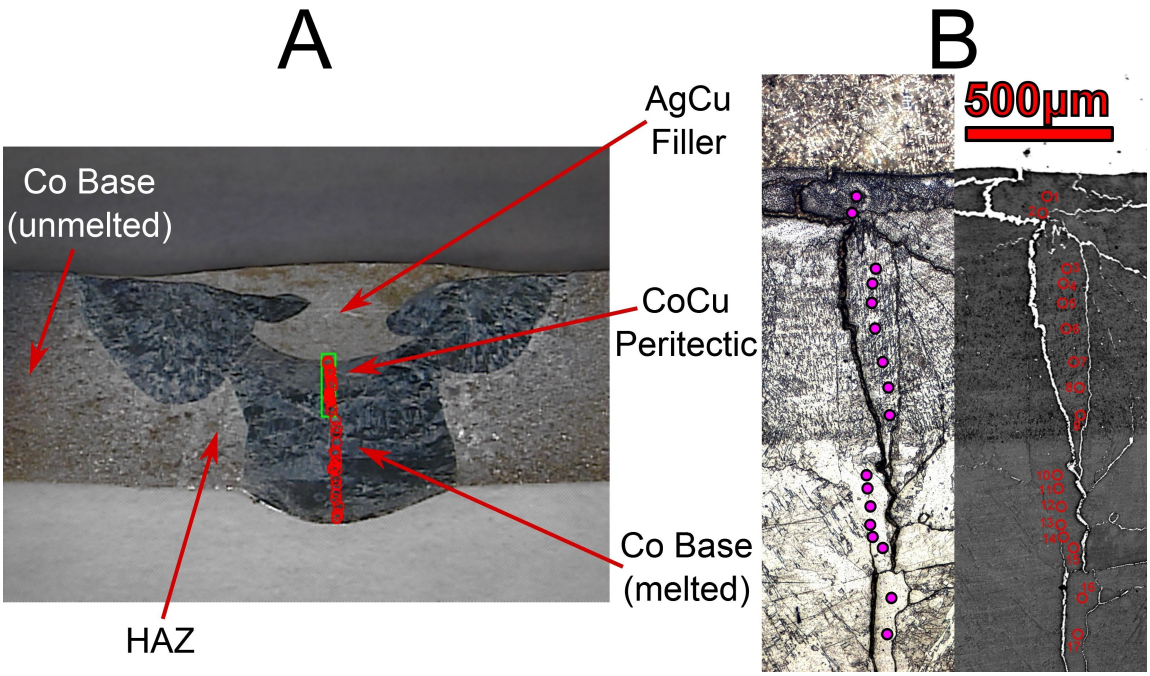

Figure 24: Weld macrostructure, microstructure, and WDS sample locations

A: Optical micrograph of an etched weld section, showing the different weld regions, as well as the location of the microprobe samples (red circles) and the magnified area to the right (green box). The unmelted Co base is characterized by small grain size due to rolling. The boundary between it and the heat affected zone (HAZ) is not clearly defined, but grain growth is evident. Melting of the Co base has resulted in much larger, aligned grains. The AgCu filler is a lighter colored structure located at the top of the weld. The CoCu peritectic is a small, gray, arcuate region located below the filler.

B: Optical micrograph and electron backscatter image showing the AgCu filler (top), the CoCu peritectic (middle) and the Co base (bottom). Location of these images in the weldment is given by the green box in the micrograph to the left. Note the location of the WDS samples, given by green or red dots. The AgCu filler posses a eutectic structure, visible in the optical image. The peritectic is filled with fine, Cu structures, visible in both images. Note how the cracks have been backfilled by AgCu, causing them to appear white in the backscatter image.

SRAS also indicates that this CoCu region has a markedly different grain structure than the cobalt base. The observed macrozones in the peritectic region are generally larger than the grains in the base cobalt region, contain numerous microscopic cracks, and have a wider range of velocities (Fig. 26). Multiple regions with fast/fast (bright blue)

and ‘slow/slow’ (pale green and salmon colors) velocity combinations exist inside the peritectic, but are absent or highly limited in the Co base.

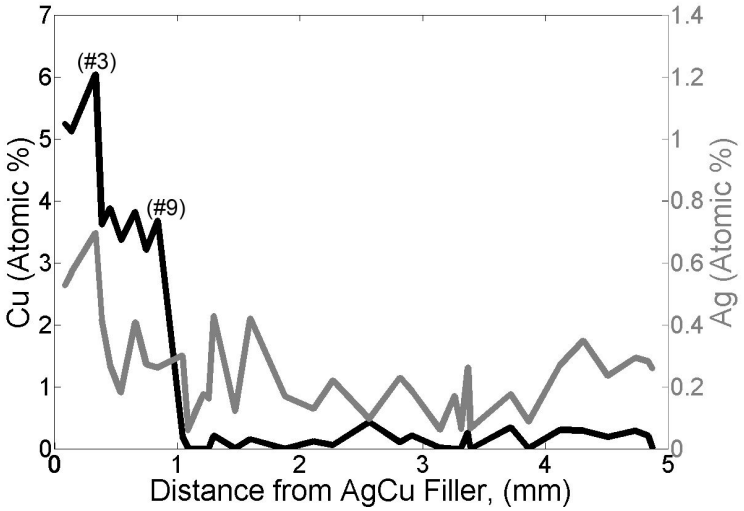

Figure 25: Weld composition vs. distance from AgCu filler

Weld composition was measured using WDS, from near the base-filler interface, to the weld root. Locations of the individual sample points are shown in Fig. 24. Note the high Cu concentrations (samples 1-9) existing inside the peritectic region. Also note the notable drop in both Ag and Cu concentrations which happens after sample 3. Outside of the peritectic, Cu concentrations are very low, while Ag concentrations are more uniform throughout the weldment.

The presence of slow/slow macrozones in the peritectic is compelling, since HCP crystal structures cannot produce this velocity combination as two orthogonal measurements cannot both be on the slow axis of the crystal. Furthermore, the presence of numerous ‘fast/fast’ grains indicates that the observed velocity profiles cannot result exclusively from an overall wave speed reduction.

Texturing in the peritectic region (Figs. 14, 15C, 15D, 24), which was attributed to Cu exsolution during cooling, may help explain differences in observed wave velocity. These Cu exsolution structures are too small for SRAS detection, but maintain original grain orientation, resulting in large apparent grain size. Effects of the Cu lamella are probably a function of their orientation, complicating analysis. Furthermore, optical images taken during SRAS show this region contains numerous microscopic cracks (Figs.

15F, 26), which may also have an effect on the measured velocities. Persistent FCC Co macrozones could explain the simultaneous presence of slow/slow and fast/fast regions, although neither FCC Co, nor FCC CoCu are stable at room temperature [67]. Finally, differences in wave velocities between the peritectic and base regions may partially result from slower wave speeds in the base. The cobalt base has been subjected to multiple heat treatments below the melting point, resulting in grain fining and jagged grain boundaries (Figs. 15, 24), as well as probable small regions FCC and possible stacking faults.

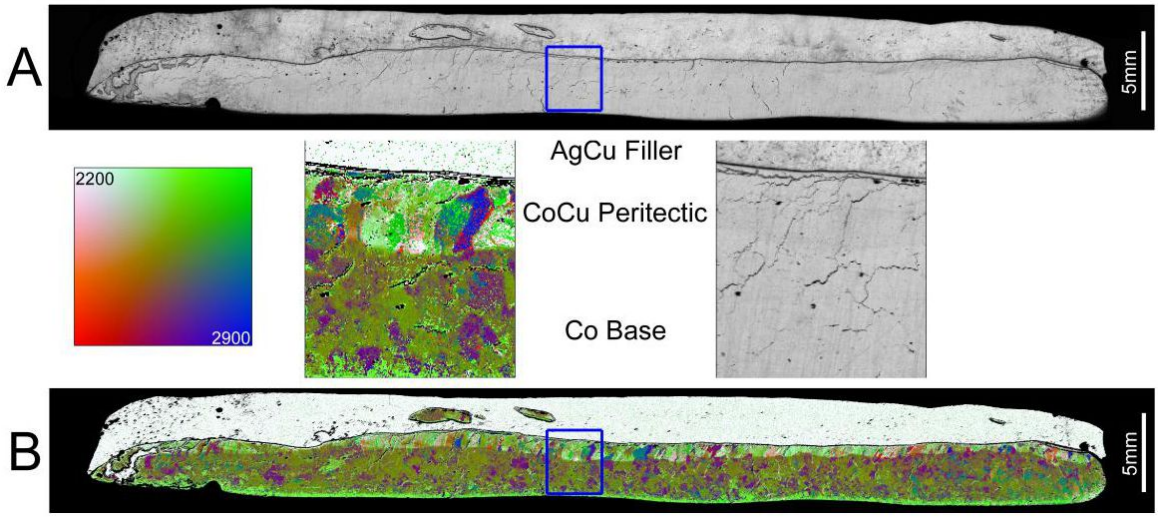

Figure 26: SRAS velocity vector map and optical weld images

SRAS velocity vector map and optical image of a central, longitudinal weld section. The weld start is oriented to the left.

A: Optical micrograph illustrating the large amount of cracking in the CoCu peritectic region. Also note the large amount of porosity near the weld start.

B: SRAS velocity vector map shows the SAW sound speed as a function of two orthogonal wave directions and location. The white area to the top is the AgCu filler, which provides no acoustic data. Below the filler is the CoCu peritectic region, indicated by large, predominantly bright green macrozones. Below this is the dull green and brown cobalt base.

Although observed wave velocities are probably a result of all of these effects, determining their relative importance is complicated by the lack of data for a simple, as cast Co structure. However, SRAS was able to conclusively establish the existence of the CoCu peritectic region as well as the existence of macrozones inside this region.

Further analysis of these welds involved optical microscopy on top and bottom weld faces, utilizing the methods described in Section 3.6. Directional grain growth is evident on both faces, inside the melted cobalt base (Fig. 27). The weld root shows a mixture of disordered grain growth, and grain growth away from the start of the first pass. Because a back and forth pattern was used to create the welds (Fig. 2), this preferential grain growth indicates that most grain growth at this weld root occurred during the first pass, and cannot originate from subsequent passes. This observation is confirmed for most welds, and suggests that power be increased for pass 2.

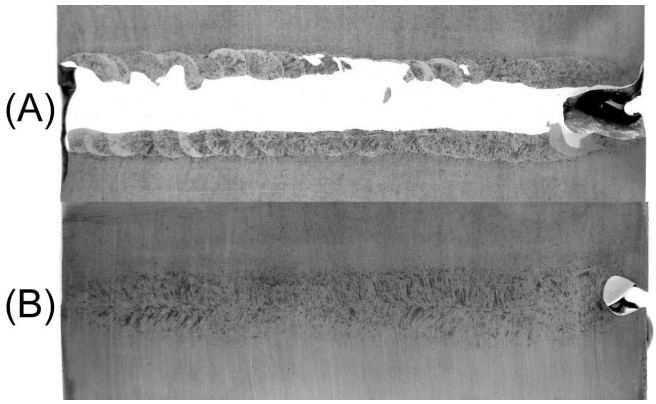

Figure 27: Weld macrostructure

Weld macrostructure revealed by polishing slurry. Weld start is at left.
A: Weld face showing filler pool (white) surrounded by cobalt. Each semicircle corresponds to a dab of filler applied to the weld. The overlapping semicircles indicate pass direction.
B: Weld root showing directional grain growth corresponding to the initial pass. Note also the central grain boundary running along the entirety of the weld.

The weld face shows a series of overlapping circular structures, corresponding to the dabs of filler applied during the third and fourth passes (Fig. 27). These passes are performed to the side of the original J-groove (Section 3.3), and substantially extend the melted region to either side. Examination of four separate welds typically shows between 20 and 25 dabs. The grain growth indicates torch direction, and area of greatest heat. Since the grains are ordered, and the pulses are well defined, it appears that this region was not remelted by the fifth (final) pass.

4.3.2 SEM, FEA and Fracture of Tensile Specimens from Completed Weldments

A single weld was sectioned into two long and five short test pieces for tensile testing (Fig. 7). Although the different test piece geometries will effect displacements and observed stiffnesses, there should be little effect on ultimate failure strength. FEA of these two geometries confirms this assertion; predicted failure strength of the shorter and longer test pieces were 5485N and 5544N respectively. This 1% difference is likely due to slight differences in observed thickness (Table 6).

Two predominant failure modes may be observed during tensile fracture (Fig. 28). The first type corresponds to the primarily brittle failure of the cobalt base, which is followed by the ductile failure of the AgCu filler (Fig. 28). The specific location of the test piece inside the weldment has a large effect on failure strength (Fig. 28B). Tensile testing does not reveal the presence of a well-defined quasi-steady region. Instead, weld quality appears to increase towards the center of the weldment, in contrast with observations during 4-pt bending.

There is reasonable correlation of failure strength with FEA, in that observed failures occur between 44% and 73% of the predicted load (Fig. 28). The difference is larger than the discrepancies observed between FEA and 4-point bending. This discrepancy is likely due to both the lamellar structure of the CoCu peritectic (Figs. 15C, 15D, 24), and the large amount of cracking there (Fig. 26). This region plays only a limited role in failure during face or root bending, but is subject to high stresses in tension, and is the predicted initial location of failure (Fig. 29).

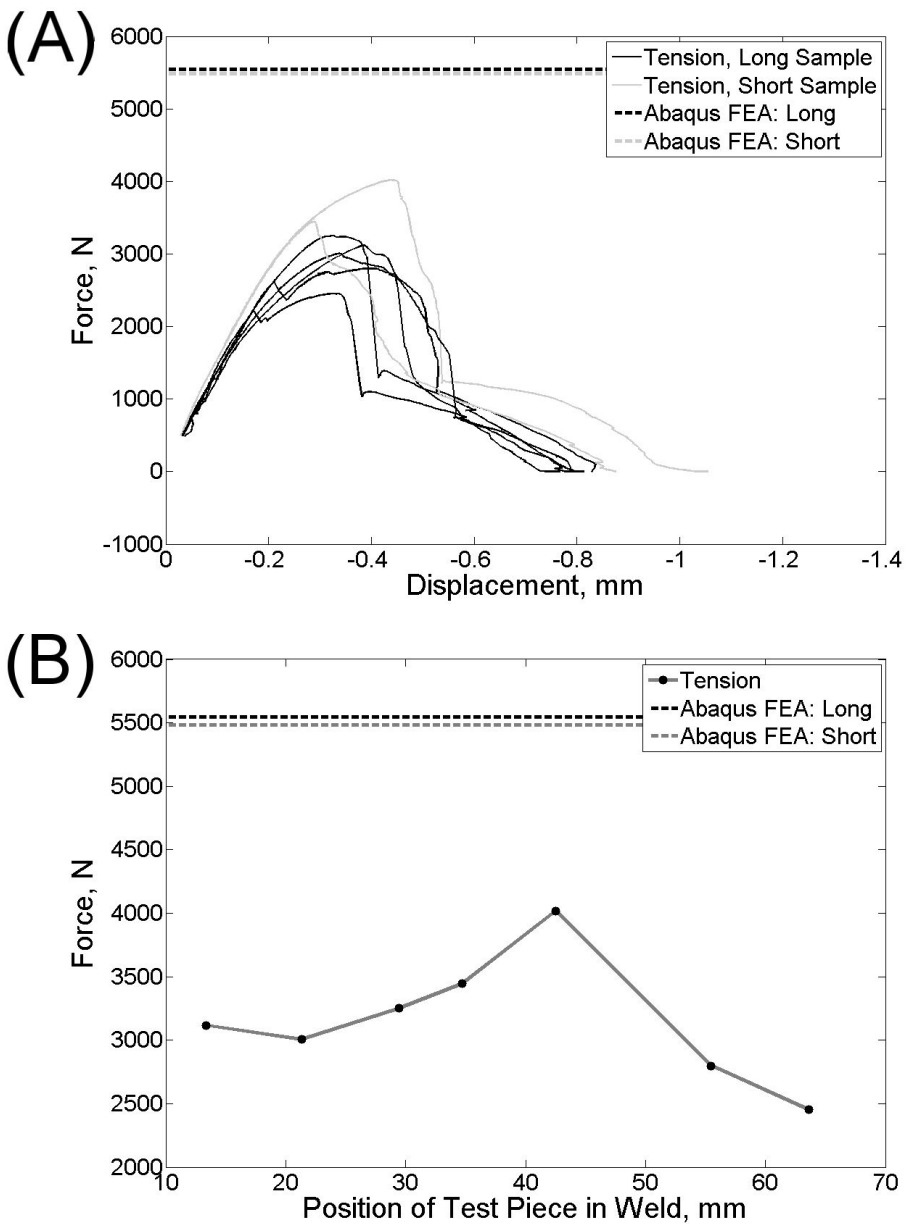

Figure 28: Tension test and FEA

A: Plot of tension test, and FEA predicted failure. Horizontal dotted lines show predicted failure for the long test piece (dark) and the shorter test piece (gray). Solid lines show the measured force/displacement curve tensile failure. Black lines represent longer test pieces, whereas gray lines indicate shorter test pieces. Note the differing curves of each test piece type. Two separate behaviors are observed. First, the load curve corresponds to the loading of the cobalt base. After fracture, a more gradual failure is observed, corresponding to ductile failure in the AgCu filler.

B: Plot showing ultimate tensile force vs. test piece position, and FEA predicted failure. Horizontal dotted lines show predicted failure for the long test piece (dark) and the shorter test piece (gray). Test pieces in the center of the weldment are significantly stronger, unlike most other tests which show a quasi-steady region.

Fractography of these tensile specimens further illustrates the microstructural details of these failure types (Fig. 30). SEM of the AgCu filler shows primarily dimples (Fig. 30A) associated with void initiation, growth and coalescence, typical of ductile failure. Additionally, the filler possesses several smooth voids (Fig. 30, arrows V). These structures are believed the result of cobalt nodules observed in the filler [22], generally close to the base-filler interface. EDS shows these dimples to be composed of silver rich AgCu (Table 9), when compared with the Ag-40 at%Cu wire. This discrepancy probably results from Cu diffusion across the base-filler boundary; however, this observation is not definitive due to porosity-induced uncertainties. Cu diffusion into the Co base is supported by WDS (Figs. 24, 25), and by the subsequent EDS measurements having a much higher Cu/Ag ratio than the filler wire.

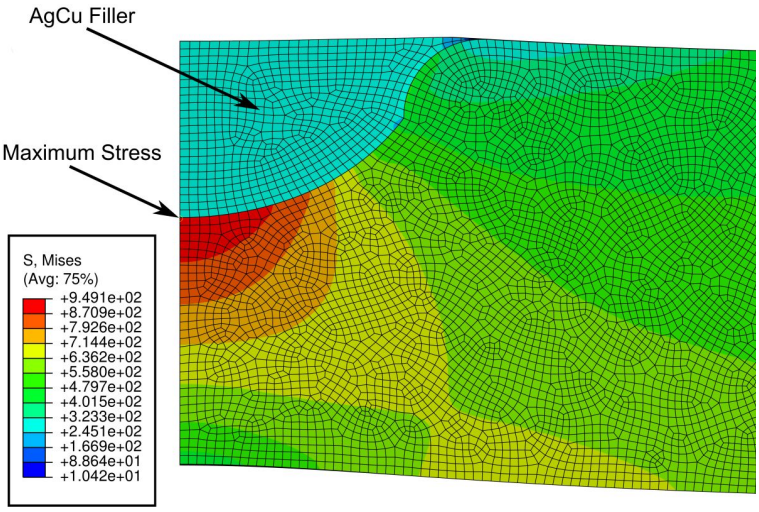

Figure 29: Predicted von Mises Stress at tensile failure
Distribution and magnitude of stresses during tensile failure. Filler is located up to the left; force is applied horizontally to the right. Note the high stress concentration in the cobalt, immediately below the filler region. This corresponds to the CoCu peritectic region on the actual welds.

In contrast with the AgCu filler, the CoCu peritectic possesses features associated with both brittle and ductile failure (Fig. 30B). This region is characterized by cleavage steps, covered with shallow dimples (Fig. 30B). The cleavage steps are consistent with

brittle failure of lamellar structures, such as those observed in other welds (Figs. 15, 24B). The dimples suggest the presence of a ductile layer of AgCu, an observation supported by high concentrations of AgCu measured by EDS (Table 9). These concentrations along this failure surface greatly exceed the AgCu concentrations measured by WDS of the weld section (Fig. 25), which also suggests that failure has occurred along a small AgCu layer, such as a backfilled crack.

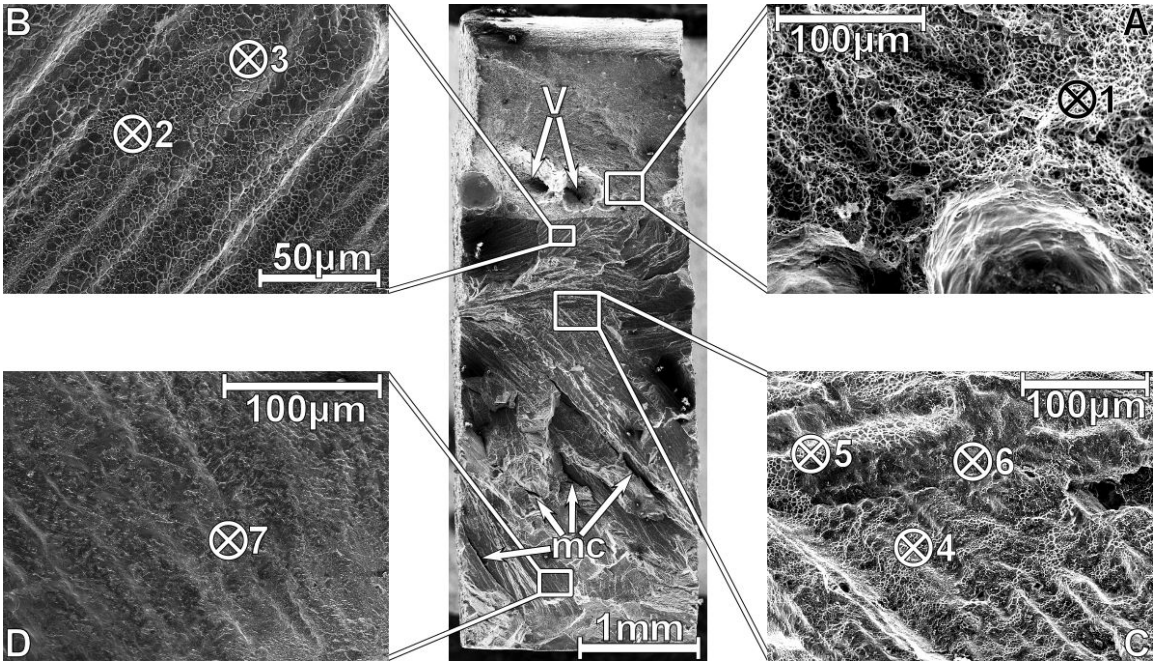

Figure 30: SEM fractography of tensile failure surface

Fractograph of the entire tensile failure surface shows distinct failure types associated with different weld regions. Filler is located at the top, and is characterized by ductile behavior. Several voids (arrows V) are believed to result from Co nodules. Below this region, the cobalt base is characterized by primarily brittle failure and microcracks (arrows mc). Roundels inside inserts designate EDS locations (Table 4).

A: Ductile failure of the AgCu filler is indicated by dimples with ~5 µm. Large smooth voids are probably the result of Co nodules near the base-filler interface.

B: Failure of a suspected backfilled AgCu crack surrounded by the CoCu peritectic. Cleavage is thought to result from the brittle failure of the lamellar peritectic, while dimples result from the ductile failure of a AgCu backfilled crack.

C: Failure of a backfilled AgCu crack, believed inside the Co base region. Facets probably result from brittle failure of the Co, while dimples result from ductile failure of the AgCu.

D: Primarily brittle failure of the Co base, far from the base-filler interface. Failure appears to be intergranular.

The combination of brittle and ductile failure modes is also observed further from the filler (Fig. 30C). This region is suspected to consist of relatively pure cobalt (Fig. 25), with intermixed AgCu cracks, although the fractograph does not permit definitively determining the border of the Co base and CoCu peritectic. Brittle failure is evidenced by multiple facets, whereas dimples, like before, indicate a ductile failure mechanism. EDS measurements show varying concentrations of AgCu; notably an area with no dimples (Table 9, #6) has a much lower AgCu concentration. The observed failure surface, as well as the high AgCu concentrations, appears to result from the failure of a backfilled crack.

Failure mechanisms even further from the filler appear brittle (Fig. 30), corresponding to the general lack of backfilled cracks in the weld root (Fig. 26). The Co base has multiple microcracks (Fig. 30, arrows marked mc) and facets, both associated with brittle failure. Closer examination shows a relatively flat failure surface, devoid of dimples (Fig. 30D). Tentatively, this is attributed to intergranular failure. EDS confirms this fracture surface is composed of nearly pure Co, although a small amount of Cu is observed, which may have segregated along a grain boundary.

Table 9: Material Composition by Region

Location	Region	Co (At%)	Ag (At%)	Cu (At%)
1	AgCu Filler	0	64	36
2	CoCu Peritectic	48	28	23
3	CoCu Peritectic	44	27	30
4	Co Base	51	24	24
5	Co Base	46	23	31
6	Co Base	88	4	8
7	Co Base	97	0	3

4.3.3 Fracture of an Unground, Completed Weld in Root Bending

A single weld was cut into 20 sections for 4-point root bending tests (Fig. 8). These results were compared to the completed weld from [22], in order to verify the quality of the newer welds, as well as the approximate location of the quasi-steady zone. Because the sections used have different widths, the reported loads have been normalized by width. The newer weld failed at higher displacements and normalized loads than the previous weld, likely due to superior material quality (Fig. 31). If the region between 31 and 54 mm is considered, the newer weld fails, on average, at a 16% higher load. This improvement is not surprising, due to the large amount of practice the welder had between the 5 pass weld produced in our previous study (Section 4.2), and this one.

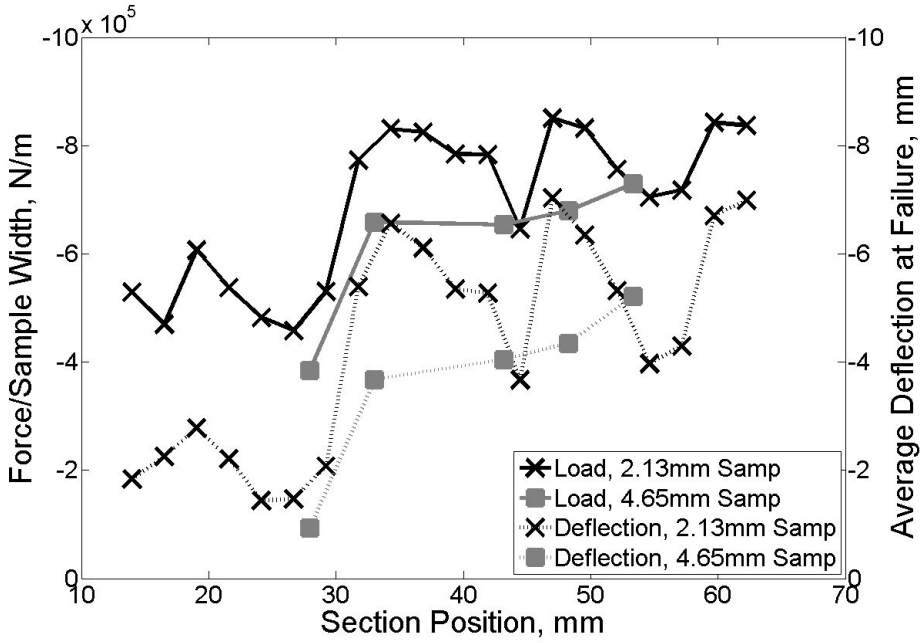

Figure 31: Failure strength and displacement of unground welds
Plot shows the failure strength and displacement of sections from unground welds in root bending. Sections from the unground weld from this study (X), are compared to a weld from the previous paper [22] (Square). The sections from this study were significantly smaller than the last, with a thickness of 2.13 mm vs. 4.65 mm. This results in slightly more chaotic behavior for the newer weld. However, both the strength and displacement have generally increased. Based on these values alone, it appears that the quasi-steady zone of the more recent weld extends from 30 mm to the final section at 62 mm.

More importantly, this test indicates the location of the quasi steady zone, and the expected variability between sections. The quasi-steady zone is a region in the center of the weld which experiences homogenous thermal conditions. The presence of a quasi-steady zone generally results in stronger welds, and more consistent behavior. This region appears to begin between 29 mm and 31 mm, and to extend beyond the last section at 62 mm. This is a highly subjective evaluation, which may vary considerably from weld to weld.

Inside this quasi-steady region, this newer weld appears less consistent than the original. However, this is mostly due to the reduction in section size, which increases the importance of cracking, and other random structural anomalies. Overall, the standard deviation inside the quasi-steady zone is approximately 8% of the average force at failure for a 2.13 mm thick section.

4.3.4 Fracture, SEM and FEA of Completed Welds in Face and Root Bending

Three welds were ground and cut into 21 sections for 4-point face and root bending tests (Fig. 8). The best and worst examples for each of these tests was imaged using the SEM. Finite element models were also made for both of these tests.

Grinding of these welds was performed in order to make their geometry uniform, and to simplify comparison with the residual stress tests (see Section 4.3.5). However, removal of the weld root will weaken these welds and potentially change the site of initial failure.

Face bending results in fairly consistent behavior across the weld, with no significant positional dependence (Fig. 32). Root bending exhibits a much higher degree

of variability (Fig. 32), with a strong dependence on section position. The sections located close to the weld start have a much lower strength than later sections for all three welds. This difference can be interpreted as a result of the varying thermal fields at the beginning of the welding process. The size of this weakened region varies, from approximately 20 mm to 45 mm, depending on the particular weld. The strongest weld has another decrease in strength towards its end, which is likely the result of higher temperatures at the end. The lack of this marked decrease for the other welds implies that their lower strength is caused by inadequate heating.

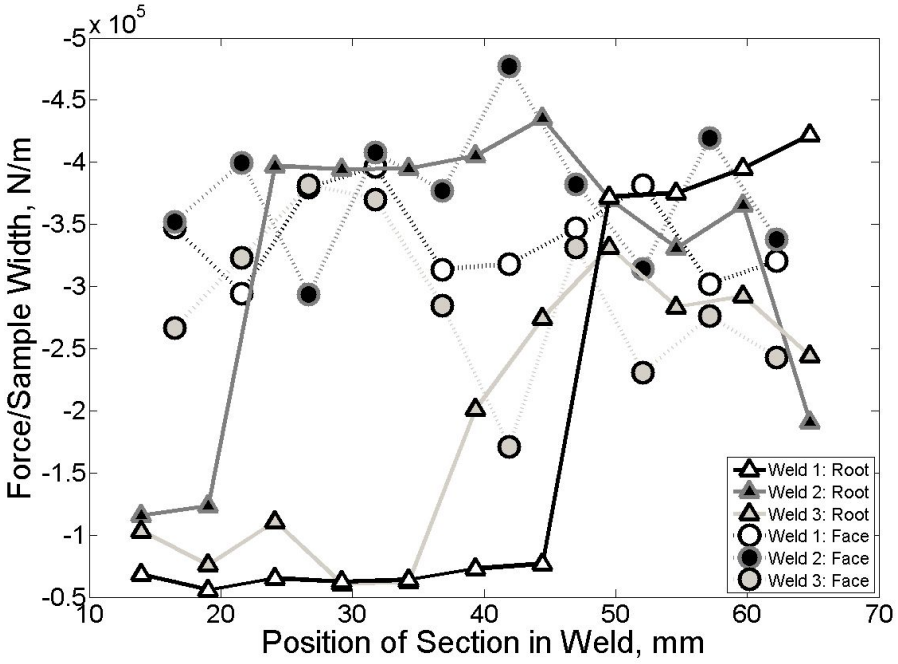

Figure 32: Failure strength of ground welds in face and root bending
Plot shows the failure strength for sections in three ground welds in alternating face and root bending. Face bending (dotted line) is much more consistent then root bending (solid line). There appears to be limited correlation between the two failure types. Furthermore, root bending is dependent on section position, while face bending does not have an obvious dependency.

Finite element analysis reveals two possible mechanisms for failure in root bending. Excessive stress at the center of the weld root (Fig. 33A) can cause failure of the cobalt base in tension, or contribute to the failure of preexisting cracks. Previous FEA predicts

weld failure to occur on one side of the weld root [22]. This difference is believed to be due to the effects of grinding the weld prior to fracture. FEA also predicts failure via excessive, compressive deformation of the filler (Fig. 33B), however this mechanism does not appear to be as significant.

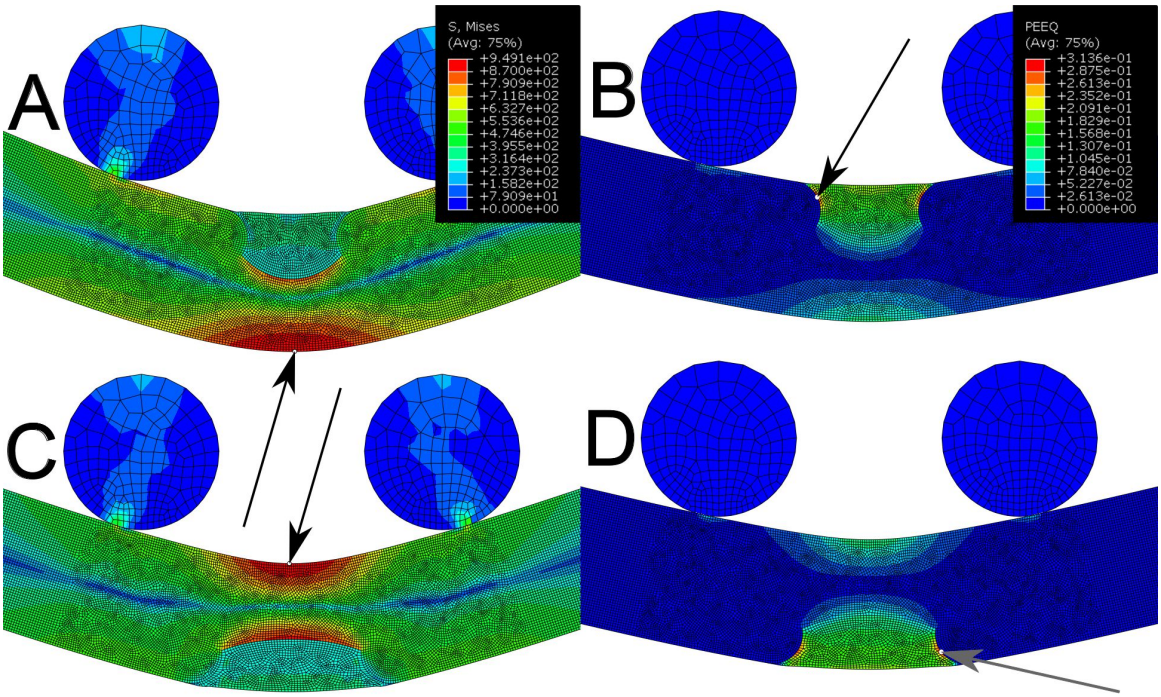

Figure 33: FEA of root and face bending

Only 2 of the 4 rollers are pictured (compare with Fig. 3). All images started as the average geometry (Table 6). Maximum values indicated by arrow.

A: FEA showing predicted von Mises stress at failure in root bending. Note the stress concentration in the center of the weld root. Imperfections in this area will contribute to failure.

B: FEA showing equivalent plastic strain (PEEQ) at failure in root bending. Note the failure, due to excessive deformation, of the AgCu at the side of the filler pool.

C: FEA showing predicted von Mises stress at failure in face bending. Note the stress concentration at the center of the weld root. This will cause failure in shear.

D: FEA showing equivalent plastic strain (PEEQ) at failure in face bending. Note the failure, due to excessive deformation, of the AgCu at the side of the filler pool. This suggests that these welds may also fail via delamination.

Predicted failure in face bending also occurs via two separate mechanisms. Excessive deformation of the filler adjacent to the base/filler boundary (Fig. 33D) may contribute to weld delamination, or tensile failure of the filler. Failure of the cobalt base in compression is also predicted (Fig. 33C).

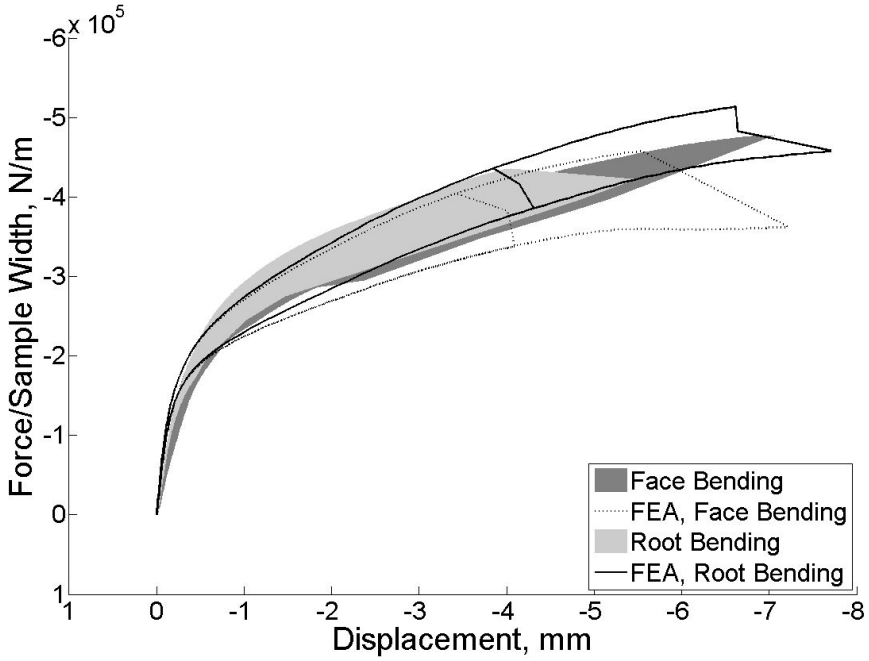

Figure 34: FEA predicted and observed failures in face and root bending

Plot shows the FEA predicted failure curves (outline) and observed curves (solid) for face and root bending. The boundaries of the FEA curves were determined using the 3 separate models described in Section 3.10.3. The middle division shows the onset of failure in the filler, due to excessive plastic deformation. The solid regions were calculated using only sections exhibiting cobalt failure. The shaded areas enclose the load displacement curves until their ultimate failure. Note the overprediction of failure loads in root bending, and the underprediction of several failures in face bending. Note also how the onset of AgCu failure corresponds more closely with the face bending test.

Three separate models were created in order to estimate the uncertainties in the force vs. displacement curves (Tables 6, 7). These models show slightly higher forces and displacements at failure in root bending than face bending (Fig. 34). Trends closely follow predicted behavior for both face and root bending, if the poorest quality root bending sections are excluded. However, observed displacements in root bending are generally lower than face bending (Fig. 32), implying that failure is occurring prematurely due to material quality.

SEM images of the strongest and weakest weld sections illustrate the effects of defects and geometry (Fig. 35). The weakest root bending section failed via cracking in the cobalt base (Fig. 35A), consistent with FEA predictions. However, failure occurred

at substantially lower load than predicted, suggesting that material quality of this specimen is low. Base-filler delamination also occurred, most likely after initial failure. This section also has large backfilled cracks, evidence of voids along the failure surface, and smaller, open cracks. It also has a large filler region, which will contribute to a high stress concentration in the base. The failure surface follows a small preexisting, backfilled crack close to the filler. Although it is not possible to conclusively establish the presence of cracking before flexure, the presence of other, open cracks suggests that failure followed a preexisting open crack.

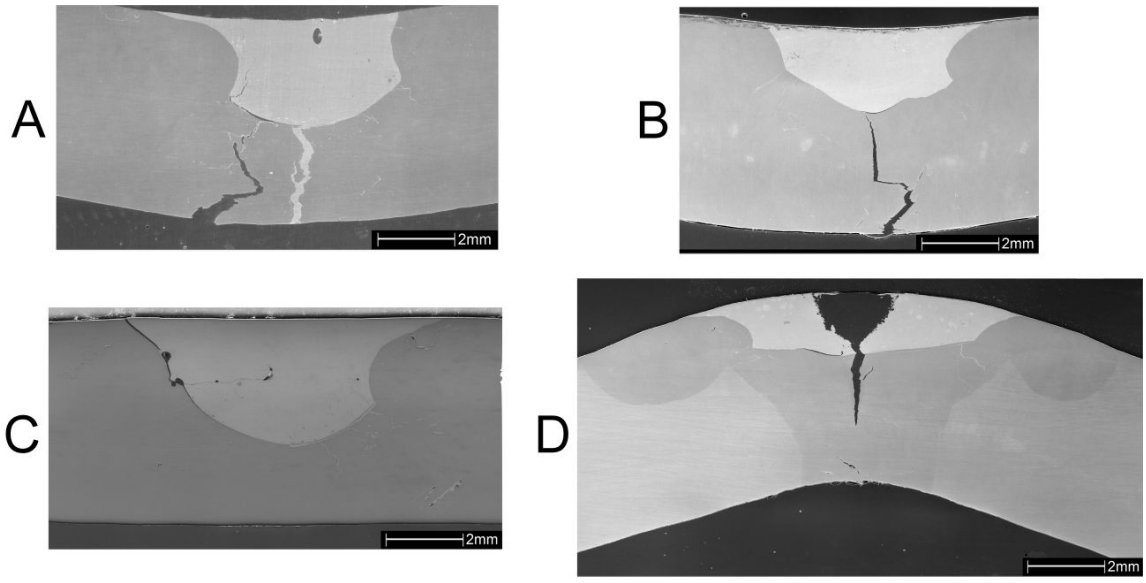

Figure 35: SEM of failures in root and face bending

A: Micrograph showing the weakest section in root bending. Note the number of backfilled cracks in the cobalt base. Examination of the failure surface reveals porosity, and the presence of preexisting cracks without AgCu backfill.

B: Micrograph showing the strongest section in root bending. Note the matching failure surfaces of the crack. The straight failure, under the filler region, implies intergranular fracture.

C: Micrograph showing the weakest section in face bending. Note the number of voids and imperfections, especially along the base/filler boundary. Failure appears predominantly by delamination.

D: Micrograph showing the strongest section in face bending. An outline showing the melted cobalt is also observed. Failure is predominantly central, and excessive necking of the AgCu filler is observed. However, this occurs away from the interface. Some delamination occurs, but this does not appear to be predominant. Note also the shear failure of the cobalt root.

In contrast, the strongest section (Fig. 35B) has a smaller than average filler region, and only minimal backfilled cracks, toward the side of the weld. As before, delamination has occurred after failure. Failure below the filler appears is centered and straight, suggesting that it has occurred along the centralized grain boundaries.

The weakest face bending section (Fig. 35C) also exhibits significant defects, as well as a larger than average filler region. In this case, failure occurred via base-filler delamination. The boundary has several significant voids which are directly along the path of failure. The filler also has several voids, which appear to play a minor role in failure, due to the presence of a horizontal crack. The presence of voids along the base-filler boundary suggests poor base-filler adhesion. Furthermore, the shape of the left side is not consistent with the general shape observed in these welds, indicating an error in welding technique.

The strongest face bending section (Fig. 35D) was imaged after 0.03 micron polishing, revealing this weld's basic macrostructure. Overall, the geometry of this weld resembles the weld produced in the previous study (Fig. 14). The darker gray region indicates the extent of melting, which is roughly symmetric. The filler region is small, increasing the amount of cobalt available. Backfilled cracking is observed, but occurs only to the side of the filler. Some delamination is also observed, as well as intergranular, tensile failure and shear failure in the base. However, the main mode of failure involves necking of the filler. The high strength of this weld section is due to a combination of favorable geometry, adequate adhesion, and high quality materials.

In all cases, weld quality is clearly influenced by geometric factors and material imperfections. The large amount of discrepancy in the root bending test is due to the

cobalt base being prone to cracking. This behavior results in much greater sensitivity of the root bend test to thermal differences during weld manufacture. The face bending test is also subject to similar effects, but the ductile filler is unlikely to form cracks. The defects most likely to cause poor performance are voids in the filler, and along the base filler boundary.

4.3.5 Residual Stress, Heat Treatment, and Root Bending

Four welds were ground and cut into 7 sections for heat treatment, residual stress measurement, and root bending tests (Fig. 8). Grinding the residual stress sections into a consistent cross section is essential for analysis, but will potentially alter residual stresses. Two separate regions were defined for each weld; each region was either left as is, or subjected to a 325°C heat treatment for 100 hours. Five of these welds had their residual stresses measured by crack compliance; data reduction was performed using FEA.

This low level heat treatment had no statistical effect on strength. If all samples are considered, the t-test reveals a 24% likelihood strengths are influenced by heat treatment. If sections 1 and 2 from every weld are removed from this study, in order to reduce the effect of material defects, the probability of this being a random distribution rises to 92%.

Residual stress measurements were successfully completed on 5 sections (Fig. 36). Two of these sections have a slitting error at approximately 0.1 mm. While this error is far from the area of interest, it does affect the trends at the beginning of the plot. For these samples only maximum stresses are reported (Table 10).

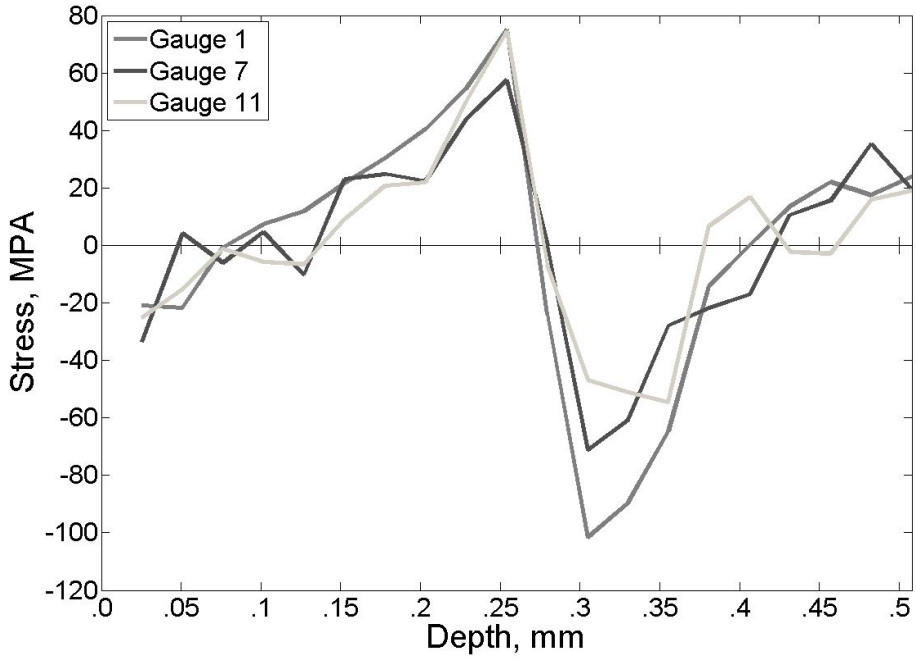

Figure 36: Measured residual stress

Plot shows the measured residual stresses vs. EDM cut depth. The top of the section is at a depth of zero; thus the AgCu filler is located at low depth, and the Co base begins at around 0.3 mm. Note the large tensile stresses in the filler, opposite the large compressive stresses in the base. Also note the small area of tensile stress in the weld root, which begins at about .4 mm.

Table 10: Residual Stress, MPa

Gauge	Weld	Section	Type	Heat Treated	Maximum Tensile	Maximum Compressive	Maximum Tensile, Root
1	1	7	Temperature	Yes	75.14	-101.7	23.91
7	3	7	Temperature	No	57.58	-71.3	35.28
8	2	4	Time	Yes	71.1	-78.75	29.74
9	3	2	Time	No	51.61	-80.74	41.45
11	1	4	Temperature	No	74.5	-54.6	18.87

Heat treatments do not appear to have affected the maximum stresses (Table 10). This conclusion correlates with earlier observations in four-point bending. The welds are subjected to multiple welding passes at significantly higher temperatures than the applied heat treatment, thereby limiting its effectiveness.

The residual stress profile observed is unlikely to influence failure. The areas of high stress are in the sample center, along the base-filler interface (Fig. 36). According to both our FEA predictions (Fig. 33) and the SEM observations (Fig. 35), this region is not

the location of failure in bending. Furthermore, these stresses place the CoCu peritectic under compression, which should strengthen the region during tensile tests. In general, compression in this area is expected to be beneficial, considering the large amount of preexisting cracks (Fig. 26), and the tendency of cobalt to experience brittle failure. Limited tensile residual stresses exist at the weld root (Fig. 36, Table 10); according to our finite element analysis, these stresses are the correct direction to influence failure during root bending. However, these stresses average only 28.7MPa, which is approximately 3% of the failure strength; much less than effects of geometry and imperfections. Due to the nature of the crack compliance method, it is not possible to measure residual stresses occurring at the very end of the sample, nor is it possible to measure stresses in the area removed by grinding. However, residual stress trends toward the weld root are relatively flat, indicating that the above estimate is reasonable. As such, effects of these stresses upon failure have not been observed.

Chapter 5. Surrogacy Discussion

The surrogate approach presented earlier [22,23] and here is a viable method to investigate weldments of toxic metals using safe substitute materials. The surrogate Co-AgCu system was selected to mimic the behavior of the Be-AlSi welding system as closely as possible, with special attention paid to residual stresses and failure mechanisms (Section 1.4, [22,23]). The cobalt base was selected mainly due to its HCP crystal structure and high stiffness, which are similar to beryllium, although other mechanical and thermal properties were also considered [22]. Furthermore, the AgCu filler was selected due to its immiscibility in cobalt, its eutectic structure, its ductile nature, and the large mismatch in coefficients of thermal expansion between it and cobalt [22]. Therefore, the Co-AgCu system represents the best possible surrogate of the Be-AlSi welds [22,23]. Due to the similarities between these two systems, the geometry, failure mechanisms, and mechanical behavior of the Co-AgCu surrogate are expected to mimic the the Be-AlSi welding system.

The concept of surrogacy is not unique to these welding systems, and may be of use in the analysis of other weldments involving toxic, rare, or expensive materials.

5.1 Advantages and Drawbacks of Surrogacy

Analyzing beryllium weldments via surrogacy is advantageous due to the high cost and toxicity of beryllium [22,23]. However, this method has several drawbacks, and is expected to augment, not replace, other numerical and experimental approaches.

Because it is not possible to perfectly match material properties, it is necessary to determine surrogate welding parameters which may differ from those used in the parent system (Section 4.1, [22]). This is time consuming and difficult. Furthermore, measurements obtained from the surrogate system are not expected to exactly equal these measurements in the original system, because the parent and surrogate systems are not identical. As with any experimental approach, interpretation is often required to understand results; additional interpretation is required to extend these results back to the parent system. Due to these reasons surrogacy is likely to be more expensive and less straightforward than numerical analysis.

However, surrogacy offers several key advantages over numerical analysis. Unlike computer simulation, surrogacy involves experimental simulation of an entire welding system [22,23]. The features examined in numerical analysis are limited by the complexity of the model, whereas the features of the surrogate welding system will be similar in scale and complexity to the original system. As such, surrogacy is expected to offer a much more complete view of the welding system than numerical analysis. Furthermore, welding surrogacy is much more actionable than numerical analysis, since weld quality is directly linked to fabrication parameters.

In summary, welding surrogacy is cheaper and safer than direct experimentation on beryllium, and also more nuanced and actionable than numerical simulation.

5.2 Implications for the Be-AlSi System

The predominant conclusion of this study is that failure in Co-AgCu welds is a result of weld quality and geometry, not residual stresses [23]. As discussed earlier (Section 4.3), weld strength can be related to the relative sizes of the base and filler pools, as well as the number and location of other cracks and imperfections. Extending the results of this study to the Be-AlSi welds would best be accomplished through numerical analysis. Unfortunately, this research has been completed due to limited time and resources. However, analysis of weld geometry and material properties of both the base and surrogate systems allow comparison, and several key conclusions can be formed.

5.2.1 Effects of Geometry

The Be-AlSi and Co-AgCu welding systems both possess similar base-filler relationships (Section 1.4). These include a comparatively weak ductile filler, a strong, brittle base, and a lack of solubility between components. As such, geometric factors affecting these two systems are likely comparable. Study of the Co-AgCu welding system indicates that strong welds usually posses a small filler region, surrounded by a large region of melted base metal (Section 4.3.4, [23])

The Be-AlSi welds show very limited penetration, a small area of unmixed, beryllium melting, and a large filler pool (Fig. 37) [54]. Since these welds exhibit only partial penetration, a crack exists at the base of the weld (Fig. 37, [54]), which will function as a severe stress raiser. Small changes in weld power, or the presence of filler inside this fissure could drastically alter the geometry of these welds and their predicted strength. Both FEA and fractography of our surrogate welds indicate that welds with

minimal base melting, such as these, are much weaker than welds with more substantial base melting [23]. As such, strength of the Be-AlSi welds will be highly dependent on geometry. Efforts to improve the strength of the Be-AlSi rings should therefore focus on increasing the amount of penetration, as this will greatly increase the nominal strength of the weldment.

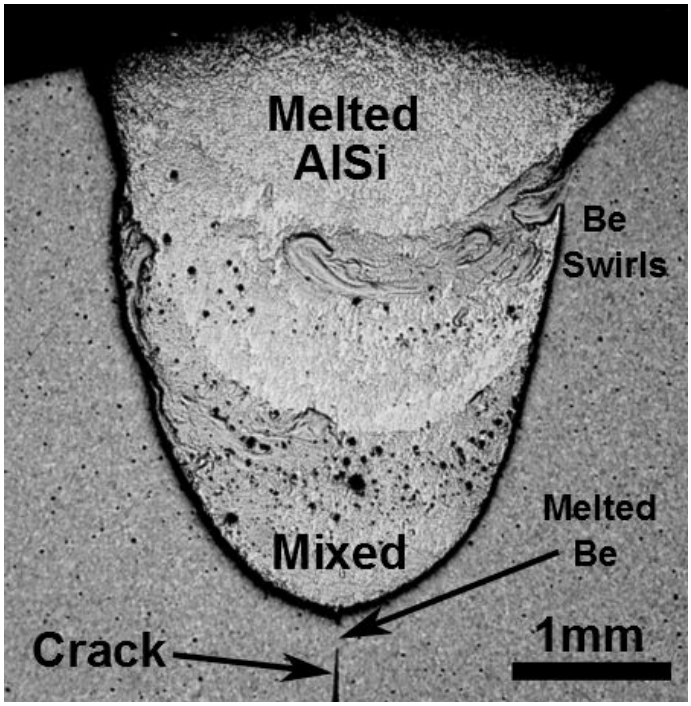

Figure 37: Optical micrograph of a Be-AlSi weld
Micrograph showing a chemically etched Be-AlSi braze weld produced at Los Alamos National Lab. The top of the micrograph is composed of melted AlSi filler. Below this, the Be base and AlSi filler mix. Porosity exists in this region, although the etching may have exacerbated these effects. Below this is a small region of melted Be. At the bottom is a significant crack, formed to to incomplete base melting. Image modified from [54]

5.2.2 Effects of Cracking and Porosity

Failure in the Co-AgCu system is strongly influenced by material quality, especially the number and location of cracks, and the amount of porosity (Section 4.3, [23]). Fractography indicates that failure of AgCu backfilled cracks is of particular importance, due the fairly large number of such features, and the lower strength of the AgCu filler.

Since the Co-AgCu and Be-AlSi welding systems possess similar base-filler relationships (Section 1.4), existence and effects of these cracks are likely comparable in both systems.

Significant porosity in the Co-AgCu welds is generally restricted to the area near the weld start or finish (Fig. 26). Therefore, only minimal data exists pertaining to the importance of porosity to failure. However, welds with significant porosity generally exhibit low strength, due to the likelihood of porosity initiated failure (Fig. 35). Effects of both cracking and porosity are expected to be slightly more severe in the parent Be-AlSi system, due to the low fracture toughness of beryllium (e.g., [25]).

Images of the Be-AlSi welds show multiple AlSi backfilled cracks in the melted Be base [54], analogous to the AgCu backfilled cracks observed inside the melted Co base of our surrogate welds (Fig 15). Be-AlSi micrographs also show a large amount or porosity in the fusion zone (Fig. 37, and [23]).

The presence of backfilled cracks in both welding systems shows that our welding surrogacy reasonably approximates system behavior, as formation of these cracks involves base-filler insolubility, hot cracking, and a low melting point filler. Fractrography of the Co-AgCu welds indicates that such cracks contribute significantly to weld failure, and are a preeminent feature affecting weld quality [23]. Presence of these backfilled cracks suggests that weld quality is a critical issue in both the base and surrogate welding systems. These assertion is supported by numerous other research (e.g., [28,29]).

Decreasing the amount of cracks relative to the amount of base melting should increase the strength of the Be-AlSi welds. The most straightforward way to decrease the number of such cracks is to decrease the thermal gradients during welding. There are

multiple methods to decrease these gradients, such as reducing weld power and traverse speeds, preheating the base material, or insulating the weldment. Utilizing a refractory base to insulate our Co-AgCu weldments proved highly successful at improving weld strength and penetration [22,23], and is expected to have a similar effect on the Be welds.

Notably, techniques which reduce cracking may also increase the amount of residual stresses in these welds, as cracking dissipates stress. Despite potential increases in residual stresses, the strength and consistency of Be-AlSi welds with lower crack concentrations should increase substantially.

Unfortunately, porosity of the Co-AgCu surrogate system was generally restricted to the weld pools at the beginning and end of the welds. These areas were generally not investigated, due to high variances in geometry and quality. As such, no systematic study regarding porosity on Co-AgCu has been performed, although it is likely of importance for beryllium.

5.2.3 Effects of Residual Stress

Measurement of the residual stresses in the Co-AgCu welds, along with FEA and heat treatment studies, shows that they do not affect weld failure (Section 4.3.5, [23]). These stresses are too low and generally not in the correct direction to influence weld failure. Furthermore, residual stresses are of secondary importance to geometry and weld quality; therefore any possible effect of these stresses will be obscured by random changes in weld quality or geometry.

Although our surrogate Co-AgCu system was developed in order to emulate the parent Be-AlSi system, analysis of material parameters indicates not only that residual

stresses will be higher in the parent system, but also that the parent system will be more sensitive to their effects (see Tables 2,4). The base-filler mismatch in coefficients of thermal expansion is greater in the Be-AlSi parent system, which may result in higher stresses. At the same time, the ultimate tensile strength of beryllium is lower than the strength of cobalt [26]. As such, it is more difficult to conclusively establish the insignificance of residual stresses in the Be-AlSi system than it is to establish the importance of cracking or geometry. However, analysis of residual stress data in the beryllium welds still indicates that these effects are of secondary importance.

Although a study combining residual stress and failure strength inside the Be-AlSi welds has not been performed, the residual stresses inside these welds has been measured using neutron diffraction [31]. These measurements show that residual stresses vary from approximately 100 MPa in compression to 100 MPa in tension, with a majority of these stresses existing between 50 and -50 MPa [31]. As such, the stresses in the Be-AlSi parent system are similar in magnitude to the residual stresses measured in the Co-AgCu surrogate system (Section 4.3.5). Since the ultimate tensile stress of beryllium (310 MPa) [26] is lower than the ultimate tensile stress of cobalt (760 MPa) [26] residual stresses may play a larger role in material failure. However, these stresses are still a modest fraction of the ultimate tensile strength. The surrogate Co-AgCu welds experience variances in strength far in excess to this fractional value due only to variances in weld quality and geometry. However, these effects should be much less important in the Co-AgCu welds, due to their superior geometry and smaller proportion of cracks in the melted base. Therefore, residual stresses are likely to play a secondary role to geometry and weld quality in the Be-AlSi welds.

5.3 Suggested Experiments for the Be Al-Si Welding System

Establishment of our surrogate system was based on structural, chemical, mechanical, and thermal similarities (Section 1.4). As such, similarities between these systems are both observed (Section 5.2) and expected. However, such relationships do not constitute proof of surrogate efficacy. Experimental correlation is still required.

However, direct experimentation on the Beryllium Aluminum-Silicon welds is difficult, due both to the toxicity of Beryllium and the specialized nature of the welds. These welds are produced robotically inside a sealed chamber, at Los Alamos National Laboratory, using the PIGMA welding process (see Section 2.1, [31]). As such, exactly reproducing these welds would require significant investment, and is beyond the current capability of this university. Acquiring these welds is also difficult, due to the secretive nature of Los Alamos National Lab. For these reasons, it has not been possible to directly correlate the behavior of the Be-AlSi and Co-AgCu systems experimentally.

Future experimental correlation can focus on improvement of welding techniques (Section 5.4) or on fracture, microscopy and residual stress measurement. A large amount of residual stress measurement [31] and microscopy [54] has already occurred on the Be-AlSi welding system. However, these results have not been adequately correlated. Furthermore, these results have not been correlated with failure. Failure testing of the Be-AlSi welds is essential to determine the relative importance of residual stresses. Performing failure tests on the Be-AlSi welds, and relating these tests to residual stresses, geometry and microstructure could validate the usefulness of welding surrogacy.

5.4 Improving the Be-AlSi Welding System

The welding techniques used to weld the surrogate Co-AgCu system should directly translate to the parent Be-AlSi system due to similarities in geometry, chemistry, morphology, and material properties [22,23]. As in the current Be-AlSi system, initial cobalt welds suffered from incomplete penetration and heavy cracking. Perfecting the Co-AgCu welding parameters revolved around improving weld strength while increasing consistency (Section 4.1, [22]). As such, these techniques should be of use in the improvement of the original Be-AlSi system. Improving the Be-AlSi welds using the methods discussed here would validate the usefulness of welding surrogacy.

Early attempts at joining the Co-AgCu weldments using MIG failed due to inadequate penetration, probably a result of the significant differences in base and filler melting points (Tables 2, 4). Switching to TIG with He top-gas, and reducing filler deposition during the first pass allowed full penetration of our surrogate. Therefore, switching the welding method for the Be-AlSi system from MIG to TIG should also correct these issues in the beryllium welds. Significant precedent involving the success of TIG on beryllium welds already exists [30, 107], although these methods predate modern safety precautions. Changing welding methods requires that welding parameters, such as traverse speed and power, be re-optimized, and that additional equipment be purchased for TIG automation (see Section 2.1).

Forming welds with deep penetration has some drawbacks, mainly involving the greater amount of heat required. Early TIG cobalt welds suffered from excessive cracking, due to an insufficient number of passes and probable oxidation of the base metal. It would be difficult to reduce oxidation in the Be-AlSi welds, since these welds

are already produced in an inert environment. Several methods were used to ameliorate the other issues in our Co-AgCu surrogate; critically, the number of passes was increased from three to five, the Co plates were preheated to 225°C, and the base of the weld was insulated with a refractory material. Staggering, rather than stacking, the passes (Fig. 12) should further reduce internal stresses during cooling and reduce cracking. Slowing down the traverse speed, decreasing torch power, preheating the weldment, and allowing it to slowly cool can all reduce thermal gradients.

Finally, the geometry of the Be-AlSi welding system should be optimized. If possible, passes should be placed on both the exterior and interior of the ring (see [30]), and the thickness of the weldment should be decreased.

Focusing on the effects of residual stress, rather than geometry or material quality, is erroneous for another reason. It is not possible to change basic weld geometry after the weld has been produced. Similarly, quality issues such as cracking and porosity are difficult to remove without remelting the weld. However, residual stress amelioration, through post-weld heat-treatment is possible.

Chapter 6. Conclusions

This research was motivated by the need to understand beryllium welding behavior, without directly investigating beryllium. To accomplish this, a new concept, welding surrogacy, was developed, and a new welding system, Co-AgCu, was perfected. Recommendations regarding the original beryllium welds can be made by investigating failure of this system.

Although the welding techniques developed here have not directly been used in the joining of beryllium, it is asserted that applying similar techniques to the beryllium welds will allow increased penetration, while reducing cracking and porosity.

6.1 Conclusions Regarding the Co-AgCu Welding System

To better understand the nature of Co weldments and to mimic the behavior of the Be-AlSi system, a systematic welding study was performed. This study involved microscopy, WDS, SRAS, fracture in multiple orientations, residual stress measurement (CCM), and FEA.

Cobalt, welded with a silver and copper filler, was the system selected for detailed experimental testing due to the similarity in chemistry, crystal structure, and material properties to the Be-AlSi system. However, once this selection was complete, the concept of "surrogacy" could not be advanced by retaining the original parameters used to weld beryllium with its aluminum-silicon fillers, as this would have resulted in inconsistent, failure prone welds. This study has seen the evolution of the Co-AgCu welding system from heavily cracked weldments, adhered only by their fillers, to strong

consistent weldments, with significant base melting, minimal porosity, manageable cracking and adequate adhesion.

To analyze the new welding system, it was important to obtain welding parameters which result in consistent welds. These parameters were determined in a study which combined optical microscopy and root bending. Although it was possible to weld these two materials together without a parameter study, the results were predictably poor. Furthermore, the random nature of cracking makes the usefulness of such an approach dubious. The best option was to perform a parameter study to improve the welds. The most direct determination of weld quality and consistency is strength. It is unlikely that the welding parameters can be meaningfully improved from this point, because the effects of changing parameters is now smaller than the effects of random cracking. Furthermore, consistency is a desirable quality, perhaps more so then strength. Further optimizing these welds to become stronger seems likely to reduce their consistency, which is already imperfect, as these welds are produced by hand. Configuring a machine to produce such welds is possible, although difficult due to the nuances involved in joining these materials. Ongoing efforts to measure welding power and temperature are a first step to automation.

Once the Co-AgCu welding system was determined, failure of these welds by fracture was investigated by comparing SRAS, WDS, and microscopy to finite element models and to residual stress data. This was performed for welds fractured in tension and four-point bending in both the root and face bending orientations. SEM suggests that failure is mainly a result of weld imperfections and geometric differences, chief among these being cracking and porosity. These imperfections are much more prevalent in the

melted base than the filler, resulting in more consistent behavior for the specimens subject to face bending than to root bending. Finite element modeling predicts loads at failure which are only marginally higher than actual failure loads for best tested specimens. This is consistent with random imperfections heavily influencing failure. Failures in tension exhibit the highest difference between predicted and observed behavior. This is probably the result of the lamellar structure and high prevalence of cracks in the CoCu peritectic region, which were observed using SEM, optical microscopy, and SRAS. This region experiences only small stresses during bending, which reduces the effects of imperfections.

Statistically, heat treatment affects neither strength nor maximum residual stress. The heat treatment was kept at a low temperature (325°C) to prevent cobalt from entering the high temperature FCC phase. Because the temperature was low, no geometric changes or grain refining could occur during heat treatment. However, during welding, they experience five separate passes at much higher temperatures. The fifth and final pass functions as a high-temperature heat treatment for the cobalt base, which is unlikely to experience significant melting. We infer that this final pass prevents the subsequent, low temperature heat treatment from having observable effects on either the residual stresses or failure strengths.

Residual stresses were also shown not to affect weld strength in four-point bending. This is likely due to random imperfections being over an order of magnitude more important than the residual stresses. Furthermore, the maximum stresses occur in the center of the weld, immediately under the base-filler interface, which is an area not significant to failure in bending. The stresses in the cobalt base are predominantly

compressive; changing them is therefore unlikely to affect failure in tension or bending. The corresponding tensile stresses in the filler are also unlikely to observably affect failure due to the high ductility of the AgCu filler.

As a surrogate, the Co-AgCu system shows considerable promise, although experimental verification has not been performed. This surrogate system was based on a number of physical and chemical similarities to the parent, Be-AlSi system, and both systems share several microstructural similarities (Section 5.2). The principal differences between these welds are arguably the weld geometry and the welding techniques. These differences are due to the long optimization process which developed our Co-AgCu welding system.

There is a strong likelihood that development of such techniques will be of use in the Be-AlSi system, as others [30,107] have already utilized similar techniques in other beryllium welds. Furthermore, microstructural similarities, specifically the presence and location of backfilled cracks in both systems (Section 5.2.2), strongly suggest that our surrogate is accurately emulating the expected failure mechanisms in the Be-AlSi welding system.

6.2 Conclusions Regarding Welding Surrogacy

In this thesis, a surrogate Co-AgCu system is used to model the behavior of the parent Be-AlSi welding system. This surrogate indicates that weld quality and geometry are highly important to weld failure in both systems, whereas residual stresses likely play a secondary roll. Furthermore, several new welding techniques have been developed, which should be of use for optimization of the parent welding system. Due to the usage

of surrogacy, these realizations and techniques were developed without the risk of Beryllium exposure.

Due to the use of a surrogate, these results require experimental verification. Some verification already exists due to welding experiments conducted in beryllium aluminum-silicon and other beryllium welds. Microscopy of the Be-AlSi system shows the existence of similar structures, including porosity and backfilled cracks [54]. Development of other beryllium based welding systems provides further support. Weismantel and Taber [30] braze-welded beryllium with a variety of metals using TIG. Similarly to this study, welds were preheated and feature full penetration. In their study on TIG and electron-beam welded beryllium, Hill et al [28] concluded that the main issues involving beryllium welds are cracking and defects. Furthermore, MacPherson and Beaver [107] hand welded beryllium in an inert enviornment using TIG, and insulated their welds using aluminum oxide.

As such, materials surrogacy has demonstrated its usefulness in welding analysis. However, development of welding surrogacy as a concept remains incomplete, because the results and welding techniques developed for the surrogate system have not been verified in the parent, Be-AlSi welds. Therefore, continuance of this research should focus on experiments in the parent welding system.

However, surrogate development required significant time and expense, which will limit its potential applicability.

6.3 Suggestions for Further Research

Further research into welding surrogacy can proceed in three main directions: (1) Sequentially coupled thermo-stress FEA models of both our Co-AgCu system and the original Be-AlSi system could numerically relate the expected behavior of both systems. (2) Direct experimentation on Be-AlSi using the methodology outlined here would conclusively establish the value of this research, but be difficult due to beryllium toxicity, and the specialized equipment required to produce PIGMA welds. (3) The Co-AgCu system could be improved through automation.

References

[1] E..W. Weisstein, *Surrogate.* From: *MathWorld--A Wolfram Web Resource.* Wolfram Research, 2005. http://mathworld.wolfram.com/Surrogate.html. Accessed August, 2015.

[2] J. Mairal. *Optimization with first-order surrogate functions.* In: *Proceedings of the 30th International Conference on Machine Learning,* 2013; Atlanta Georgia. JMRL:W&CP volume 28.

[3] Y. Jin. *Surrogate assisted evolutionary computation: Recent advances and future challenges.* Swarm and Evolutionary Computation, **1**: 61-70, (2011).

[4] N.V. Queipo, R.T. Haftka, W. Shyy, T. Goel, R. Vaidyanathan, P.K. Tucker. *Surrogate-based analysis and optimization.* Progress in aerospace sciences, **41**(1): 1-28, (2005).

[5] J. Barwise, A. Shimojima, *Surrogate reasoning*. Cognitive Studies: Bulletin of the Japanese Cognitive Science Society, **2**(4): 7-26, (1995).

[6] J.D. Cramer, H.C. Britt. *Fission studies of thorium, uranium, and plutonium isotopes with (t, pf) reactions*. Physical Review C, **2**(6): 2350-2358, (1970).

[7] J.D. Cramer, H.C. Britt. *Neutron fission cross sections for 231 Th, 233 Th, 235 U, 237 U, 239 U, 241 Pu, and 243 Pu from 0.5 to 2.25 MeV using (t, pf) reactions*. Nuclear Science and Engineering, **41**(2): 177-187, (1970).

[8] B.F. Lyles, L.A. Bernstein, J.T. Burke, F.S. Dietrich, J. Escher, I. Thompson, D.L. Bleuel, R.M. Clark, P. Fallon, J. Gibelin, A.O. Macchiavelli, M.A. McMahan, L. Phair, C.W. Beausang, S.R. Lesher, B. Darakchieva, M. Evtimova. *Absolute and relative surrogate measurements of the U 236(n, f) cross section as a probe of angular momentum effects*. Physical Review C, **76**(1): 014606, (2007).

[9] J. Hiemenz. *Additive manufacturing trends in aerospace.* Stratasys Ltd, 2014. http://usglobalimages.stratasys.com/Main/Secure/White%20Papers/SSYS-WP-AeroTrends-03-13-FINAL.pdf?v=635513030276305587. Accessed August, 2015.

[10] J.J. Vandenberg, K.R. Knoerr. *Comparison of surrogate surface techniques for estimation of sulfate dry deposition*. Atmospheric Environment, **19**(4): 627-635, (1985).

[11] B. Moghtaderi, T. Poespowati, B. Dlugogorski, E. Kennedy. *Short communication: Application of a surrogate material in assessing the impact of porosity on re-ignition of wood-based materials*. Fire and materials, **26**(2): 99-101, (2002).

[12] S.M. Lewis, J.M. England, R.M. Rowan. *Current concerns in haematology. 3: Blood count calibration*. Journal of clinical pathology, **44**(11): 881-884, (1991).

[13] C.D. Lytle, W. Truscott, A. P. Budacz, L. Venegas, L.B. Routson, W.H. Cyr. *Important factors for testing barrier materials with surrogate viruses*. Applied and environmental microbiology, **57**(9): 2549-2554, (1991).

[14] M. Lyons, D.C. Winter, C.K. Simms. *Extrusion properties of porcine intestines and surrogate materials for ventral hernia modelling*. Journal of the mechanical behavior of biomedical materials, **18**: 57-66, (2013).

[15] M. Wykes, G. Counsell, D. McGlinchey, C.H. Wu. *Tokamak dust, characterisation and removal studies*. Fusion engineering and design, **56**: 403-407, (2001).

[16] E.C. Biemiller. *Results and analyses of irradiation/anneal experiments conducted on Yankee Rowe reactor pressure vessel surrogate materials.* EPRI TR-106001. Research Project 4075-01. Yankee Atomic Electric Company Test Reactor Program. Bolton, MA; December, 1995.

[17] L. Reynolds, T.P. Jones, K.A. BéruBé, H. Wise, R. Richards. *Toxicity of airborne dust generated by opencast coal mining*. Mineralogical Magazine, **67**(2): 141-152, (2003).

[18] H.C. Yang, J.H. Lee, J.G. Kim, J.H. Yoo, J.H. Kim. *Behavior of radioactive metal surrogates under various waste combustion conditions*. Nuclear Engineering and Technology, **34**(1): 80-89, (2002).

[19] C.H. Delegard, A.J. Schmidt, J.W. Chenault. *Mechanical properties of K Basin sludge constituents and their surrogates*. PNNL-14949. Pacific Northwest National Laboratory; November, 2004.

[20] A.K. Kercher, J.D. Hunn. *Results from ORNL characterization of ZrO2-500-AK2 - surrogate TRISO material.* ORNL/TM-2005/540. Oak Ridge National Laboratory; June, 2005.

[21] D.A. Turner, Y. Miron. *Testing of organic waste surrogate materials in support of the Hanford organic tank program - final report*. WHC-MR-0455, UC-600. Westinghouse Hanford Company; January, 1994.

[22] E.M. Criss, M.A. Meyers. *Braze welding of cobalt with a silver-copper filler*. Journal of Materials Research and Technology, **4**(1): 44-59 (2015).

[23] E.M. Criss, R.J. Smith, M.A. Meyers. *Failure mechanisms in cobalt welded with a silver-copper filler*. Materials Science and Engineering, A. (2015) *In press*

[24] H.H. Hausner, editor. *Beryllium: it's metallurgy and properties*. University of California Press: Berkeley and Los Angeles; 1965.

[25] K.A. Walsh. *Beryllium chemistry and processing*. ASM International: Materials Park; 2009.

[26] W.F. Gale, T.C. Totemeier, editors. *Smithells metals reference book*. 8th Edition. Butterworth-Heinemann: Oxford; 2003.

[27] B.W. Jaskula. *2011 Minerals yearbook: beryllium* [advance release]. United States Geological Survey; 2013.

[28] M.A. Hill, B.K Damkroger, R.D. Dixon, E. Robertson. *Beryllium weldability*. In: *Materials Weldability Symposium, in conjunction with ASM Materials Week*; Oct 8-12, 1990; Detroit Michigan. (LA-UR--90-2516).

[29] R.G. Castro, L.A. Jacobson, P.W. Stanek. *Beryllium processing technology review for applications in plasma-facing components*. LA-12545-MS, UC-904. Los Alamos National Laboratory; July 1993.

[30] E.E. Weismantel, K.C. Taber. *Fabrication of beryllium structures by braze-welding, brazing and soldering*. In: *Proceedings of the Second International Conference*; October 15-17, 1964; Philadelphia, Pennsylvania. (Beryllium Technology; Vol 2) pp. 841-855.

[31] D.W. Brown, R. Varma, M.A.M. Bourke, P. Burgardt, S. Spooner, T. Ely, M.R. Daymond, B. Clausen. *Residual Strains in a PIGMA Welded Beryllium Ring*. Advances in X-ray Analysis, **44**: 162-7, (2001).

[32] M.E. Kolanz. *Introduction to beryllium: uses, regulatory history and disease*. Applied Occupational and Environmental Hygiene, **16**(5): 559-567, (2001).

[33] *ASM specialty handbook: nickel, cobalt and their alloys*. ASM: Materials Park; 2000.

[34] *Cobalt monograph. Brussels*: Center D'Information du Cobalt; 1960.

[35] *Cobalt facts*. Cobalt Development Institute; 2013.

[36] K.B. Shedd. *2011 Minerals yearbook, cobalt* [advance release]. United States Geological Survey; 2013.

[37] P. Campbell. *Permanent Magnet Materials and Their Application*. Cambridge University Press: Cambridge; 1996.

[38] D.P. NaBadalung, J.I. Nicholls. *Laser welding of a cobalt-chromium removable partial denture alloy*. The Journal of Prosthetic Dentistry, **73**(3): 285-290, (1998).

[39] M.I. MacEntee, E.B. Hawbolt, J.I. Zahel. *The tensile and shear strength of a base metal weld joint used in dentistry*. Journal of Dental Research. **66**(2): 154-158, (1981).

[40] J. Black, G. Hastings, editors. *Handbook of biomaterial properties*. Chapman & Hall: London; 1998.

[41] E.R. Buchanan. *An overview of hardfaced coatings for industrial use*. In: *Proceedings of the Third International Pump Symposium*; May 1986; College Station, Texas. pp. 91-96.

[42] M. Riddihough. *Stellite as a wear-resistant material*. Tribology, Volume **3**(4): 211-215, (1970).

[43] A. Roth. *Vacuum sealing techniques*. AIP Press: Woodbury; 1994.

[46] O. Untracht. *Jewelry concepts & technology*. Doubleday: New York; 1985.

[47] J.R. Davis, editor. *Alloying: understanding the basics*. ASM: Materials Park; 2001.

[46] M.J. Donachie. S.J. Donachie. *Superalloys: a technical guide*. 2nd Edition. ASM: Materials Park; 2002.

[47] S.C. Levy, P. Bro. *Battery hazards and accident prevention*. Plenum Press: New York; 1994.

[48] M.A. Laughton, D.F. Warne. *Electrical Engineer's Reference Book*, 16th edition. Elsevier Science: Oxford; 2003.

[49] J. Sato, T. Omori, K. Oikawa, I. Ohnuma, R. Kainuma, K. Ishida. *Cobalt-Base High-Temperature Alloys*. Science, **312**(7): 90-91, (2006).

[50] H.-Y. Yan, V.A. Vorontsov, D. Dye. *Alloying effects in polycrystalline γ′ strengthened Co–Al–W base alloys*. Intermetallics, **48**: 44-53, (2014).

[51] *Metal prices in the United States through 2010*. United States Geological Survey, Special Investigations Report 2012-5188; 2013.

[52] *Technical data sheet: Al 718*, Rev. 4. Lucas Milhaupt; April 2011.

[53] *Technical data sheet: braze 720 & 721 (VTG)*, Rev. 6. Lucas Milhaupt; July 2008.

[54] P.W. Hochanadel, W.L. Hults, D.J. Thoma, V.R. Dave, A.M. Kelly, P.A. Pappin, M.J. Cola, P. Burgardt. *Structure/property relationships in multipass GMA welding of beryllium.* In: *82nd Annual AWS Convention*; May 9, 2001; Cleveland, Ohio. (LA-UR-01-23243).

[55] R. Lakes. *Viscoelastic Materials*. Cambridge University Press: Cambridge; 2009.

[56] *ASM Handbook: Vol. 3: Alloy Phase Diagrams*. ASM International; 1992.

[57] H. Okamoto. *Desk Handbook: Phase Diagrams for Binary Alloys.* ASM International: Materials Park; 2000.

[58] I. Karakaya, W.T. Thompson. *Ag-Co (silver-cobalt)*. In: *Binary alloy phase diagrams, Vol. 1*. 2nd ed, edited by T.B. Massalski. ASM International: Materials Park; 1990. pp.25-26.

[59] J.L. Murray. *Ag-Cu (Silver-Copper)*. In: *Binary alloy phase diagrams, Vol. 1*. 2nd ed, edited by T.B. Massalski. ASM International: Materials Park; 1990. pp.28-29.

[60] X.C. He, H. Wang, H.S. Liu, and Z.P. Jin. *Thermodynamic description of the Cu-Ag-Zr system*. CALPHAD: Computer Coupling of Phase Diagrams and Thermochemistry, **30**: 367-374, (2006).

[61] J.L. Murray, D.J. Kahan. *Al-Be (aluminum-beryllium)*. In: *Binary alloy phase diagrams, Vol. 1*. 2nd ed, edited by T.B. Massalski. ASM International: Materials Park; 1990. pp.125-128.

[62] Z. Pan, Y. Du, B.Y. Huang, Y. Liu, R.C. Wang. *A thermodynamic description of the Al-Be system: modeling and experiment*. CALPHAD: Computer Coupling of Phase Diagrams and Thermochemistry, **28**: 371-378, (2004).

[63] G.V. Nikitina, V.N. Romanenko, L.N. Ishutinova. *Energies of mixing in systems containing germanium and silicon with elements of groups III and V*. Inorganic Materials, **7**: 41-44, (1971).

[64] A.L. Udovskii, V.N. Karpushkin, E.A. Kozodaeva. *General algorithm, its mathematical basis and computer autonomic program for calculation of phase diagrams of binary systems, containing p disordered phases of variable and q phases of constant compositions at (p,q) ‹ 10*. CALPHAD: Computer Coupling of Phase Diagrams and Thermochemistry, **19**: 245-277, (1995).

[65] Z. Pan, Y. Du, B. Huang, H. Xu, Y. Liu, H. Chen, W. Xiong. *Experimental study of the Be-Si phase diagram*. Journal of Materials Science, **41**: 2525-2528, (2006).

[66] Y. Du, Q.S. Ran, Z.P. Jin, G. Effenberg, W. Ding. *Optimization and calculation of the Al-Be-Si System.* Chinease Journal of Metal Science and Technology, **8**: 185-191, (1992) .

[67] T. Nishizawa, and K. Ishida, *Co-Cu (Cobalt-Copper)*. In: *Binary alloy phase diagrams, Vol. 2*. 2nd ed, edited by T.B. Massalski. ASM International: Materials Park; 1990. pp. 1181-1183 .

[68] M. Palumbo, S. Curiotto, L. Battezzati. *Thermodynamic analysis of the stable and metastable Co-Cu and Co-Cu-Fe phase diagrams*. Computer Coupling of Phase Diagrams and Thermochemistry, **30**: 171-178, (2006).

[69] R.J. Smith, W. Li, J. Coulson, M. Clark, M.G. Somekh, S.D. Sharples. *Spatially resolved acoustic spectroscopy for rapid imaging of material microstructure and grain orientation*. Measurement Science and Technology, **25**(5): 055902 (11pp), (2014).

[70] W. Li, S.D. Sharples, R.J. Smith, M. Clark, M.G. Somekh. *Determination of crystallographic orientation of large grain metals with surface acoustic waves*. The Journal of the Acoustical Society of America, **132**(2): 738-745, (2012).

[71] *ASM Handbook: Vol. 6a: Welding Fundamentals and Processes*. ASM International: Materials Park; 2011 .

[72] R.W. Messler. *Principles of welding: processes, physics, chemistry and metallurgy.* John Wiley & Sons: New York; 1999

[73] D. Romans, E.N. Simons. *Welding processes and technology.* Pitman: London; 1968

[74] J.F. Lancaster. *Metallurgy of welding.* 6th Edition. Abington Publishing: Cambridge; 1999

[75] L.P. Connor, editor. *Welding Handbook. Volume 1. Welding Technology.* 8th Edition. American Welding Society: Miami; 1987

[76] R.L. O'Brian, editor. *Welding Handbook. Volume 2. Welding Processes.* 8th Edition. American Welding Society: Miami; 1987

[77] J.C. Lippold. *Welding metallurgy and weldability.* John Wiley & Sons: Hoboken; 2015

[78] W.F. Savage, E.F. Nippes, E.S. Szekeres. *A study of weld interface phenomena in a low alloy steel.* Welding Journal **55**(9): 260s-268s, (1976)

[78] J.A. Goldak, M. Akhlaghi. *Computational Welding Mechanics.* Springer US: New York; 2005

[80Clark] D.S. Clark, W.R. Varney. *Physical Metallurgy for Engineers.* Second Edition. D. Van Nostrand Company: Princeton; 1962

[81] Z.D. Jastrzebski. *Nature and Properties of Engineering Materials.* John Wiley & Sons: New York; 1962

[82] D. Rosenthal. *Mathematical theory of heat distribution during welding and cutting.* Welding Journal **20**(5): 220s-234s, (1941)

[83] C.M. Adams. *Cooling rates and peak temperatures in fusion welding.* Welding Journal (NY), **37**: 210s-215s (1958)

[84] N. Christensen, V. de L. Davies, K. Gjermundsen. *Distribution of temperatures in arc welding.* British Welding Journal **12**(2): 54-75, (1965).

[85] C.R. Heiple, J.R. Roper. *The geometry of gas tungsten arc, gas metal arc, and submerged arc weld beads.* In: *Welding: Theory and practice*, edited by D.L. Olson, R.D. Dixon, A.L. Liby. North-Holland: Amsterdam; 1990. pp. 1-34

[86] S. Kou. *Welding Metallurgy.* John Wiley & Sons: Hoboken; 2003

[87] H. Udin, E.R. Funk, J. Wulff. *Welding for engineers.* Wiley: New York; 1954

[88] T.W. Eager, N.-S. Tsai. *Temperature fields produced by traveling distributed heat sources.* Welding Journal, **62**(12): 346s-355s, (1983).

[89] A.C. Nunes. *An extended Rosenthal weld model.* Welding Journal, **62**(6): 165s-170s, (1983).

[90] N.D. Malmuth, W.F. Hall, B.I. Davis, C.D. Rosen. *Transient thermal phenomena and weld geometry in GTAW.* Welding Journal, **53**(9): 388s-400s, (1974).

[91] *Welding Simulation Suite. From Fast Distortion Engineering & Fabrication Planning to Weld Repair & Root Cause Analysis.* ESI Group; 2011. https://www.esi-group.com/sites/default/files/resource/brochure_flyer/1032/folder_welding.pdf. Accessed August, 2015.

[92] *Simufact welding. The solution to simulating welding processes.* Simufact Engineering, Gmbh. http://www.simufact.de/en/solutions/Praesentation_wel/ Simufact_BR_simufact.welding_en.pdf. Accessed August, 2015

[93] C.S. Wu, L. Dorn. *Computer simulation of fluid dynamics and heat transfer in full-penetrated TIG weld pools with surface depression.* Computational Materials Science, **2**(2): 341-349, (1994)

[94] T. Zacharia, A.H. Eraslan, D.K Aidun, S.A. David. *Three-dimensional transient model for arc welding process.* Metallurgical Transactions B, **20**(5): 645-659, (1989).

[95] G.A. Taylor, M. Hughes, N. Strusevich, K. Pericleous. *Finite volume methods applied to the computational modelling of welding phenomena.* Applied Mathematical Modelling, **26**(2): 311-322, (2002).

[96] T.U. Seidel, A.P. Reynolds. *Two-dimensional friction stir welding process model based on fluid mechanics.* Science and Technology of Welding & Joining, **8**(3): 175-183, (2003).

[97] J.T. Plewes, K.J. Bachmann. *The effect of thermomechanical pretreatment on the allotropic transformation in cobalt*. Metallurgical Transactions, **4**: 1729-1734, (1973).

[98] *Casti Metals Blue Book: Welding Filler Metals.* 4th Edition. Casti Publishing: Alberta; 2003.

[99] *Standard Test Method for Guided Bend Test for Ductility of Welds*. Designation: E190-92. ASTM International, 2008.

[100] G.F. Vander Voort. *Metallography, principles and practice*. McGraw-Hill: New York; 1984.

[101] J.T. Armstrong. *Citzaf-a package of correction programs for the quantitative electron microbeam X-ray analysis of thick polished materials, thin films, and particles*. Microbeam Analysis, **4**(3): 177-200, (1995).

[102] Y.Z. Tian, S.D. Wu, Z.F. Zhang, R.B. Figueiredo, N. Gao, T.G. Langdon. *Microstructural evolution and mechanical properties of a two-phase Cu-Ag alloy processed by high-pressure torsion to ultrahigh strains*. Acta Materiala, **59**: 2783-2796, (2011).

[103] Q. Meng, S. Guo, X. Zhao, S. Veintemillas-Verdaguer. *Bulk metastable cobalt in fcc crystal structure*. Journal of Alloys and Compounds, **580**: 187-190, (2013).

[104] M.R. Hill. *The slitting method*. In: *Practical Residual Stress Measurement Methods*, edited by G.S. Schajer. John Wiley & Sons Ltd: Chichester; 2013. pp. 89-108.

[105] M.B. Prime. *Experimental procedure for crack compliance (slitting) measurements of residual stress*. LA-UR-03-8629. Los Alamos National Laboratory; 2003.

[106] C.C. Seepersad, E. Taleff, J.R. Howell, G. Ely, S. Shah. *LANL-UCSD-UT Research on Weld Residual Stresses in Beryllium. FY09 Quarterly Report* (Third Quarter: April-June). Los Alamos Engineering Institute; July, 2009.

[107] B.M. MacPherson, W.W. Beaver. *Fusion Welding of Beryllium.* WADD Technical Report 60-917. Accession Number: AD0269349. Brush Beryllium Company, April 1961

Appendix I. Welding Parameter Studies

Table 11: Robotic MIG parameter study[1]

Set	Weld	Geometry	Pass	Power (V)	Traverse (ipm)	Filler	Result
MIG1	1	Butt, V-groove	1	23	25	AlSi	Cracking
MIG1	2	Butt, V-groove	1	22.5	25	AlSi	Cracking
MIG1	3	Butt, V-groove	1	22.5	25	AlSi	Cracking
MIG1	4	Butt, V-groove	3	22.5	75	AlSi	Cracking
MIG2	1	Butt, V-groove	1	18	15	AgMn	No Penetration
MIG2	2	Butt, V-groove	1	19	15	AgMn	No Penetration
MIG2	3	Butt, V-groove	1	19	18	AgMn	No Penetration
MIG2	4	Butt, V-groove	3	19	54	AgMn	No Penetration
MIG3	1	Plate, V-groove	1	19	12	AgMn	No Penetration
MIG3	2	Plate, V-groove	1	20	12	AgMn	No Penetration
MIG3	3	Plate, V-groove	1	20	15	AgMn	No Penetration
MIG3	4	Plate, V-groove	1	19	15	AgMn	No Penetration
MIG3	5	Plate, V-groove	1	20	15	AgMn	No Penetration
MIG3	6	Plate, V-groove	1	20	18	AgMn	No Penetration
MIG3	7	Plate, V-groove	3	20	18	AlSi	Cracking
MIG4	1	Butt, V-groove	1	20	18	AgMn	No Penetration
MIG4	2	Butt, V-groove	1	20	18	AgMn	No Penetration
MIG5	1	Bead on Plate	1	20	15	AgMn	No Penetration
MIG5	2	Bead on Plate	1	20	12	AgMn	No Penetration
MIG5	3	Bead on Plate	1	22	15	AgMn	No Penetration
MIG5	4	Bead on Plate	1	22	12	AgMn	No Penetration
MIG5	5	Bead on Plate	1	24	15	AgMn	No Penetration
MIG5	6	Bead on Plate	1	24	12	AgMn	No Penetration
MIG5	7	Bead on Plate	1	24	18	AgMn	No Penetration
MIG5	8	Bead on Plate	1	26	15	AgMn	No Penetration
MIG6	1	Butt, V-groove	1	19	8	AgMn	No Penetration
MIG6	2	Butt, V-groove	1	20	8	AgMn	No Penetration
MIG6	3	Scrap Butt	1	20	8	AgMn	No Penetration
MIG6	4	Butt, V-groove	1	19	12	AgMn	No Penetration
MIG6	5	Butt	1	20	12	AgMn	No Penetration
MIG6	6	Butt	1	20	10	AgMn	No Penetration
MIG6	7	Butt	1	20	8	AgMn	No Penetration

[1]Co-10 wt.%Mo base, Ar top gas
[2]AlSi=Al-12wt.%Si; AgMn=Ag-12wt.%Mn

Table 12: Manual MIG parameter study[1]

Set	Weld	Geometry	Passes	Power (V)	Feed (fpm)	Base[2]	Result[3]
MIG7	1	Scrap Plate	1	19.9	5.1	CoMo	<1mm
MIG7	2	Scrap Plate	1	19	5.1	CoMo	<1mm
MIG7	3	Scrap Plate	1	16	5.1	CoMo	Failure
MIG7	4	Scrap Plate	1	19.9	5.1	CoMo	<1mm
MIG7	5	Scrap Plate	1	21	5.1	CoMo	<1mm
MIG7	6	Scrap Plate	1	12.5-17	3.2	CoMo	<1mm
MIG7	7	Scrap Plate	1	21	5.5	CoMo	<1mm
MIG7	8	Scrap Plate	1	25	4,5,7	CoMo	<1mm
MIG7	9	Scrap Plate	1	17	4	CoMo	<1mm
MIG7	10	Scrap Plate	1	25[3]	4,5,7	CoMo	Failure
MIG7	11	Scrap Plate	1	19.9	4.75	CoMo	adhesion
MIG8	1	Scrap	1	21	5.5	Co	adhesion
MIG8	2	Scrap	1	24.5	5	Co	adhesion
MIG8	3	Scrap	1	23.5	5.5	Co	adhesion
MIG8	4	Scrap	1	23	5	Co	adhesion
MIG8	5	Scrap	1	21	5.5	Co	adhesion
MIG9	1	Scrap Plate	1	21	5.5	Co	<1mm
MIG9	2	Bead on Plate	1	23	3, 3.5, 4.5	Co	<1mm
MIG9	3	Bead on Plate	1	24.5	4.5	Co	<1mm
MIG9	4	Bead on Plate	3	22	5	Co	<1mm
MIG9	5	Bead on Plate	3	22.5	5	Co	Failure

[1]Ar top gas, AgMn Filler
[2]CoMo=Co-10 wt.%Mo
[3]Numerical values indicate penetration depth
[3]Spray Arc

Table 13: Manual TIG parameter study I[1]

Set	Weld	Geometry	Passes	Power (A)	Special Technique	Filler[2]	Penetration (mm)
1	1	Bead on Edge	1	119		AgMn	<<1
1	2	Bead on Plate	1	119	Base Pre-melt	AgMn	~1
1	3	Bead on Plate	1	119	Melt, Add, Stop	AgMn	~1
1	4	Bead on Plate	1	119	Slow	AgMn	<1
1	5	Bead on Plate	1	119	Oscillation	AgMn	~1
1	6	Bead on Plate	1	119	Small Bead	AgMn	<<1
1	7	Bead on Plate	3	119		AgMn	<<1
1	8	Bead on Plate	1	119	Tiny Bead	AgMn	~1
2	1	Bead on Edge	1	218	Slow	AgMn	~2
2	2	Bead on Plate	1	218	Slow	AgMn	~2
2	3	Bead on Plate	1	119	Slow	AgMn	~1
2	4	Bead on Plate	1	119	Slow	AgMn	~1
3	1	Butt, V-groove	1	218	Slow	AgMn	<1
3	2	Butt, V-groove	3	218	Tight Root	AgMn	~2

[1]CoMo base, Ag-12wt%Mn filler, Ar top gas, no back-gas
[2]AgMn=Ag-12wt%Mn

Table 14: Manual TIG parameter study II[1]

Set	Weld	Geometry	Passes	Power (A)	Special Technique	Filler	Result[3]
4	1	Butt, V-groove	3	218	Tight root	AgMn	<1 mm
5	1	Scrap Plate	1	218	Hot	AgMn	~3 mm
5	2	Scrap Plate	1	218	Pulse	AgMn	~1 mm
5	3	Scrap Plate	1	234	Pulse	AgMn	~1 mm
5	4	Scrap Plate	1	160	Slow, light foot	AgMn	~2 mm
5	5	Scrap Plate	1	200		AgMn	~2 mm
5	6	Scrap Plate	3	234	Slow, light foot	AgMn	~2 mm
6	1	Butt, V-groove	1	218		AgMn	<1 mm
6	2	Butt, V-groove	1	250		AgMn	~1 mm
6	3	Butt, V-groove	3	150		AlSi	Cracking
6	4	Butt, V-groove	1	119	Vertical	AgMn	<1 mm
6	5	Butt, V-groove	3	119	Vertical	AgMn	~2 mm
6	6	Scrap Butt	1	218	Slow, .3mm gap	AgCu	No Penetration
6	7	Butt, V-groove	3	218	Melt, Add, Stop	AgCu	<1 mm

[1]Co base, variable filler, Ar top gas, no back-gas
[2]AgMn=Ag-12wt%Mn; AgCu=Ag-28wt%Cu
[3]Numerical values indicate penetration depth

Table 15: Manual TIG parameter study III[1]

Set	Weld	Geometry	Passes	Power (A)	Back-gas	Filler[2]	Notes	Result[3]
7	1	Scrap Butt	1	218		AgCu*		Adhesion
7	2	Scrap	2	218		AgCu*		~3mm
8	1	Butt, U-groove	2†	218		AgCu		~3 mm
8	2	Butt, U-groove	1	218		AgCu	45° orientation	~3 mm
8	3	Butt, U-groove	3†	218		AgCu		~2 mm
8	4	Butt, U-groove	7	218		AgCu	Passes staggered	Complete penetration
8	5	Butt, U-groove	3†	200		AgCu		~1 mm
8	6	Butt, U-groove	1	218		AgCu	Wide U-groove	Porosity
8	7	Butt, U-groove	3	218	Ar	AgCu		Complete penetration
8	8	Butt, U-groove	4	198		AgCu	Slow	Complete penetration
9	1	Final U-groove	5†	198	Ar	AgCu		~3 mm
9	2	Final U-groove	1	210	He	AgCu		Failure
9	3	Final U-groove	2	210	Ar	AgCu	Too Hot	Failure
9	4	Final U-groove	5†	225	Ar	AgCu	Pulsed	30%
9	5	Final U-groove	5†	227	Ar	AgCu	Passes staggered	30%

[1]Co base, variable filler, He top gas, variable back-gas
[2]AgCu=Ag-28wt%Cu; AgCu*=Ag-7.5wt.%Cu;
[3]Numerical values indicate maximum penetration depth. Percentage value indicates the amount of the root with complete penetration.
†Alternating passes

Table 13: Manual TIG parameter study V[1]							
Set	**Weld**	**Geometry**	**Power (A)**	**Gap (mm)**	**Passes**	**Notes**	**Result[2]**
10	1	Scrap Butt	210	.3	5/5		80%
10	2	Scrap Butt	210	.3	5/5		40%
10	3	Scrap Butt	210	.3	5/5		10%
10	4	Butt, U-groove	225	.3	2/5		10%
10	5	Butt, U-groove	210	.3	5/5		80%
10	6	Scrap Butt	210	.3	5/5	Small part	100%
11	1	Butt, U-groove	225	.3			30%
11	2	Butt, U-groove	225	0			50%
11	3	Butt, U-groove	225	.55			40%
11	4	Butt, U-groove	225	.3	5/5	Preheat[3]	90%
9	6	Final U-groove	225	.3	5/5		20%
9	7	Final U-groove	225	.3	2/5		70%
9	8	Final U-groove	225	.4	2/5	No Ar Excess Filler	50%
9	9	Final U-groove	225	.4	2/5	Preheat[3]	70%
9	10	Final U-groove	225	.35	2/5		60%
9	11	Final U-groove	225	.5	2/5		70%
9	12	Final U-groove	225	.15	2/5		0%
9	13	Final U-groove	225	.65	2/5		100%
9	14	Final U-groove	225	.25	2/5	Wrong filler	0%
9	15	Final U-groove	225	.4	2/5	Hot clamp	10%
9	16	Final U-groove	225	.5	5/5	Pool flowed into refractory	Success
9	17	Final U-groove	225	.3	3/5		0%
9	18	Final U-groove	225	0	2/5	Inconsistent	80%
9	19	Final U-groove	225	0	2/5		Success†
9	20	Final U-groove	225	0	5/5	Excess Filler	0%
9	21	Final U-groove	225	.4	5/5	Top Gas Failure	10%
9	22	Final U-groove	225	0	5/5		Success
9	23	Final U-groove	225	0	5/5	Excess Filler	30%
9	24	Final U-groove	225	0	1/5		Success†

[1]Co base, AgCu filler, He top gas, Ar back gas, 5 pass alternating direction, clamped
[2]Percentage value indicates the amount of the root with complete penetration.
[3]Preheated with propane torch
†Used for fracture testing

Table 13: Final TIG weld fabrication[1]

Set	Weld	Geometry	Passes	Power (A)	Notes	Result[2]
12	1	Butt, U-groove	5/5	220		30%
12	2	Butt, U-groove	4/5	220		100%
12	4	Scrap U-groove	5/5	225		Success
12	5	Scrap U-groove	2/5	225		Cracking
12	6	Scrap U-groove	4/5	225		Failure
12	8	Scrap U-groove	5/5	225		Cracking
12	9	Scrap U-groove	2/5	225		80%
12	10	Scrap U-groove	4/5	225		90%
12	11	Scrap U-groove	2/5	225		90%
12	12	Scrap U-groove	4/5	225		70%
12	13	Scrap U-groove	2/5	225		90%
12	14	Scrap U-groove	2/5	225		100%
12	13	Scrap U-groove	2/5	225		80%
12	14	Scrap U-groove	2/5	225		100%
12	15	Scrap U-groove	2/5	225		80%
12	16	Scrap U-groove	2/5	225		Cracking
12	1	Final U-groove	5/5	225		Failure
12	2	Final U-groove	4/5	225		Success†
12	3	Butt, U-groove	3/5	225	Equipment Failure	Failure
12	4	Final U-groove	5/5	225		Success†
12	5	Final U-groove	6/5	225	Extra Pass	Failure
12	6	Butt, U-groove	5/5	225		Success
12	7	Final U-groove	5/5	225		Success†
12	8	Final U-groove	5/5	225		Success†
12	9	Final U-groove	2/5	225	Inconsistent	90%
12	10	Final U-groove	5/5	225		Success*
12	11	Final U-groove	4/5	225		70%
12	12	Final U-groove	5/5	225		Success†
12	13	Final U-groove	5/5	225		Success†
12	14	Final U-groove	4/5	225	Excess Helium	Failure
12	15	Final U-groove	5/5	225		Success†
12	16	Final U-groove	5/5	225		Success†
12	17	Final U-groove	5/5	225		Success†
12	18	Final U-groove	5/5	225		Success*
12	19	Final U-groove	5/5	225	Filler Contaminated	Failure
12	20	Final U-groove	5/5	225		Success†
12	21	Final U-groove	5/5	225		Success†
13	22	Final U-groove	5/5	225		Success†

[1]Co base, AgCu filler, He top gas, Ar back gas, 5 pass alternating direction, furnace preheated clamp
[2]Passes 1-2=225 A, Pass 5=150 A
[3]Numerical values indicate percent of the root penetrated
†Used for fracture testing
*Used for SRAS